

MASTER'S THESIS

Haloscope search for Axion dark matter around 4.6 GHz :
First results from a prototype equipped with a 9T, 110 mm
diameter magnet and a HEMT amplifier

4.6 GHz 近傍での、ハロースコープによる暗黒物質アクシオン探索—直径110ミ
リ9TマグネットとHEMTアンプを用いたプロトタイプ検出器による最初の結果

Marthe AZZI

Department of Physics
Graduate School of Science
Tohoku University

2024

Abstract

Axion is a hypothetical elementary particle that appears as an elegant solution not only to the unexplained conservation of charge-parity symmetry in the strong interaction but also to the dark matter mystery. The last decades have dismissed many of the dark-matter candidates leaving to the axion great motivations. However, axion search is very challenging because the theory does not provide strong constraints on its mass range and requires high sensitivity. Although many different detection methods have been employed, the unexplored region remains vast. To address this, we have initiated the search for axions at RCNS with a new resonant cavity haloscope. This method is based on the coupling of axions with two photons. The prototype consists of an electromagnetic resonant cavity placed in a relatively large magnet of diameter 110 mm, length 200 mm, and 8.76 T. The whole was cooled to 8.8 K by two GM cryocoolers and we use a conventional low-noise-HEMT amplifier.

Our results probe axion masses in the range $[1.908370397, 1.908415832] \times 10^{-5}$ eV, which corresponds to frequencies of around 4.6145 GHz. Assuming axions to be the only component of the dark matter halo embedding our galaxy ($\rho_a = 0.45$ GeV/cm³) and its velocity to follow a Maxwellian distribution, we have conducted a statistical analysis. Under 90% confidence level, no statistically significant axion signals have been found over our search range so we set a rejection line on the possible values of the coupling constant $g_{a\gamma\gamma}$. The most stringent limit on $g_{a\gamma\gamma}$ is 8×10^{-14} GeV⁻¹ at 1.908380×10^{-5} eV and the worst limit is 2.03×10^{-13} GeV⁻¹ at 1.908373×10^{-5} eV. These results are already competitive and position us at the forefront of axion searches. Future upgrades, such as a larger magnet, a low-noise superconducting amplifier, or a superfluid helium cryostat, promise to drastically enhance our sensitivity, expanding our reach into the axion parameter space.

Keywords: particle physics, strong CP-problem, dark matter, axion, axion two-photon coupling constant, haloscope, RF cavity

Acknowledgment

I am very grateful to my supervisor, Professor Yasuhiro Kishimoto, for his dedication to teaching me scientific methods, his support throughout my master's program, and his successful experiment. I also thank Atsushi Tokiyasu, Professor Izumi Ogawa, and Professor Masaki Yamashita for their advice and contribution to this work. Finally, I extend my thanks to the Research Center for Neutrino Science for their warm welcome and for allowing me to take part in the KamLAND-Zen Collaboration.

Contents

Introduction	6
1 Axion Theory	7
1.1 Strong Charge-Parity (CP) problem	7
1.1.1 The U(1) Axial problem	7
1.1.2 Chiral anomaly	8
1.1.3 Theta-vacua	9
1.1.4 Interpretation	13
1.1.5 Contribution from quarks mass matrix	14
1.1.6 The neutron electric dipole moment	15
1.2 Peccei and Quinn solution	15
1.2.1 PQ mechanism	15
1.2.2 PQWW, KSVZ and DFSZ models	16
1.3 Conclusion	17
2 Dark Matter	18
2.1 Dynamical arguments	18
2.2 Dark Matter candidates	19
2.2.1 MACHOs	19
2.2.2 Primordial Blackholes	19
2.2.3 Modified Gravity	19
2.2.4 Sterile neutrino	19
2.2.5 Superpartners	20
2.2.6 WIMPs	20
2.2.7 Axion-like-particles	20
2.3 Axion DM halo Energy density	21
2.3.1 Galactic halo models	21
2.3.2 Creation mechanism in the Early Universe	21
2.3.3 First limits on axion mass	22
2.3.4 Pre-Inflation and Post-Inflation Scenarios	23
2.3.5 Trapped misalignment mechanism	24
2.4 Conclusion	25
3 Experiment	26
3.1 Status of axion experiments	26
3.1.1 Haloscopes	26
3.1.2 Helioscopes	27
3.1.3 Light-shinning-through-the-wall	27
3.2 Our experiment	28
3.2.1 Magnet	28
3.2.2 Cavity and geometric factor	29
3.2.3 Target range	31
3.2.4 Tuning and quality factor	31
3.2.5 Cryogenic environnement	31
3.2.6 Circuit diagram	33
3.2.7 Data acquisition	34
3.2.8 Amplifier calibration	34
4 Data Analysis	36
4.1 Axion signal shape	36
4.1.1 Axion signal likelihood distribution	36
4.1.2 Axion signal power excess	37
4.1.3 Fitting function	39
4.1.4 Signal search range	39

4.2	Stability check	40
4.2.1	Temperature	40
4.2.2	Gain	42
4.2.3	Quality factor and resonance frequency	43
4.2.4	Antenna coupling	47
4.3	Digital spectrometer data treatment	48
4.3.1	Compilation	48
4.3.2	Background fitting	50
4.4	Statistical analysis	51
4.4.1	Signal and Null samples	51
4.4.2	Confidence intervals	52
4.4.3	Hypothetical test of non-zero P hypothesis	53
4.4.4	Rejection line	57
4.4.5	Systematics and final result	58
	Conclusion	60
	5 Prospects	60
	Appendix	66
	A CPT symmetries	66
	B Basic definitions in Gauge theories	67
	C Goodness of fit	67
	D Lorentz approximation	69
	E Details of lorentz fit results on VNA data	70
	F Natural units	71

Introduction

The axion draws its origins from a long-lasting mystery: why is the eta meson so heavy? The solution to this problem was brought by the Nobel Prize Gerard 't Hooft. He demonstrated that the vacuum of QCD was more complicated than we thought by relating chirality to topology. However, this revealed by the same time the so-called strong CP problem. The question then became, why is the neutron electric dipole moment so small? In 1977, Roberto Peccei and Helen Quinn proposed the existence of a new symmetry. The latter would be an exact symmetry of the classical action, have a color anomaly and be spontaneously broken. This results in a (pseudo)-Goldstone boson called the axion. Shortly after its introduction, the idea emerged that the axion could also be the solution to another, much older mystery: dark matter. Cosmologists have observed abnormal dynamics in the universe. Spiral galaxies rotate faster than the gravitational pull of visible matter would predict. Either Newton's second law is wrong, or there must be some invisible matter causing this discrepancy. Axion has the right properties to be this invisible matter. It does not interact directly with light, interacts only weakly with other forces and could be produced in the right amount to constitute all the missing matter. Thus, axion may lie at the intersection of two of the biggest mysteries in modern physics. Whether the axion is the solution or not, we need experiments. Luckily, observations suggest that Earth is surrounded by a halo of dark matter. It is therefore possible that we have many axion dark matter particles around us. However, because of its very weak interactions and low mass, the search for such a particle is a major challenge. It requires very sensitive detectors and a search in a very wide range of mass. Electromagnetic resonant cavities have proven to be efficient in reaching the parameter space of axion QCD. Axions have no electric charge and no quantum spin, but they can interact via the Strong force with the electro-magnetic field. This small interaction can give a signal that will be amplified by the resonant cavity if the latter is tuned to the right frequency or, equivalently, to the right axion mass. In this way, we can test several frequencies and exclude the mass range where we observe no signal. This is the contribution we want to make with our experiment.

This thesis is organized into five parts. Section 1 explains the emergence of the strong CP problem and the introduction of the axion as a solution. Section 2 exposes the mystery of dark matter and a cosmological discussion regarding the axion. Then, Section 3 presents the current state of axion experiments and our own experiment. Finally, the process of our data analysis is explained in Section 4. In a last but short Section 5, we will discuss our research prospects.

1 Axion Theory

This chapter is an attempt to grasp the origin and interest of axions as a solution to a long-standing problem in the Standard Model. Some basic definition and notations can be found in Appendix B. In addition, the explanations given in [1] were very useful for my understanding of the theta vacuum.

1.1 Strong Charge-Parity (CP) problem

The strong CP problem involves not only QCD as its name suggests but also the flavor physics of the weak interaction. Let's first focus on QCD, and then we will consider the contribution of the quarks mass matrix.

1.1.1 The U(1) Axial problem

Things started with the $U(1)_A$ QCD problem. Quantum chromodynamics (QCD) is the theory that describes the strong nuclear interaction. It is a gauge theory with the SU(3) symmetry group coupled to $N_f = 6$ Dirac fermions which are the quarks. In the Standard Model, the Lagrangian density that describes Quantum Chromodynamics (QCD) is

$$\begin{aligned}\mathcal{L}_{\text{QCD}} &= \mathcal{L}_{\text{gluons}} + \mathcal{L}_{\text{quarks}} \\ &= -\frac{1}{4}G\tilde{G} + \sum_f^{N_f} \bar{\psi}_f(i\gamma^\mu D_\mu - m_f)\psi_f\end{aligned}$$

with ψ the quark field, m the quark's mass, f the index for the quark's flavor (up, down, charm, strange, top, or bottom), G the gluon field strength tensor. The index f will be sometimes omitted for clarity. Now, each quark field can be decomposed into left-handed and right-handed components.

$$\psi_L = \frac{1}{2}(1 - \gamma^5)\psi \quad \psi_R = \frac{1}{2}(1 + \gamma^5)\psi \quad \psi = \psi_L + \psi_R$$

Using the properties of γ^5 , namely $(\gamma^5)^2 = 1$ and $\{\gamma^5, \gamma^\mu\} = 0$, we have,

$$\bar{\psi}_L\psi_L = 0, \quad \bar{\psi}_R\psi_R = 0, \quad \bar{\psi}_L i\gamma^\mu D_\mu \psi_R = 0, \quad \bar{\psi}_R i\gamma^\mu D_\mu \psi_L = 0$$

Thus,

$$\mathcal{L}_{\text{quarks}} = \sum_f \left[\bar{\psi}_L i\gamma^\mu D_\mu \psi_L + \bar{\psi}_R i\gamma^\mu D_\mu \psi_R - \bar{\psi}_L m_f \psi_R - \bar{\psi}_R m_f \psi_L \right] \quad (1)$$

The $U(1)_A$ transformation rotates the left- and right-handed quarks with opposite phases.

$$\psi_L \rightarrow \psi_L e^{i\frac{\phi}{2}}$$

$$\psi_R \rightarrow \psi_R e^{-i\frac{\phi}{2}}$$

The kinetic terms remain unchanged as the phase cancel each other but not the mass terms. After a $U(1)_A$ transformation, the Lagrangian density of QCD is:

$$\mathcal{L}_{\text{QCD}} = -\frac{1}{4}G\tilde{G} + \sum_f^{N_f} \left[\bar{\psi} i\gamma^\mu D_\mu \psi - m_f (\bar{\psi}_L \psi_R e^{-i\phi} + \bar{\psi}_R \psi_L e^{i\phi}) \right]$$

In the limit where quarks masses tend to zero, it seems that \mathcal{L}_{QCD} has a global $U(N_f)_V \otimes U(N_f)_A$ symmetry. In the context of the strong interaction, taking this limit is reasonable at least for the first generation, since $m_u, m_d \ll \Lambda_{\text{QCD}}$, and this is enough to highlight the problem. So let's focus on the first generation.

$$\mathcal{L}_{QCD} = -\frac{1}{4}G.\tilde{G} + \sum_{u,d} \bar{\psi}i\gamma^\mu D_\mu\psi$$

The Lagrangian density above respects $U(2)_V \otimes U(2)_A$ symmetry. Experimentally, we observe that $U(2)_V$ is indeed a good approximate symmetry through the detection of nucleons and pions: p, n, π^\pm, π^0 . However, for the axial symmetry, $U(2)_A = SU(2)_A \otimes U(1)_A$, we have $SU(2)_A$ that is spontaneously broken because of the quarks condensate. Therefore, according to the Goldstone Theorem it should exist four Nambu-Goldstone bosons (NGBs). As we are dealing with approximate symmetry ($m_u, m_d \approx 0$), the NGBs can have a small mass, so we should call them pseudo-NGBs. In the hadronic spectrum, we have three pions that are light enough for being pseudo-NGBs, but we are missing a fourth light meson of mass smaller than $\sqrt{3}m_\pi$. The demonstration can be found in [2]. Either a meson is missing, or the η meson is too heavy.

Meson	Composition	Approximate Mass (MeV)
π^+	$\bar{d}u$	139
π^0	$\frac{1}{\sqrt{2}}(\bar{u}u - \bar{d}d)$	135
π^-	$\bar{u}d$	139
η	$\frac{1}{\sqrt{6}}(\bar{u}u - \bar{d}d - 2\bar{s}s)$	548
η'	$\frac{1}{\sqrt{3}}(\bar{u}u - \bar{d}d + \bar{s}s)$	958

Table 1: Mass of mesons [3]. Kaons are ignored in the 2 flavor QCD.

1.1.2 Chiral anomaly

Perhaps we are not detecting this light meson because there is no $U(1)_A$ symmetry in the strong interactions [2]. Indeed a chiral anomaly was identified for the axial-vector current [4]. The axial-vector current is expressed as, $J_{\mu 5} = \sum_f \bar{\psi}_f \gamma_\mu \gamma_5 \psi_f$. The chiral anomaly is the unexpected $G.\tilde{G}$ term which appears in its divergence.

$$\partial^\mu J_{\mu 5} = 2i \sum_f^{N_f} m_f \bar{\psi}_f \gamma_5 \psi_f + 2N_f \frac{g^2}{32\pi^2} G.\tilde{G} \neq 0$$

with the factor 2 because of two chiralities.

This anomaly seems to prevent the conservation of the axial current even for massless quarks. With the $U(1)_A$ transformation of rotation phase ϕ section 1.1.1, the effective action is,

$$\begin{aligned} S_{eff} &= S_{QCD} + \phi \int d^4x \partial^\mu J_{\mu 5} \\ &= S_{QCD} + \phi 2N_f \frac{g^2}{32\pi^2} \int d^4x G.\tilde{G} \quad \text{for massless quarks} \end{aligned}$$

Or we can write the effective Lagrangian density for the strong interaction as,

$$\mathcal{L}_{eff} = \mathcal{L}_{QCD} + \phi 2N_f \frac{g^2}{32\pi^2} G.\tilde{G}$$

For some time, the missing meson problem was explained by the discovery of this chiral anomaly.

1.1.3 Theta-vacua

The $U(1)_A$ problem was thought to be solved by the chiral anomaly until John Bardeen [5] found that the term $G.\tilde{G}$ could be written as,

$$\frac{g^2}{32\pi^2}G.\tilde{G} = \partial_\mu K^\mu$$

$$\text{with } K^\mu = \frac{g^2}{32\pi^2}\epsilon^{\mu\alpha\beta\gamma}A_\alpha^a(G_{\beta\gamma}^a - \frac{g}{3}f^{abc}A_\beta^b A_\gamma^c)$$

According to Stokes' theorem, the volume integral of a divergence is equal to the surface integral of the vector field.

$$\int_V d^4x \partial_\mu K^\mu = \oint_{\partial V} \vec{d\sigma} \cdot \vec{K} = \oint_{\partial V} d\sigma_\mu K^\mu$$

$d\sigma = (d\sigma_0, d\sigma_1, d\sigma_2, d\sigma_3)$ is the normal vector at a point of the surface ∂V . This surface ∂V is the boundary of space-time, so we are dealing with boundary conditions. It is a 3-dimensional surface because when we go at infinity in one direction of spacetime, we loose a degree of freedom. For instance, a field A at the limit $x_1 \rightarrow +\infty$ will be expressed in terms of A_2, A_3, A_0 . As another example, at the limit $x_0 \rightarrow +\infty$ we are left with the 3-dimensional space.

Thus, we easily see that if we take $A_\mu^a = 0$ as boundary condition, the surface integral vanishes. In this case, the $G.\tilde{G}$ term would not affect the action and the $U(1)_A$ problem comes back. However, Gerard 't Hooft [6] realized that the correct boundary conditions were A_μ^a a pure gauge field at infinity. It means that A_μ^a is either equal to 0 or a gauge transformation of 0. In other words, the vacuum had more configurations than we thought. According to the gauge transformation written above, those extra configurations have the form :

$$A_\mu = 0 \rightarrow \frac{i}{g}\Omega\partial_\mu\Omega^{-1}$$

Besides, under the gauge transformation, K^μ does not remain unchanged,

$$K^\mu \rightarrow K^\mu + \frac{1}{24\pi^2}\text{Tr} \epsilon^{\mu\alpha\beta\gamma}\Omega\partial_\alpha\Omega^{-1}\Omega\partial_\beta\Omega^{-1}\Omega\partial_\gamma\Omega^{-1} + \frac{ig}{8\pi^2}\partial_\beta\text{Tr} \epsilon^{\mu\alpha\beta\gamma}\partial_\alpha\Omega^{-1}\Omega A_\alpha$$

Since we have chosen to look at the gauge transformation of $A_\mu = 0$, the expression simplifies to,

$$K^\mu \rightarrow \frac{1}{24\pi^2}\text{Tr} \epsilon^{\mu\alpha\beta\gamma}\Omega\partial_\alpha\Omega^{-1}\Omega\partial_\beta\Omega^{-1}\Omega\partial_\gamma\Omega^{-1}$$

Hence,

$$\oint_{\partial V} d\sigma_\mu K^\mu = \frac{1}{24\pi^2} \int d\sigma_\mu \text{Tr} \epsilon^{\mu\alpha\beta\gamma}\Omega\partial_\alpha\Omega^{-1}\Omega\partial_\beta\Omega^{-1}\Omega\partial_\gamma\Omega^{-1} \quad (2)$$

As we can see, the above integral no longer promises to vanish. Moreover, we can easily show that if the standard/classical Euclidean action of gluons noted $S_E^{cl}(A)$ is finite, then so is the integral (2). The subscript E recalls that we are working in Euclidean space.

$$\begin{aligned} \left| \oint_{\partial V} d\sigma_\mu K^\mu \right| &= \left| \frac{g^2}{32\pi^2} \int d^4x_E G.\tilde{G} \right| \\ &\leq \frac{g^2}{32\pi^2} \int d^4x_E |G.\tilde{G}| \\ &\leq \frac{g^2}{8\pi^2} \frac{1}{4} \int d^4x_E |G.\tilde{G}| \leq \frac{g^2}{8\pi^2} \frac{1}{4} \int d^4x_E G^2 = \frac{g^2}{8\pi^2} S_E^{cl}(A) \end{aligned}$$

We admit that $S_E^{cl}(A)$ is finite. Thus K is integrable on ∂V and we note,

$$\nu \equiv \oint_{\partial V} d\sigma_\mu K^\mu$$

By analogy, ν is called a topological charge with K the corresponding topological current. However K is not a physical current since it is not gauge invariant. It belongs to the broader category of Chern-Simons currents. To understand why topology is involved, we will show how the expression (2) can be related to the Jacobian determinant of a continuous differentiable mapping between two three-spheres. To begin with, let's see what these two three-spheres correspond to.

As explained before, the boundary conditions of spacetime could be studied in any "directions", resulting in a three dimensional spacetime. For simplicity 't Hooft decided to look at the boundary conditions in the temporal limit $t = \pm\infty$ so that we are left with only spatial field configurations. This is a gauge fixing called the Weyl gauge and, mathematically, it consists in $A_0 = 0$. With this choice, the field configurations of vacuum depend only on spatial coordinates $\vec{x} = (x_1, x_2, x_3)$. However, we still need to distinguish a few different boundary conditions for the gauge transformation of 0.

$$\begin{aligned}
A_\mu = 0 &\rightarrow \frac{i}{g}\Omega_m(\vec{x})\partial_\mu\Omega_m(\vec{x})^{-1} && \text{when } t \rightarrow -\infty \\
&\rightarrow \frac{i}{g}\Omega_n(\vec{x})\partial_\mu\Omega_n(\vec{x})^{-1} && \text{when } t \rightarrow +\infty \\
&\rightarrow \frac{i}{g}\Omega_\infty\partial_\mu\Omega_\infty^{-1} && \text{when } |\vec{x}| \rightarrow \infty \\
&\text{and } \Omega_m, \Omega_n \rightarrow \Omega_\infty && \text{when } |\vec{x}| \rightarrow \infty
\end{aligned} \tag{3}$$

Ω_m, Ω_n and Ω_∞ can be any element of the gauge group as long as $\Omega_m, \Omega_n \rightarrow \Omega_\infty$ when $|\vec{x}| \rightarrow \infty$. They are *a priori* different. The reason for the indexes m, n and ∞ will come later. Without creating artifacts, we can perform the following gauge transformation,

$$A_\mu \rightarrow \Omega_\infty^{-1}A_\mu\Omega_\infty + \frac{i}{g}\Omega_\infty^{-1}\partial_\mu\Omega_\infty \tag{4}$$

Then we can redefine $\Omega_m(\vec{x}) := \Omega_m(\vec{x})\Omega_\infty^{-1}$ and $\Omega_n(\vec{x}) := \Omega_n(\vec{x})\Omega_\infty^{-1}$ and we have now Ω_m and Ω_n that tend to 1 as $|\vec{x}| \rightarrow \infty$. With this redefinition, spatial infinity becomes topologically equivalent to a 3-sphere. It is called compactification.

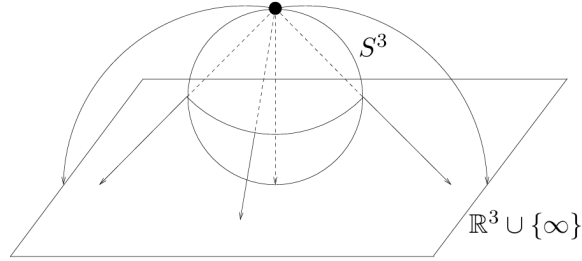


Figure 1: Stereographic projection after compactification. From [7]

Besides, since $SU(2)$ is topologically equivalent to a 3-sphere and $SU(2) \subset SU(3)$, there exists a smooth map between $SU(3)$ and a 3-sphere.

So let's note S_3 the compactified spatial infinity and S'_3 the sphere associated with the gauge group. According to eq (3) and (4),

$$\begin{aligned}
m &=: \frac{1}{24\pi^2} \int d\sigma_\mu \text{Tr } \varepsilon^{\mu\alpha\beta\gamma} \Omega_m \partial_\alpha \Omega_m^{-1} \Omega_m \partial_\beta \Omega_m^{-1} \Omega_m \partial_\gamma \Omega_m^{-1} \\
&= \frac{1}{24\pi^2} \left(\frac{g}{i}\right)^3 \int_{S_3} d^3x \text{Tr } \varepsilon^{\alpha\beta\gamma} A_\alpha A_\beta A_\gamma \Big|_{t=-\infty}
\end{aligned}$$

and the same works for n .

Hence, we can identify $\text{Tr } \varepsilon^{\alpha\beta\gamma} A_\alpha A_\beta A_\gamma$ to the Jacobian determinant of the map f between the compactified spatial infinity and the gauge group (with a different map for $t = -\infty$ or $t = +\infty$).

$$\text{Tr } \varepsilon^{\alpha\beta\gamma} A_\alpha A_\beta A_\gamma \Big|_{t=\pm\infty} = \det J(f_{\pm\infty})$$

with a map $f_{\pm\infty} : S_3 \rightarrow S'_3$

Another way to see m (or n) is as a "winding number". The Jacobian determinant represents how the volumes around each points are distorted when they are mapped from S_3 to S'_3 . Therefore, integrating the Jacobian determinant over the entire S_3 gives the total volume change. The key point is to recall that "volume" refers here to the intrinsic volume of the manifold, not the volume of a sphere. Besides, the winding number corresponds to the number of time the whole S_3 would wrap around S'_3 under the map f (with f a continuous map between two compact oriented manifolds of same dimension). Hence, it becomes clear that both the integral of the Jacobian determinant and the winding number describe the same factor m .

We have described so far the configurations at spatial infinity, so now let's try to calculate the value of the integral ν .

In the Weyl gauge $A_0 = 0$, only $K^0 \neq 0$. In this choice of gauge, it is convenient to visualize ∂V as a cylinder of radius $|\vec{x}| \rightarrow \infty$ and whose lower and upper bases correspond respectively to the time slices $t = -\infty$ and $t = +\infty$. The surface element over a time slice at t is simply the spatial volume element $d\sigma_0 = dx_1 dx_2 dx_3 = d^3x$. Thus, the expression for the topological charge simplifies to,

$$\begin{aligned} \nu &= \oint_{\partial V} d\sigma_0 K^0 \quad \text{with } \partial V = \{(\vec{x}, t) \text{ so that } |\vec{x}| = \infty, t = \pm\infty\} \\ &= \int d\sigma_0 K^0(\vec{x}, t = +\infty) - \int d\sigma_0 K^0(\vec{x}, t = -\infty) \\ &= \int d^3x \left[K^0(\vec{x}, +\infty) - K^0(\vec{x}, -\infty) \right] \end{aligned}$$

Without loss of generality, we name the integral value by the indices used previously,

$$\begin{aligned} \int d^3x K^0(\vec{x}, -\infty) &= \oint_{\partial V} d\sigma_\mu K^\mu(\vec{x}, -\infty) \\ &= \frac{1}{24\pi^2} \oint_{\partial V} d\sigma_\mu \text{Tr } \varepsilon^{\mu\alpha\beta\gamma} \Omega_m \partial_\alpha \Omega_m^{-1} \Omega_m \partial_\beta \Omega_m^{-1} \Omega_m \partial_\gamma \Omega_m^{-1} \\ &:= m \\ \int d^3x K^0(\vec{x}, +\infty) &:= n \end{aligned}$$

Hence, $\nu = n - m$.

Configurations with different winding numbers are topologically distinct, i.e. they belong to different equivalence classes. The only way to go from one configuration to another is through instanton. According to the Atiyah-Singer index theorem, the finite nature of the Euclidean action in turn implies that the topological charge is an integer.

$$\begin{aligned} |m\rangle_- &= |m\rangle_+ \text{ through perturbation theory} \\ |m\rangle_- &= |m+1\rangle_+ \text{ through instanton} \end{aligned}$$

However, those pure gauge states we have described so far are not gauge invariant whereas the physical vacuum state of QCD must respect gauge invariance. Let's visualize the transition from the abstract to the physical level.

We pick a state for each gauge-equivalence class. Those states live in a large vector space we call V . Each of the pure gauge states also belongs a gauge-equivalent class which, as we have seen, can be characterized by their winding number. Therefore, some elements of V can be expressed as a linear combination of pure gauge states. In other words, a set of pure gauge states span a subspace of V . The physical vacuum state belongs to this subspace. Let's note its coefficients c_m .

$$|\theta\rangle_{\pm} = \sum_m c_m |m\rangle_{\pm}$$

with $|m\rangle$ pure gauge states.

Now, the physical vacuum state must respect gauge invariance. What does this imply for the c_m coefficients?

The unitary operator U on V -space does,

$$U |m\rangle_{\pm} = |m+1\rangle_{\pm}$$

A state is gauge invariant, if and only if, it is an eigenstate of U . Besides, U is unitary so its eigenvalues can be written as $e^{i\theta}$ with θ a real number and we note the corresponding eigenstates $|\theta\rangle$.

$$U |\theta\rangle_{\pm} = e^{i\theta} |\theta\rangle_{\pm}$$

From now, let's ignore the subscript \pm .

$$\begin{aligned} U |\theta\rangle &= \sum_m c_m U |m\rangle = \sum_m c_m |m+1\rangle = \sum_m \frac{c_m}{c_{m+1}} c_{m+1} |m+1\rangle = \sum_m \frac{c_{m-1}}{c_m} c_m |m\rangle \\ e^{i\theta} |\theta\rangle &= \sum_m e^{i\theta} c_m |m\rangle \end{aligned}$$

The members of the family $(|m\rangle)_m$ of pure gauge states are independent because they do not belong to the same equivalence class, so we can identify,

$$\frac{c_{m-1}}{c_m} = e^{i\theta}$$

We can take $c_0 = 1$, so

$$|\theta\rangle = \sum_m e^{-im\theta} |m\rangle$$

We do not know if there is any physical principle that could determine what θ should be. Of course, θ and $\theta + 2\pi$ give the same vacuum state, but between these two values, there is an infinite number of possible vacuum states that are fundamentally different. So θ takes a value in the range $[0; 2\pi[$ but the Standard Model does not give more constraints. We can just accept that, mathematically, θ parametrises a family of vacua, each corresponding to a different theory of QCD.

However, the value of θ might make a difference in experiments. To understand its effect, let's write the vacuum to vacuum transition and use the path integral formalism.

$$\begin{aligned}
{}_+ \langle \theta | \theta \rangle_- &= \sum_{m,n} e^{in\theta} e^{-im\theta} \langle n | m \rangle_- \\
&= \sum_{\nu, m} e^{i(\nu+m)\theta} e^{-im\theta} \langle m + \nu | m \rangle_- \\
&= \sum_{\nu} e^{i\nu\theta} \sum_m \langle m + \nu | m \rangle_- \\
&= \sum_{\nu} e^{i\nu\theta} \int [dA]_{\nu} e^{iS_{QCD}[A]} \\
&= \sum_{\nu} \int [dA] e^{i(S_{QCD}[A] + \nu\theta)} \delta\left(\nu - \frac{g^2}{32\pi^2} \int d^4x_E G \cdot \tilde{G}\right) \\
&= \int [dA] e^{iS_{eff}[A]} \\
&\text{with } S_{eff} = S_{QCD} + \theta \frac{g^2}{32\pi^2} \int d^4x_E G \cdot \tilde{G}
\end{aligned}$$

With $[dA]_{\nu}$, we have integrated over all possible paths or field configurations that belong to the same topological sector (i.e. equivalence class), the latter being characterized by the topological charge ν . Hence, the complexity of the QCD vacuum effectively adds a term to the QCD Lagrangian,

$$\mathcal{L}_{eff} = \mathcal{L}_{QCD} + \theta \frac{g^2}{32\pi^2} G \cdot \tilde{G} \quad (5)$$

To conclude, we do not have the $U(1)_A$ problem because we have a more complicated vacuum. However, this vacuum has a mysterious parameter θ . The theoretical freedom of choice of θ is in fact a large freedom of choice for the coupling constant ϕ of section 1.1.2.

1.1.4 Interpretation

Recall that all these troubles came from a chiral transformation. So there must be a connection between chirality and topological charge. Let's see what is the effect of a chiral transformation on a theta-vacuum.

As we have seen section 1.1.2, the $U(1)_A$ current $J_{\mu 5}$ is not conserved for massless quarks. It is not a current in the Noether sense.

$$\partial^{\mu} J_{\mu 5} = 2N_f \frac{g^2}{32\pi^2} G \cdot \tilde{G}$$

We want to construct a Noether current $J_{\mu 5}^{\text{sym}}$ so we require,

$$\partial^{\mu} J_{\mu 5}^{\text{sym}} = 0$$

$$Q_5 = \int d^3x J_{05}^{\text{sym}}$$

with Q_5 the associated conserved charge

However, in contrast to $J_{\mu 5}$, the current $J_{\mu 5}^{\text{sym}}$ is not gauge-invariant. Nevertheless, we can relate the two current by,

$$\begin{aligned}
\partial^{\mu} J_{\mu 5} &= \partial^{\mu} J_{\mu 5}^{\text{sym}} + 2N_f \partial^{\mu} K_{\mu} \\
J_{\mu 5} &= J_{\mu 5}^{\text{sym}} + 2N_f K_{\mu}
\end{aligned}$$

Firstly, the conserved charge transforms as follow,

$$\begin{aligned}
UQ_5U^{-1} &= U \int d^3x J_{05}^{\text{sym}} U^{-1} \\
&= U \int d^3x J_{05} U^{-1} - 2N_f U \int d^3x K_0 U^{-1} \\
&= \int d^3x J_{05} - 2N_f \left(\int d^3x K_0 - 1 \right) \\
&= Q_5 + 2N_f \\
\text{Using : } U \int d^3x K_0 U^{-1} &= \int d^3x K_0 - 1
\end{aligned}$$

So a chiral transformation on a theta-vacuum gives,

$$\begin{aligned}
U \exp\left\{i \frac{\phi}{2N_f} Q_5\right\} |\theta\rangle &= U \exp\left\{i \frac{\phi}{2N_f} Q_5\right\} U^{-1} U |\theta\rangle \\
&= \exp\left\{i \frac{\phi}{2N_f} (Q_5 + 2N_f)\right\} e^{i\theta} |\theta\rangle \\
&= e^{i(\theta+\phi)} \exp\left\{i \frac{\phi}{2N_f} Q_5\right\} |\theta\rangle
\end{aligned}$$

Besides, we know that,

$$U |\theta + \phi\rangle = e^{i(\theta+\phi)} |\theta + \phi\rangle$$

So $\exp\{i \frac{\phi}{2N_f} Q_5\} |\theta\rangle$ and $|\theta + \phi\rangle$ belong to the same equivalence class, all θ -vacua are degenerate and describe the same theory [8].

$$\exp\{i \frac{\phi}{2N_f} Q_5\} |\theta\rangle \sim |\theta + \phi\rangle$$

However, this is only true in the massless case. If one considers the mass of quarks, Q_5 is no longer conserved and θ -vacua are no longer equivalent.

1.1.5 Contribution from quarks mass matrix

Now we consider equation (5) with the mass term from quarks,

$$\mathcal{L}_{eff} = -\frac{1}{4} G_{\mu\nu}^a G^{\mu\nu a} + \theta \frac{g^2}{32\pi^2} G \cdot \tilde{G} + \sum_f \left[\bar{\psi}_f i \gamma^\mu D_\mu \psi_f - \psi_{f,L}^- m_f \psi_{f,R} - \psi_{f,R}^- m_f \psi_{f,L} \right]$$

This expression suggests that the mass matrix of quarks has been already diagonalized and m_f are its diagonal coefficients. The latter are not necessarily real. Let's note,

$$m_f = |m_f| e^{i\phi_f}$$

As shown in Section 1.1.1, we can rotate these angle away with a $U(1)_A$ transformation,

$$\begin{aligned}
\psi_{f,L} &\rightarrow \psi_{f,L} e^{i\frac{\phi_f}{2}} \\
\psi_{f,R} &\rightarrow \psi_{f,R} e^{-i\frac{\phi_f}{2}}
\end{aligned}$$

and this results in the additional term,

$$\sum_f \phi_f 2 \frac{g^2}{32\pi^2} G \cdot \tilde{G}$$

Besides,

$$\sum_f \phi_f = \arg\left(\prod_f |m_f| e^{i\phi_f}\right) = \arg(\det(M_{diag})) = \arg(\det(M))$$

So the quarks mass matrix contributes to the theta-angle, and we note the total angle $\bar{\theta}$.

$$\begin{aligned} \theta &\rightarrow \bar{\theta} \equiv \theta + \arg(\det(M)) \\ \mathcal{L}_{eff} &= \mathcal{L}_{QCD} + \bar{\theta} \frac{g^2}{32\pi^2} G \tilde{G} \end{aligned} \quad (6)$$

With this contribution, the problem gets even more mysterious. What is this parameter $\bar{\theta}$?

1.1.6 The neutron electric dipole moment

The CP violating term equation (6) implies a non-zero neutron electric dipole moment. In other words, we would expect an asymmetric distribution of quarks in the neutron. By measuring a Larmor frequency difference, one can estimate the neutron electric dipole moment, itself proportional to $\bar{\theta}$. However, experiments like CASPER 3.1.1 do not observe such effect. Up to now, experiments have proven $\bar{\theta}$ to be very close to zero.

$$|\bar{\theta}| \lesssim 10^{-10}$$

Some could argue, it is just as Nature is done, but others remain unsatisfied. Indeed it is hard to accept that by pure chance two unrelated violating angles perfectly cancel each other until the order of 10^{-10} whereas in theory, $\bar{\theta}$ could be in the order of 1. The Standard Model aims at explaining everything without assumptions. It is built in order to minimize the number of input parameters sometimes called ‘‘constants of Nature’’ (coupling constants, mixing angles, ...). Some of those parameters have a well-understood value whereas others, like the theta angle, remain mysterious. The theta angle is the only constant of Nature that appears experimentally to be very small if not 0. However, the Standard Model, although it is a very constrained framework, struggles to explain why it takes this value.

1.2 Peccei and Quinn solution

1.2.1 PQ mechanism

To solve this problem, Peccei and Quinn introduced a new global symmetry $U_{PQ}(1)$ [9] that has a chiral anomaly. This symmetry is an exact symmetry for the classical action density, but it is spontaneously broken at the f_a scale. From this broken symmetry results a scalar (pseudo) dynamical field $a(x)$ associated with a Nambu-Goldstone boson called axion [10]. This new particle is coupled to the gluons by the following term :

$$\mathcal{L}_A = (...) + \frac{a}{f_a} \xi \frac{g^2}{32\pi^2} G \tilde{G}$$

The spontaneous symmetry breaking of $U_{PQ}(1)$ allows the vacuum expectation value $\langle a \rangle$ of the axion field to be non-zero. In principle, $\langle a \rangle$ can take any value. However, once we consider QCD anomaly, the effective potential felt by the axion is changed and the vacuum expectation value of the axion becomes,

$$\langle a \rangle = -\frac{f_a \bar{\theta}}{\xi}$$

Thus, if we include axion to the Standard Model Lagrangian density, the theta term disappears when the axion field relaxes.

$$\mathcal{L}_{SM+A} = (...) + (\bar{\theta} + \frac{a}{f_a} \xi) \frac{g^2}{32\pi^2} G \tilde{G}$$

The strong CP symmetry is preserved when the axion field is at its minimum potential and CP violation arises from the small oscillations around this minimum.

1.2.2 PQWW, KSVZ and DFSZ models

We usually define a "standard" axion mass for convenience [11],

$$m_a^{st} = \frac{m_\pi f_\pi}{v_F} \sqrt{\frac{m_u m_d}{m_u + m_d}} \approx 25 \text{keV}$$

with $v_F \approx 250 \text{GeV}$ the Fermi scale

Then, any axion model can be characterized by 4 parameters : $\lambda_m, \lambda_3, \lambda_0$, and $K_{a\gamma\gamma}$, with,

$$\begin{aligned} \text{axion mass} \quad m_a &= \lambda_m m_a^{st} \frac{v_F}{f_a} \\ \text{coupling to pion} \quad \xi_{a\pi} &= \lambda_3 \frac{f_\pi}{f_a} \\ \text{coupling to eta} \quad \xi_{a\eta} &= \lambda_0 \frac{f_\pi}{f_a} \end{aligned}$$

And the interaction we are interested in,

$$\text{coupling to two-photon} \quad \mathcal{L}_{a\gamma\gamma} = -g_\gamma \frac{\alpha}{\pi} \frac{1}{f_a} a(x) \vec{E}(x) \cdot \vec{B}(x)$$

with α the fine structure constant

$$g_\gamma = \frac{1}{2} \left(\frac{N_e}{N} - \frac{5}{3} - \frac{m_d - m_u}{m_d + m_u} \right)$$

N_e the electro magnetic anomaly

N the color anomaly

according to [12].

In the original axion model called the PQWW (Peccei-Quinn-Weinberg-Wilczek), f_a was thought to be of the order of the electroweak scale or Fermi scale v_F , which would correspond to an axion mass around 25 keV when $\lambda_m = 1$. This model has been quickly ruled out by accelerator search and stellar evolution (section 2.3.3). However, an arbitrarily high f_a such as the grand unification scale (10^{15}GeV) remain a viable solution. Indeed, with an extremely weakly coupled axion, the evolution of stars is no longer a source of discrepancy. Moreover, high f_a implies an axion mass low enough to make it impossible to detect by accelerators. The missing energy they would induce by escaping the LHC after a collision is too small compared to the sensitivity of the LHC. It is the so-called "invisible" axion. Two famous "invisible" axion models are the KSVZ (Kim [13] Shifman Vainshtein Zakharov [14]) and the DFSV (Dine Fischler Srednicki [15] Zhitnisky) models.

Model	N_e	N	g_γ
KSVZ	0	1	$\simeq 0.97$
DFSZ	16	6	$\simeq 0.36$

Table 2: KSVZ and DFSZ model result

Note that in our analysis we will use the axion coupling to two photons defined as,

$$g_{a\gamma\gamma} \equiv g_\gamma \frac{\alpha}{\pi} \frac{1}{f_a} \tag{7}$$

1.3 Conclusion

Solving the $U(1)_A$ problem taught us that the QCD vacuum was more complicated than we thought and that justified the presence of a CP-violating term believed to be negligible until then. However, this solution gave birth to the strong CP problem. Indeed, we have a CP-violating term that does not vanish, whereas in the experiment, the CP symmetry seems to be conserved. But the problem got even worse when considering quarks masses. The theta parameter receives an $O(1)$ contribution from the electroweak sector, making the strong CP problem a fine-tuning problem in which one could hope for a happy cancellation between apparently unrelated terms. Peccei and Quinn did not believe this to be the result of chance but a strong call for a new theory. They have introduced a new global symmetry that has a chiral anomaly. This symmetry breaks spontaneously and introduces a new Nambu-Goldstone boson called the axion. Since the axion undergoes the QCD potential, it rotates the CP violating term away when relaxing. This mechanism would explain why we do not observe CP violation in the strong interaction.

2 Dark Matter

If the axion was initially introduced as a solution to the strong CP problem, it is also an appealing candidate for dark matter, if not the best motivated to date. The review [16] was a great help in structuring the first two sections of this chapter.

2.1 Dynamical arguments

The concept of dark matter takes its origin from dynamical arguments. Ever since Newton's laws of motion and universal gravitation, the mass of celestial bodies has been tied to their dynamic behaviors. In the 19th century, several scientists found discrepancies between the apparent mass distribution and the observed dynamics and suggested the existence of invisible stars, planets, clouds or black holes, referred to as 'dark masses'. In 1904, Lord Kelvin tried to estimate the amount of dark matter in the Milky Way by using the analogy of a gas subject to gravity. He related the system's size to the stars' velocity dispersion. Based on this idea, Jacobus Kapteyn and Oort developed a quantitative model for obtaining local densities of dark matter.

In 1933, Fritz Zwicky studied the redshifts of galaxy clusters [17]. He applied the virial theorem to the Coma cluster and concluded that it should contain much more dark matter than luminous matter. Besides, Sinclair Smith also made an estimate for the Virgo cluster. The scientific community remained skeptical of these results, arguing that the assumption that these clusters were in equilibrium was wrong [18],[19]. Nevertheless, in parallel, astronomers began to dream about what this dark matter might be.

Later, another set of arguments came from the study of the rotation curves of spiral galaxies, which are the rotational speed of matter as we look away from the galaxy center. At first, some argued that the rotation curves could not lead to any conclusion as one must consider an internal "viscosity" due to stellar interactions, but this argument was quickly dismissed by Chandrasekhar [20]. In the 1970s, Morton Roberts and his collaborators observed that rotation curves are anomalously flat at long distances, whereas the visible mass distribution is exponentially decreasing [21].

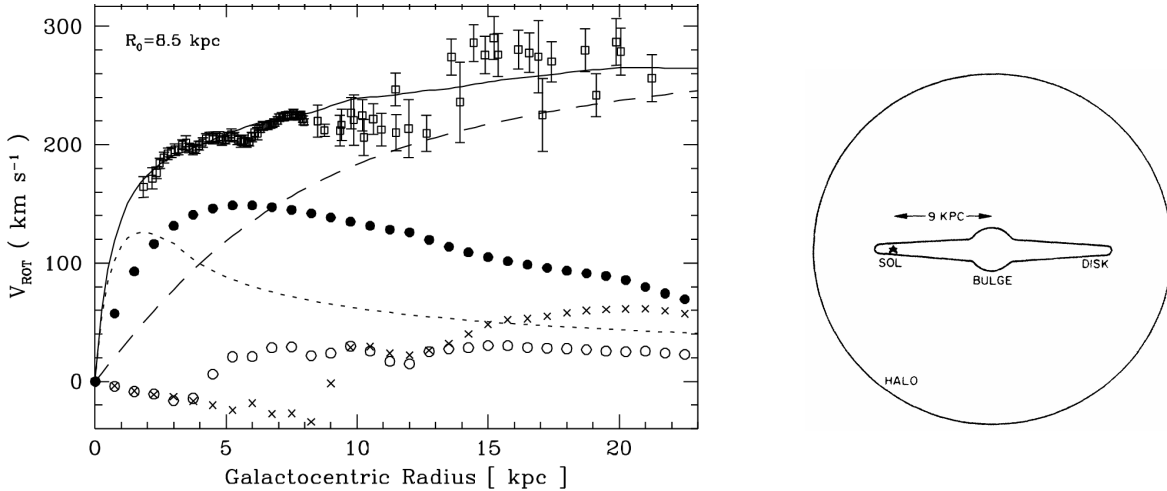


Figure 2: Rotational speed of matter as we look away from the galaxy center [22]. The contribution from the bulge (dotted line), stellar disk (filled circles), and gaseous disk made of H_1 layer (crosses), and H_2 layer (circles) cannot explain the data (squares). We need an additional curve (dashed line) which could be due to a halo of invisible matter embedding our galaxy. Right Figure from [23].

Modeling works along with improvements in radio observation technology enabled Kent Ford and Vera Rubin to obtain much more precise measurements [24]. They have concluded that these galaxies are all embedded in a dark matter halo whose size exceeds the visible size of the galaxy.

2.2 Dark Matter candidates

Although dark matter is an undeniable mystery, its nature remains unknown. Many solutions have been proposed. For example, some argue that the theory of gravity should be modified, while others propose the existence of new elementary particles. We will briefly describe the arguments against each of these solutions and why we think the axion is the best candidate.

2.2.1 MACHOs

As history shows, the first straightforward candidates for dark matter were objects such as planets, dwarfs, neutron stars, or black holes. These candidates are known as MACHOs (massive astrophysical compact halo objects). The exclusion of MACHOs as the main component of dark matter is the result of two different approaches.

One uses the phenomenon of gravitational lensing, i.e. the deflection of light by a mass. Considering a large number of stars in a nearby galaxy, and assuming the dark matter halo to be composed solely of MACHOs, the light coming from 1 out of 2×10^6 stars should undergo the phenomenon of gravitational lensing. Using this idea and 6.7 years of survey, the EROS collaboration [25] has set an upper limit according to which MACHO cannot explain more than 8 % of the mass of the Milky Way halo.

The other approach is based on the cosmological density of baryons. To explain the variety of nuclear elements in our universe, we first believed in stellar nucleosynthesis. Although heavy elements are indeed produced in the stellar core or supernovae, this process could not explain the observed abundance of light elements such as Helium or Deuterium. In 1946, Gamow [26] proposed the process of neutron capture for a nucleosynthesis in the Early Universe. Along with the discovery of the cosmic microwave background (CMB) in 1965 [27], one could predict the primordial light element abundances and thus set an upper limit on the cosmological baryon density. Finally, the most precise measurement of the ratio of the heights of the odd and even peaks in the CMB power spectrum was done by the Planck Collaboration [28] and has constrained baryonic matter to comprise less than 20% of the matter in the Universe. This excludes the possibility for MACHOs to be the main component of dark matter.

2.2.2 Primordial Blackholes

The failure of the baryonic matter candidates suggested the existence of new particles. But before reaching this conclusion, one dark matter candidate had survived: the primordial black hole (PHB). These black holes would have formed before the big bang nucleosynthesis and could have masses small enough (less than 10^{23} kg) not to be detected by microlensing. However, their lack of Hawking-radiation of gamma rays also constrains their mass to be at least equal to 10^{14} kg. Considering this mass range and the spectrum of density fluctuations to be scale invariant, the abundance of dark-matter PBH is too small to explain today's dark matter [29] [30].

2.2.3 Modified Gravity

Nevertheless, the idea of dark matter as “matter” has not yet won over everyone. Some physicists believe that the dynamical anomalies that led to the concept of dark matter are a clue to a new framework. In 1982, Mordehai Milgrom proposed the Modified Newtonian Dynamics theory (MOND) [31] as a weak-field limit, but no realistic framework could be established with this theory. In particular, because of incompatibility with the conservation of momentum, angular momentum and energy, as well as with general relativity. However, this suggestion has given rise to a series of efforts to develop a realistic MOND-type theory. One promising solution is Bekenstein's 2004 TeVeS theory [32]. The TeVeS theory respects observed dynamics, conservation laws, and relativistic phenomena, but has too many degrees of freedom to predict the ratio of cosmic microwave background peaks.

2.2.4 Sterile neutrino

In the 1980s, numerical simulations greatly accelerated the investigation of possible dark matter particles. A key distinction between candidates was whether they were relativistic or non-relativistic during the epoch of structure formation. These two categories, respectively called “hot” and “cold” dark matter, result in different large-scale structure patterns. Although Standard Model neutrinos

were excluded [33], so-called “sterile” neutrinos have been envisioned. Unlike standard neutrinos, sterile neutrinos do not interact via the electroweak force [34]. They could have been produced through neutrino oscillations, according to models like the Dodelson-Widrow mechanism. Research into this idea is still ongoing.

2.2.5 Superpartners

Supersymmetry is a class of quantum field theories that postulates a partner particle, called a superpartner, for every particle in the Standard Model. These superpartners are bosons for Standard Model fermions and fermions for Standard Model bosons, with the same quantum numbers except for spin. Although supersymmetry was not originally introduced to address the mystery of dark matter, some superpartners have a property that makes them compelling dark matter candidates, that is, to being weakly interacting. The first superpartner considered as a dark matter candidate was the gravitino. Later, in the context of the Minimal Supersymmetric Standard Model (MSSM) [35], neutralinos (particles arising from the mixing of the superpartners of neutral gauge bosons and the Higgs bosons) became the most studied candidates. Another key property of a viable dark matter candidate is stability and the lightest neutralino would be stable if R-parity is included in the model [36].

2.2.6 WIMPs

One of the most famous candidates is the WIMP (weakly interacting massive particles). WIMPs are stable, massive particles that interact weakly with themselves and with the Standard Model. This interaction, even if very “weak”, would have enabled dark matter to reach equilibrium with the thermal bath. At that time, dark matter would have been in constant abundance. However, as the Universe expanded and cooled, the rate of interaction with dark matter became weaker than the rate of expansion. Thermal equilibrium could no longer be, and the number of dark matter particles froze. This is the “freeze-out”. The resulting dark matter particles are known as “cold relics”. The interaction rate is smaller for heavier particles, therefore, they freeze out earlier. This scenario gives us a relationship between the current abundance of dark matter and the mass and cross-section of WIMPs [37]. The remaining degree of freedom makes WIMPs a large group of dark matter particles. Many theories beyond the Standard Model (SUSY, Extra-dimension, Effective Field theory, ...) give some dark matter candidates that belong to the broad category of WIMPs. For instance, the neutralino of supersymmetry is a WIMP. This gave the search for WIMPs additional motivation, such as the unification of forces. In addition, it turns out that with the observed abundance of dark matter and an effective cross section close to the scale of the weak interaction, we match the energy range of the LHC. This coincidence, called the WIMP miracle, raised hopes of dark matter creation in the LHC, but unfortunately nothing has yet been observed.

2.2.7 Axion-like-particles

Since the WIMP miracle is in decline, hopes have turned to another type of dark matter: non-thermally produced bosonic dark matter. These candidates are not constrained by the Pauli principle or structure formation. They can have much lower masses. For these light bosonic dark matter candidates, there are few production processes that will be exposed in the section 2.3.2. The QCD axion, belongs to this category. However, in general, Axion-Like-Particles do not require any relation between the coupling constant and the mass. Some of them are predicted by theories that solve the strong CP problem but some do not, or respond to other theoretical motivations. The variety of theories results in a very wide parameter space to probe.

2.3 Axion DM halo Energy density

A first step in reducing the parameter space is to discuss the energy density of the DM axion on Earth. Its value depends on the combination of particle physicists’ models with cosmology as shows Figure 3.

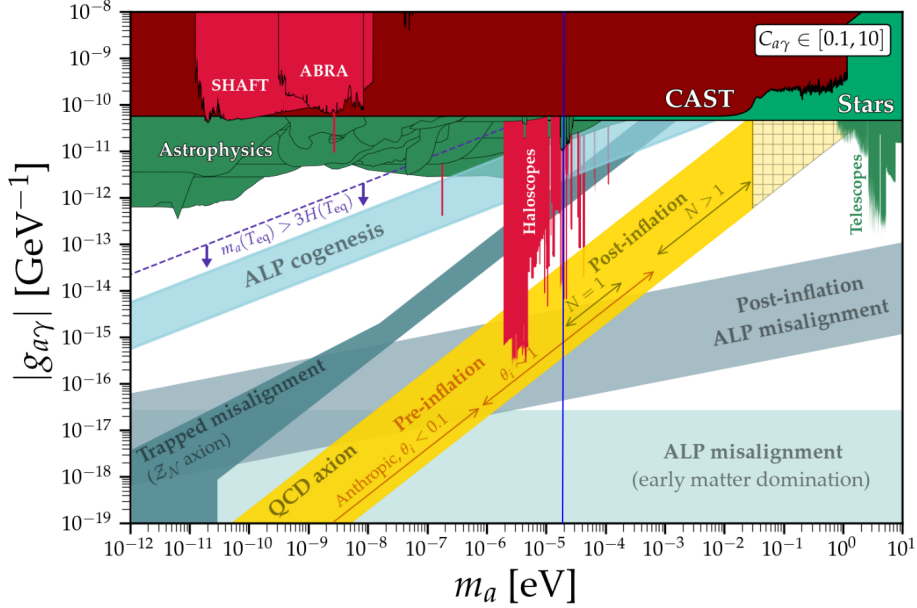


Figure 3: Our search position at the blue marker, among the current limits and predictions of theoretical models. Adapted from [38].

2.3.1 Galactic halo models

The energy density and velocity distribution depend on the dark matter halo model considered. In our data analysis, we assume the simpler model in which dark matter has reached thermal equilibrium in the halo. Therefore, the axion signal’s velocity is expected to follow a Maxwell-Boltzmann distribution (section 4.1.1) like a thermalized gas. With this model, the local dark matter density on Earth is,

$$\rho_a = 0.45 \text{ GeV/cm}^3 \quad [39], [40]. \quad (8)$$

A second model [41] argues that gravitational interactions of dark matter have postponed the reach of equilibrium. This implies the presence of “caustics”, very high density regions, which produce dominating flows in the velocity distribution. However, this model suffers from uncertainties due to the galaxy rotational speed and is therefore difficult to test.

2.3.2 Creation mechanism in the Early Universe

To estimate the energy density of axions and their impact on the evolution of the Universe, it is essential to consider how the axion would have been produced. We distinguish the “hot axion” produced thermally in the primordial plasma and the “cold axion” resulting from the axion field’s relaxation.

Hot axions are produced in the primordial plasma. Today, they would have a temperature of a few kelvins and would be moving too fast to make up the dark matter of galactic halos. Moreover, we have no technique for detecting them.

The cold dark matter axion is produced by the axion’s field relaxation process, known as “vacuum realignment”. Since symmetry breaking, the weakly interacting bosonic field has begun to oscillate, releasing energy. The observation of dark matter today would correspond to the axion field’s remaining small oscillations around its minimum potential. The axion particle we aim to detect follows this creation mechanism, so from now on we will focus on the case of the “cold axion”.

The effective potential for the axion field induced by the QCD anomaly is,

$$V_{QCD}(a) = \chi(T) \left[1 - \cos\left(\frac{\xi a}{f_a} + \bar{\theta}\right) \right] \quad (9)$$

and $\chi(T) = \begin{cases} \chi_0 & \text{if } T < T_{QCD} \\ \chi_0 \left(\frac{T}{T_{QCD}}\right)^{-8.16} & \text{if } T \geq T_{QCD} \end{cases}$

with $\chi_0 \equiv m_a^2 f_a^2 = (75.6 \text{ MeV})^4$ and $T_{QCD} = 153 \text{ MeV}$. The topological susceptibility χ gives the magnitude of the potential as a function of temperature. It increases as the universe cools.

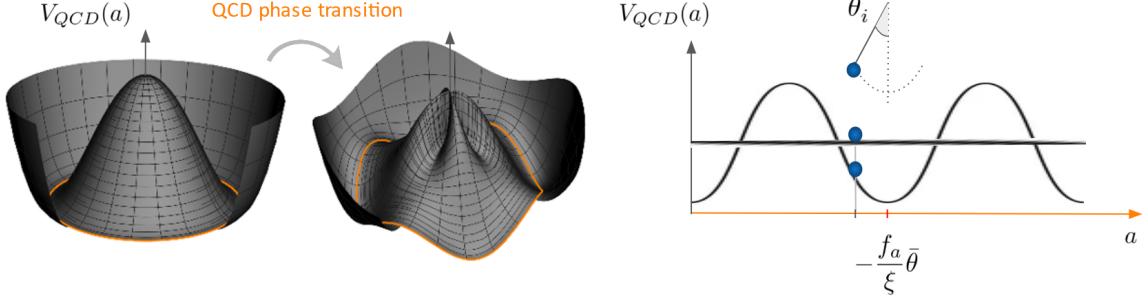


Figure 4: The very first potential on the left illustrates the spontaneous symmetry breaking of the Peccei-Quinn (PQ) symmetry. In this situation the strong CP problem is not solved yet. It is when the QCD phase transition happens that the potential felt by the axion is distorted. The axion field "rolls" into one of the new minima and cancel the theta angle. Adapted from [42].

2.3.3 First limits on axion mass

Axions cannot be too heavy. As axions are an additional loss mechanism for stars, observation of the evolution of neutron stars has led to an upper limit being set on the mass of axions. This reasoning rules out the PQWW model. At first, this was thought to rule out the axion, but soon after, the existence of an "invisible" axion was suggested.

$$10^9 \text{ GeV} < f_a$$

$$m_a < 10^{-2} \text{ eV}$$

On the other hand, one can set a lower limit on m_a with a simple idea. The strong CP problem seems to be solved when the axion field is close to its minimum potential. For this to happen, axion field oscillations must have begun sufficiently early in the history of the Universe. Since the period of oscillation is related to the mass of the particle, the finite age of the universe implies a minimum mass for the axion (or, equivalently, an upper limit for f_a).

$$\frac{2\pi}{m_a} < \text{Age Universe} \approx 4.35 \times 10^{17} \text{ s}$$

$$\Rightarrow 10^{-33} \text{ eV} < m_a$$

This lower limit can be strengthened if one considers the observed cold dark matter relative energy density Ω_{CDM} ,

$$\Omega_a h^2 < \Omega_{CDM} h^2 \approx 0.12 \quad [43]$$

The relic relative energy density of axions, noted Ω_a , is related to the initial misalignment angle θ_i as illustrated Figure 4.

$$\Omega_a h^2 \simeq 0.12 \theta_i^2 F(\theta_i) \left(\frac{f_a}{10^{12} \text{ GeV}} \right)^{1.17} \quad [44]$$

$$\text{with } \theta_i \equiv \frac{a_i \xi}{f_a} \quad (10)$$

$$F(\theta_i) = \left[\log \left(\frac{e}{1 - \theta_i^2 / \pi^2} \right) \right]^{1.17} \quad [45]$$

$F(\theta_i)$ is a correction factor for large initial misalignment angles. For small angles $F(\theta_i) \approx 1$. Thus given $\theta_i = \mathcal{O}(1)$,

$$\begin{aligned} f_a &< 10^{12} \text{ GeV} \\ 10^{-6} \text{ eV} &< m_a \end{aligned}$$

Note, that the bound on $\Omega_a h^2$ is for the whole universe and cannot be directly related to the local value ρ_a equation (8). A dark matter halo is a gravitational cluster so the density is much higher than the average $\langle \rho_a \rangle$.

$$\begin{aligned} \Omega_a &\equiv \frac{\langle \rho_a \rangle}{\rho_c} \\ \text{gives } \langle \rho_a \rangle &\lesssim 0.126 \times 10^{-5} \text{ GeV.cm}^{-3} \end{aligned}$$

with $\rho_c = 1.05 \times 10^{-5} h^2 \text{ GeV.cm}^{-3}$ the critical density from Friedmann equation for a spatially flat universe [3].

2.3.4 Pre-Inflation and Post-Inflation Scenarios

The timing of the Peccei-Quinn (PQ) symmetry breaking relative to cosmic inflation affects the initial conditions of the axion field and, consequently, the energy density of axions in the Universe.

In the ‘‘pre-inflation scenario’’ [46], the symmetry breaks when the observable universe is causally connected, so the initial misalignment angle is uniform. If the angle is small, the energy density is proportional to its square. Now if we suppose that the symmetry breaks after the inflation (‘‘post-inflation scenario’’), then the misalignment angle varies between regions that are not causally connected. So the axion’s initial energy density is no longer homogeneous. Some regions will have higher axion energy density than others, creating local overdensities of dark matter and thus more complicated dynamics. The breaking of the $U_{PQ}(1)$ during inflation can generate topological defects (axion strings and domain walls) whose decay produces axion and thus adds further contribution and uncertainty to the axion energy density. However, if the symmetry is broken early enough, the topological defects are faded away by inflation. If we go into more detail, we also have to take into account the fluctuation of the isocurvature, as well as uncertainties concerning the amount of entropy created during the QCD phase transition, and so on [47]. All these considerations result in a very wide mass range for dark matter axions, even when assuming that axion is the only component of dark matter.

In our search range, both pre- and post-inflation scenarios are possible. For post-inflation models, Figure 5 shows that we are concerned by at least three QCD axion models [48], [49], [50].

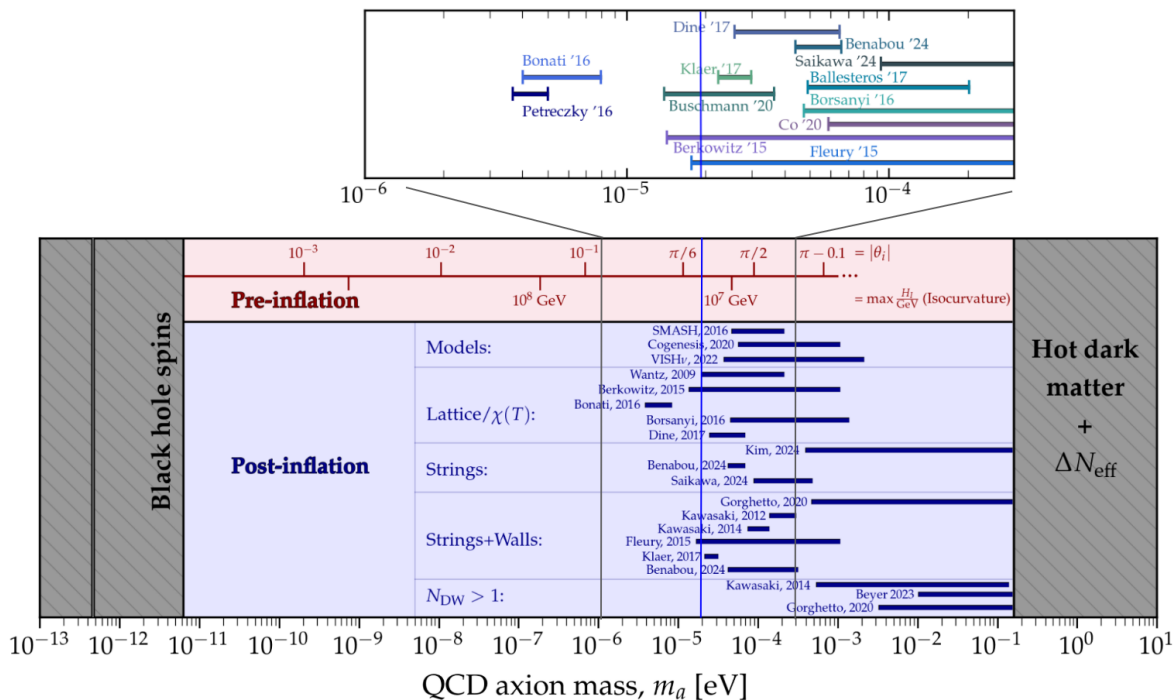


Figure 5: Our current search position in blue marker among theoretical predictions for QCD axion masses. Adapted from [38].

2.3.5 Trapped misalignment mechanism

This possibility was proposed by [51]. If the PQ symmetry is not exact but slightly broken by an extra term, this would change the resulting axion abundance. The PQ breaking term creates a potential that appears earlier than the QCD potential and that has several minima. The axion falls into one of those minima. As the universe cools, the QCD potential increases.

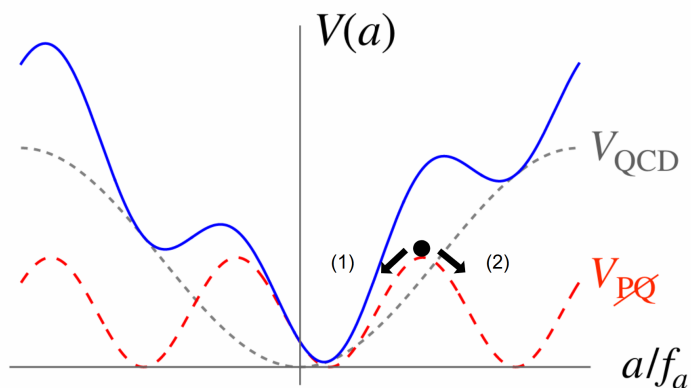


Figure 6: Effective potential of the axion. Contribution from QCD (gray dotted line), from PQ breaking term (red dotted line) and total effective potential (blue line). Adapted from [52].

In the case (2) illustrated in Figure 6, the axion will be trapped in a local minimum for some time. The axion oscillations in the true vacuum will be delayed and the initial amplitude will be larger. This leads to a higher abundance of axions. However, in the case (1), axion abundance will be lower. More details can be found in [53].

Although the effect of the PQ breaking term must disappear as the universe cools for the CP symmetry to be conserved, the axion abundance changes. This trapped misalignment mechanism is particularly impacting for the pre-inflation scenario because it removes the dependency between f_a or θ_i and the axion's abundance. Therefore, the PQ symmetry must be of high quality to maintain its predictive power.

2.4 Conclusion

In our experiment, the axions we want to detect are categorized as cold dark matter. They are produced through vacuum realignment mechanism. Moreover, they belong to the dark matter halo in which the earth is embedded. We admit the isothermal halo model which makes the axion's velocity distribution Maxwellian and its energy density to be $\rho_a = 0.45 \text{ GeV/cm}^3$. Under these assumptions, the sensitivity of our experiment will cover the trapped misalignment mechanism over our frequency search range.

3 Experiment

3.1 Status of axion experiments

Experiments for direct detection of axion can be divided into three categories, depending on the hypothetical axion source used. Haloscopes aim to detect axion relics, helioscopes investigate axion emission from the sun, and others produce their own axion, such as the Light-Shining-Through-Wall experiments.

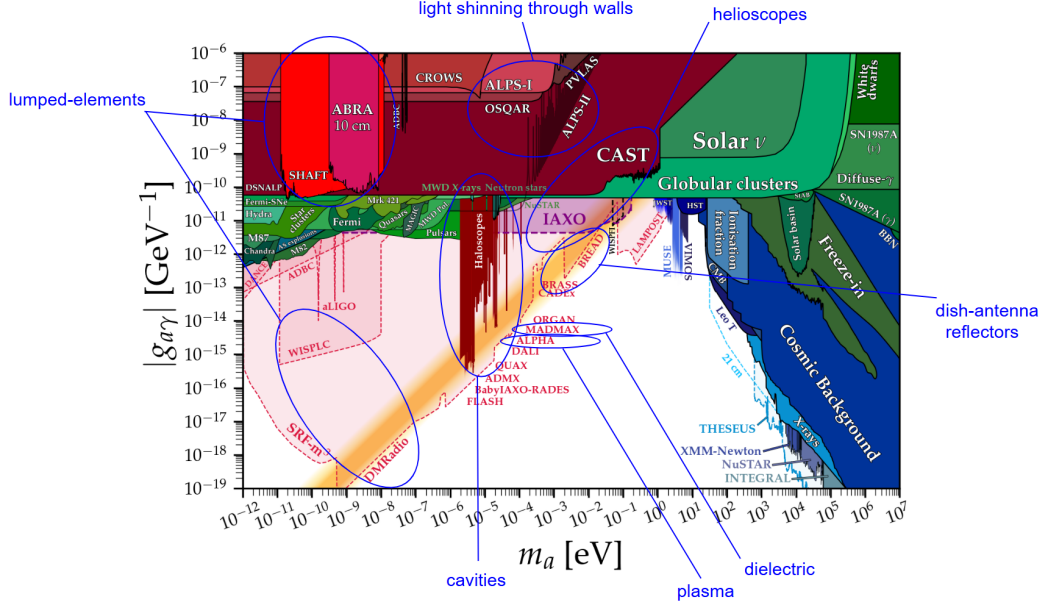


Figure 7: Status of axion search range with axion-photon coupling [38]

3.1.1 Haloscopes

ABRACADABRA [54], ADMX SLIC [55], SHAFT [56], and the upcoming DMRadio [57] experiments look for particularly low-mass axions in the GUT-scale. They use tunable "lumped-element" resonator in strong magnetic field. Axions would generate an oscillating current in a pick-up loop parallel to the static magnetic field of a toroidal or solenoidal magnet. Although cavities follow a similar idea their search range is different for two reasons. From one side, lumped elements technics are limited to low frequencies by the inductance and capacitance of their circuit. On the other hand, low frequencies require a large cavity for which high-quality factor is harder to obtain.

In cavity experiments, various strategies are employed. For instance, ORGAN (Oscillating Resonant Group AxioN) uses multi-mode cavities to scan several frequency ranges at the same time. On the contrary, HAYSTAC [58] (Haloscope At Yale Sensitive To axion Cold dark matter) focuses in enhancing their sensitivity. They have achieved a quantum-limited amplification, i.e. an amplifier noise reduced to the Heisenberg uncertainty principle, thanks to Josephson junctions. The latter consists of two superconductors separated by a thin insulator through which quantum tunneling of Cooper pairs can happen. The phase difference between the superconductors currents allows a high non-linearity that amplifies weak signals. From a mathematical point of view, it is a squeezing of the vacuum state. Finally, the most famous cavity experiment is probably ADMX [59] (Axion Dark Matter eXperiment) closely followed by CAPP as it has reached the QCD axion sensitivity. Our experimental set-up (section 3.2) is similar to these experiments.

For post-inflation axion-range we prefer: plasma, dish antenna/reflectors or dielectric technics. With a wire metamaterial, ALPHA [60] experiment creates a plasma sensitive to DM axion oscillations. BREAD and BRASS [61] experiments use bended structures, which are respectively a dish

antenna and a superconductive reflector, which gives the advantage of searching on a broader frequency band compared to cavities. MADMAX [62] (Magnetized Disk and Mirror Axion Experiment) make a series of parallel dielectric disks in a strong magnetic field. At each disk, axions can be converted into photons and the constructive interference would produce a significant signal. The tuning is done by adjusting the spacing between disks. Those three technics have not yet given results but promise a sensitivity up to QCD axion.

Finally, among haloscopes, CASPER (Cosmic Axion Spin Precession Experiment) has a quite unique approach. It does not use the axion to photon coupling. In CASPER-electric [63], the polarized samples are solid and axions can be detected through their coupling of to gluons that creates the nucleon EDM (electric dipole moment). In CASPER-wind [64], the samples are made of liquid of high nuclear spin (such as Xenon) and they use the interaction to nucleons due to the relative motion between the Earth and the axion halo. This mechanism is sometimes referred to as a CASPER-gradient because it is the gradient of the axion field that appears in the interaction term. In both experiments the axion field gives rise to an effective oscillating magnetic field perpendicular to nuclear spins and we would detect the precessive movement of spin relaxation with a SQUID magnetometer placed next to the sample. Their strategy investigates the Planck and GUT scales with a particularly broad band of frequency.

3.1.2 Helioscopes

Axion helioscope was originally proposed in [65]. A famous experiment using this idea is CAST(CERN Axion Solar Telescope). CAST experiment uses an old magnet coil of CERN to convert the solar axion flux into X-rays. The photons are then efficiently collected via optical focalisation technics. Their axion search range already very wide is expanded toward heavier masses by using gas. Up to now they achieved to set an upper limit of $5.7 \times 10^{-11} \text{GeV}^{-1}$ on the axion-photon coupling constant [66]. For higher sensitivity, the current 9m magnet will be replaced by a 25 meters coil for the upcoming IAXO experiment.

3.1.3 Light-shinning-through-the-wall

ALP, OSQUAR, and ALPS-II are experiments based on the Light-shinning-through-the-wall concept [67]. A laser source crosses a first magnetic field and produces hypothetical axions which pursue their path through a wall, and are back converted into photons in a second magnetic cavity. Those experiments have the advantage of not depending on dark matter hypothesis or halo models and look for general Axion-like-Particles (ALPs).

3.2 Our experiment

Our experiment belongs to the category of cavity haloscopes. It is designed to detect axions of the dark matter halo that embeds our Earth. We generate a strong magnetic field that will convert axions into photons. This signal is then amplified using an electromagnetic resonant cavity. The power of the axion's induced signal will depend on the properties of the axion itself, such as its coupling constant $g_{a\gamma\gamma}$, its energy density ρ_a , and its mass m_a , as well as on parameters specific to our detector : antenna coupling κ , gain G , magnetic field B_z , cavity volume V , geometric factor C , de-tuning correction α , and quality factor Q_L .

$$P = \frac{\kappa G}{(\kappa + 1)} g_{a\gamma\gamma}^2 \rho_a B_z^2 V C \frac{\alpha}{m_a} Q_L \quad (\text{section 4.1.2})$$

In this section, we describe the general structure of our experiment and determine the values of the geometric factor C and the magnetic field B_z . The other detector parameters will be estimated in the next chapter.

3.2.1 Magnet

Our project is based on the coupling of axions to photons. Under a strong static magnetic field, such as 8.76 Tesla, an axion can be converted into two photons. The axion field energy is locally transferred to the electromagnetic field. This electromagnetic field excitation is too small to be directly detected, so we amplify this perturbation using a resonant cavity. Another way to see it is with axion electrodynamics described in [12].

$$\mathcal{L}_{a\gamma\gamma} = -g a(x) \vec{E}(x) \cdot \vec{B}(x)$$

with $g \equiv g_{a\gamma\gamma}$ defined in 7

The magnetic field and the relative position of the cavity is illustrated Figure 8 and 9. In our set-up, there is an offset of 5mm horizontally and 15mm vertically between the center of the magnet and the center of the cavity.

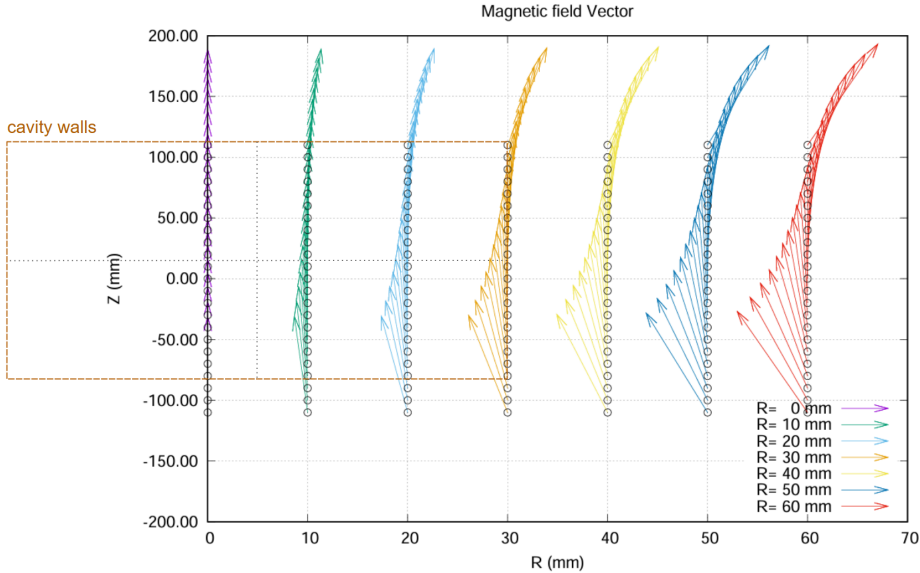


Figure 8: Magnetic field. The inner walls of the cavity are represented by a dotted brown line. The centre of the cavity is slightly offset horizontally (5mm) and vertically (15mm) from the centre of the magnet.

At a given radius, the norm of the vectors Figure 8 is slightly greater at the edges of the magnet but the change in direction dominates the effect on the B_z component. Thus, B_z is smaller on the top and bottom sides of the cavity. On the other hand, at a given position z , the norm increases as we

move away from the center, and this dominates the bending of the magnetic field. These two effects are best seen in Figure 9.

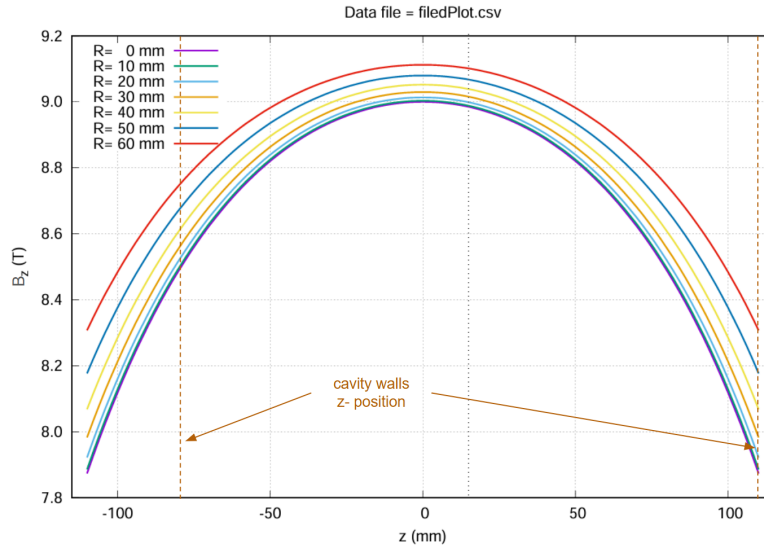


Figure 9: Isolines of radial distance from the center of the magnet in function of the z-component of the magnetic field and the z-position in the cryostat. The position of the top and bottom inner walls of the cavity corresponds to the dotted brown line.

3.2.2 Cavity and geometric factor

An electromagnetic resonant cavity consists of a conductive cylinder. Some electrons of the constitutive metal will move by inductive effect in response of the axion signal. If the dimensions of the cavity are well chosen, electrons will oscillate from one extremity of the cavity to the other and drag other electrons with them. As the number of moving charges increases, the signal induced on the antenna gets amplified. We use the transverse magnetic (TM) mode TM₀₁₀ to couple to the axion field.

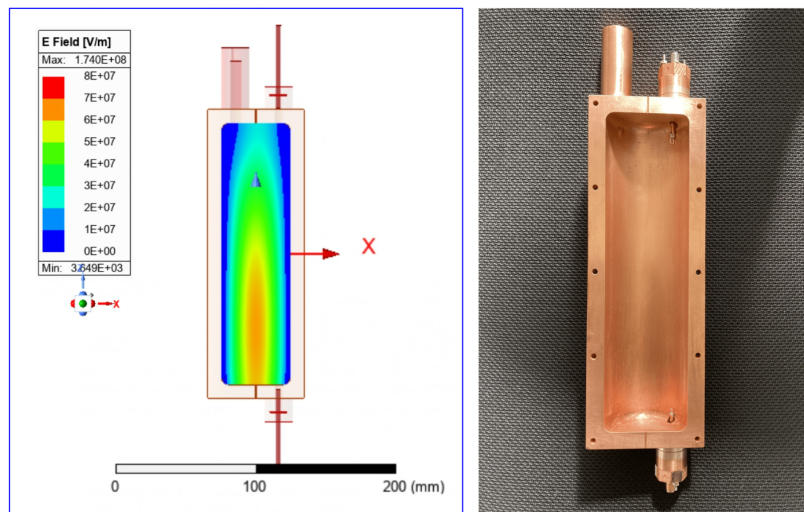


Figure 10: HFSS simulation of the TM₀₁₀ mode in a 4.5 GHz cavity model with no tuning bar (left panel) and real cavity opened (right panel).

The HFSS simulation Figure 10 along with the magnetic field Figure 8 allow us to calculate the geometric factor C .

The geometric factor or form factor is the coupling strength of a given mode n of the cavity to the axion field. According to [12] it is defined as,

$$C_n \equiv \frac{1}{B_0^2 V} \left(\int_V d^3x \vec{B}_0(\vec{x}) \cdot \vec{e}_n(\vec{x}) \right)^2 = \frac{(\int_V d^3x \vec{B}_0(\vec{x}) \cdot \vec{E}_n(\vec{x}))^2}{B_0^2 V \int_V d^3x |\vec{E}_n(\vec{x})|^2}$$

We can recognize the overlap of the static magnetic field created by the magnet and the electric field of the cavity's mode. This is why, axion search in the high frequency (or high mass) regime requires complex cavity design to keep a non-zero geometric factor. To simplify the notations, we define,

$$\begin{aligned} B_z &\equiv B_{0z} \\ E_z &\equiv E_{010z} \end{aligned}$$

B_z (or B_{0z}) is the z-component of the static magnetic field created by the magnet while E_z (or E_{010z}) is created by the resonance of the cavity in TM010 mode. They are aligned.

In addition, we slightly change the definition of the geometric factor to the following but we use B_z instead of the B_0 is the signal power excess equation (16).

$$C \equiv \frac{(\int_V d^3x \vec{B}_0(\vec{x}) \cdot \vec{E}_n(\vec{x}))^2}{B_z^2 V \int_V d^3x |\vec{E}_n(\vec{x})|^2}$$

Since we are interested in the TM010 mode of the cavity, $\vec{E}_n(\vec{x}) = E_z(\vec{x})\vec{e}_z$ so,

$$C = \frac{(\int_V d^3x B_z(\vec{x}) E_z(\vec{x}))^2}{B_z^2 V \int_V d^3x E_z(\vec{x})^2} \quad (11)$$

with B_z Figure 9 and E_z Figure 10

The volume is not the exact volume of the cavity (373.06cm^3) but an effective volume calculated by HFSS simulation,

$$V = 370.87 \pm 0.8\% \text{ cm}^3 \quad (12)$$

As shown section 3.2.1, the magnetic field slightly changes with position and the cavity is not exactly at the center of the magnet. This induces a systematic error on the average B_z and on the geometric factor.

5 mm offset gives,

$$\Delta x = \Delta y = 5/\sqrt{2} = 3.5 \pm 2 \text{ mm}$$

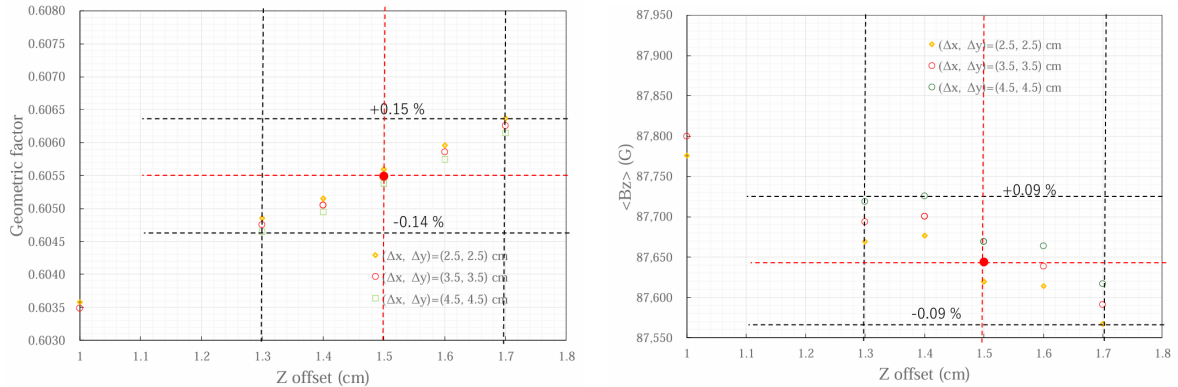


Figure 11: Deviation on the estimate of the geometric factor (left graph) and deviation on the average z component of the magnetic field in Gauss unit (right graph) due to cavity position.

To conclude,

$$C = 0.605^{+0.15\%}_{-0.14\%} \quad (13)$$

$$B_z = 8.76 \text{ T} \pm 0.9\% \quad (14)$$

3.2.3 Target range

The measurement range is set to [4.614104, 4.615104] GHz so a span of 1MHz. However, not the full range gives a sufficient sensitivity, so the final result will concern a smaller range,

$$[4.614494625, 4.614604488] \text{ GHz}$$

In terms of axion mass with natural unit, it corresponds to

$$[1.908370397, 1.908415832] \times 10^{-5} \text{ eV}$$

This range was not yet explored at the time of our experimental run. However, recently HAYSTAC phase II c/d [58] has declared some results in this range.

3.2.4 Tuning and quality factor

The use of a resonant cavity raises two main challenges: the tuning and the quality factor.

Our cavity does not have a tuning system. We cannot shift the resonance frequency. In future experiments, we will use a tuning rod to shift the resonance frequency and extend our search range while using a single cavity (section 5).

As for the quality factor Q, it characterizes the current losses in a conductive element such as cavity walls or antenna. Having a high Q factor allows to keep the signal a longer time and therefore increases the signal-to-noise ratio. For the antenna, the limit on its maximal conductivity is very high so the temperature has no effect on it, but for cavity wall, we can increase its quality factor with a cryogenic environment.

3.2.5 Cryogenic environment

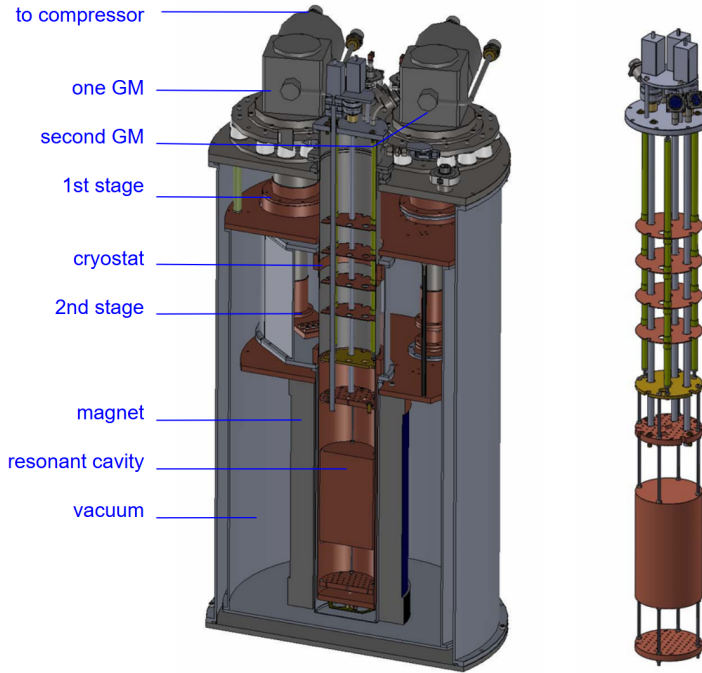


Figure 12: Two GM cryocoolers connected to the cryostat. The cryostat contains the cavity and the electronics which are held in a column as shows the right figure.

Our cryogenic system is based on a Gifford-McMahon (GM) cryocooler with helium-4. The helium gas is first compressed at room temperature by a mechanical compressor. The heat produced by this process is removed by a heat exchanger. The gas cools the first conductive plate (1st stage). Then the pressurized cooled gas undergoes expansion to reach cryogenic temperatures. It cools the second conductive plate (2nd stage). These three steps follow each other in a closed cycle. The cooling process relies only on this Joule–Thomson effect. In contrast to traditional cryogenic systems, helium is always in the gaseous state.

The cryostat itself is a cylinder in contact with the cooling plates of the GM cryocoolers and contains another helium gas. This helium gas is cooled by the walls of the cryostat and surrounds the cavity, amplifier, switches, etc. The magnet, however, is outside the cryostat, in the vacuum chamber.

Helium has the lowest boiling point of all the elements, and the gaseous state allows to quickly transfer heat away from surfaces through convection. In addition to its cryogenic cooling properties, helium is a noble gas and therefore does not react with the cavity walls. Moreover, it has a low density and a low dielectric constant (close to 1). This means that it scatters or absorbs very few microwaves, thus avoiding some signal degradation.

The background noise depends on an effective temperature,

$$T_{eff} = T_{amp} + T_{cavity} + \dots$$

with T_{amp} and T_{cavity} respectively the temperature of the amplifier and the cavity walls. The statistical fluctuations of our data follow a Gaussian distribution of standard deviation σ which is related to the effective temperature by this formula,

$$\sigma = G \frac{P}{\sqrt{N}} = G \frac{kT_{eff}\Delta\nu}{\sqrt{\tau\Delta\nu}}$$

with

$$P = kT_{eff}\Delta\nu$$

$$N = \sqrt{\tau\Delta\nu}$$

Therefore, lowering the temperature T_{eff} reduces noise.

Another way to reduce noise is to increase the measurement time. As mentioned in the previous section, longer measurement times allow to accumulate more data, which can help average out random noise. For this to be, the quality factor must be sufficiently high and stable. The quality factor is the number of oscillations a resonator can make before its energy is significantly dissipated. So, for a given conducting element, the lower its resistive losses, the higher its quality factor. In a conductive material, resistive losses are due to atomic vibrations, so to improve the electrical conductivity of the cavity walls, the system temperature must be lowered as much as possible.

3.2.6 Circuit diagram

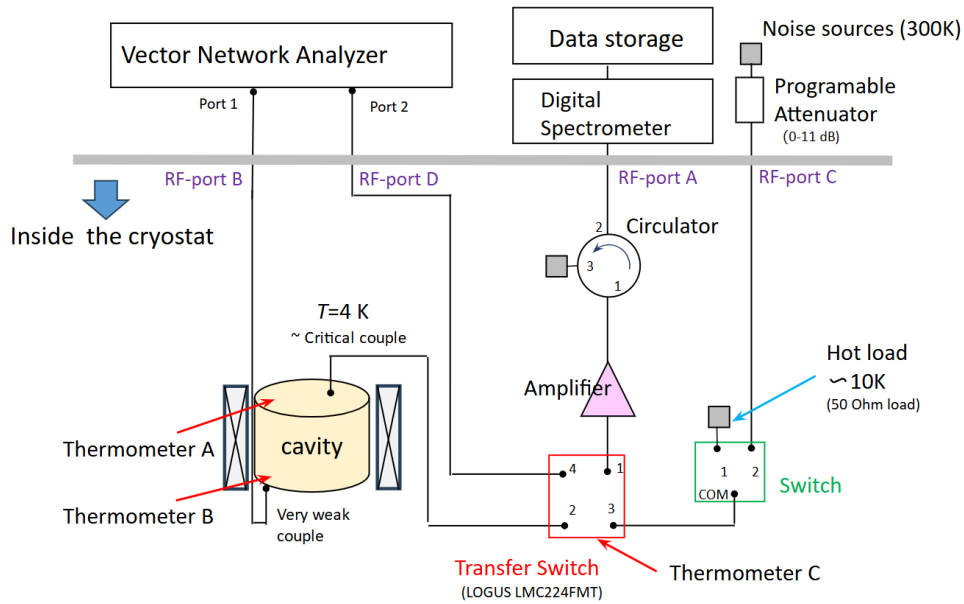


Figure 13: Circuit diagram

There are two port on the top of the cavity. One is of variable coupling and is connected via 50-ohm transmission line to a digital spectrometer. The other is weakly coupled and is used to characterize the cavity response through the transmission and reflection measurements of the VNA.

Apparatus	Reference
Digital spectrometer	Signal analyzer Anritsu MS2840A
VNA	KEYSIGHT ENA Network Analyzer E5063A (100 kHz–18 GHz)
Amplifier	LNF-LNC4-8F
Noise source 1	NC46A
Noise source 2	PE85N1007

Table 3: Details of the apparatus and their references.

Note that in this thesis, we will often use the acronym SA (signal analyzer) to refer to the digital spectrometer.

3.2.7 Data acquisition

To compile data consistently, we need to ensure that the detector response is stable. Therefore, we alternate between the acquisition of physics data and calibration measurements.

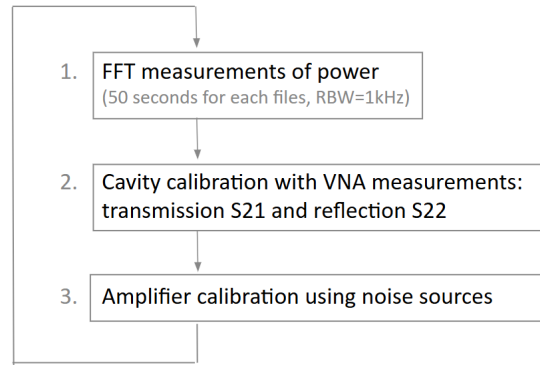


Figure 14: Data acquisition cycle

A Vector Network Analyzer (VNA) is used to check the cavity's properties. The quality factor is obtained by fitting the transmission measurement $|S_{21}|^2$ with a Lorentzian function (section 4.2.3), and the antenna coupling is estimated by fitting the Smith chart of reflection measurement S_{22} (section 4.2.4). Regarding the amplifier response, we use the digital spectrometer and a calibration noise source along with an attenuator.

3.2.8 Amplifier calibration

The amplifier's response is characterized by its gain and its noise.

$$\text{Noise}_{\text{Amp}} + P_{\text{input}}G = P_{\text{output}}$$

with G the gain of the amplifier

To obtain the amplifier's response, we use a Noisecom (NC) noise source with an attenuator. The noise source generates a known power through the amplifier and we measure the output power. The attenuator allows to get several input powers with the same noise source and so more points for gain calibration. The gain is then obtained by a linear fit.

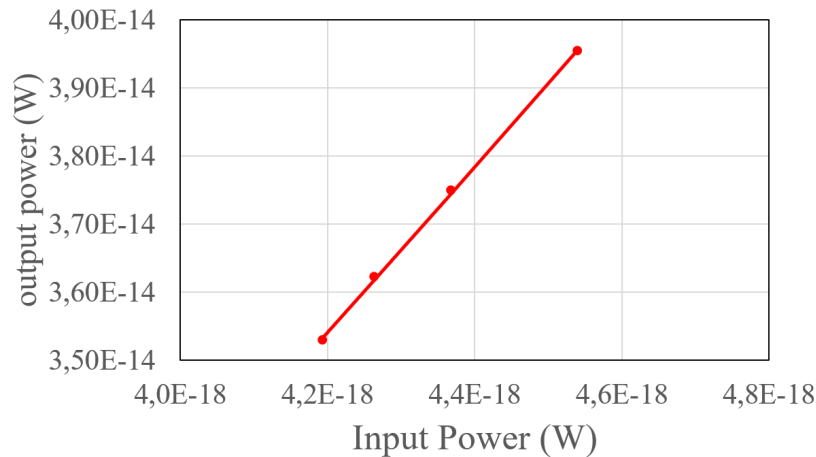


Figure 15: Example of gain estimation by a linear fit of the amplifier response to the noise source with attenuator.

Since the noise source comes with an attenuator, we can express their input power as,

$$P_{\text{input}} = \alpha k T_{NS} \Delta\nu + (1 - \alpha) k T_{\text{env}} \Delta\nu$$

with,

T_{NS} the temperature of the noise source

T_{env} the temperature of the attenuator/environment (15)

α the attenuation factor

$\Delta\nu$ the RBW of the VNA

k the Boltzmann constant

In formula (15), two temperatures enter into account: the temperature of the environment, which is about 300 K and the temperature of the noise source, which depends on the frequency and is given by the noise source company.

Noise Source	Frequency (GHz)	T_{NS} (K)
NC46A	5	1345

Table 4: Noise source temperature and reference.

Then, we have the attenuation factor α that is a parameter set on the attenuator. However, its true value is always slightly different than the set value so it must be estimated by a VNA calibration. For this, the transfer switch Figure 13 rotates into the position 4-3. Finally, $\Delta\nu$ is the RBW of the VNA and is set to the same value as the RBW of the digital spectrometer, which is 1kHz.

The input powers Figure 15 are higher than the relevant power range for axion searches. Therefore, we wanted to use also a 50-ohm noise source. The 50-ohm noise source gives a single point but its power can be lower since we can put it inside the cryostat. By combining the data from the NC configuration and the 50-ohm noise source, we could better extrapolate the amplifier’s response to the zero-power regime. However, the use of several calibration methods requires a purely mechanical switch, as it must operate in a magnetic field. In our experiment, once the magnet is turned on, the 50 Ohm cryogenic resistance cannot be used because one of the switch (green one Figure 13) does not work under magnetic field. This issue is fixed in the next experiment but for current data, the response of the amplifier must be measured using only noise sources located outside the cryostat.

4 Data Analysis

4.1 Axion signal shape

4.1.1 Axion signal likelihood distribution

Halo axion's velocity follows a Maxwell distribution f .

$$\begin{aligned} f(\mathbf{v}) &= \left(\frac{1}{2\pi}\right)^{3/2} \frac{1}{\sigma_{vx}\sigma_{vy}\sigma_{vz}} \exp\left\{-\frac{v_x^2}{2\sigma_{vx}^2} - \frac{v_y^2}{2\sigma_{vy}^2} - \frac{v_z^2}{2\sigma_{vz}^2}\right\} \\ &= \left(\frac{1}{2\pi}\right)^{3/2} \frac{1}{\sigma^3} \exp\left\{-\frac{|\mathbf{v}|^2}{2\sigma^2}\right\} \quad \text{with } \sigma_{vx} = \sigma_{vy} = \sigma_{vz} \equiv \sigma \end{aligned}$$

Integrating this distribution gives,

$$\begin{aligned} 1 &= \int \int \int_{-\infty}^{+\infty} f(v_x, v_y, v_z) dv_x dv_y dv_z = \int_0^{+\infty} \int_0^{+\pi} \int_0^{2\pi} f(|\mathbf{v}|) |\mathbf{v}|^2 \sin(\theta) d|\mathbf{v}| d\theta d\phi \\ &= \int_0^{+\infty} f(|\mathbf{v}|) \left(\int_0^{+\pi} \int_0^{2\pi} \sin(\theta) d\theta d\phi \right) |\mathbf{v}|^2 d|\mathbf{v}| \\ &= \int_0^{+\infty} f(|\mathbf{v}|) 4\pi |\mathbf{v}|^2 d|\mathbf{v}| \end{aligned}$$

We make a change of variable,

$$\begin{aligned} E &= mc^2 + \frac{1}{2}m|\mathbf{v}|^2 \\ \Rightarrow |\mathbf{v}|^2 &= \frac{2}{m}K \quad \text{with } K = E - mc^2 \\ \Rightarrow 2|\mathbf{v}|d|\mathbf{v}| &= \frac{2}{m}dK \\ \Rightarrow d|\mathbf{v}| &= \frac{dK}{m\sqrt{\frac{2}{m}K}} = \frac{dK}{\sqrt{2mK}} \end{aligned}$$

Thus,

$$\begin{aligned} f(|\mathbf{v}|)4\pi|\mathbf{v}|^2d|\mathbf{v}| &= \left(\frac{1}{2\pi}\right)^{3/2} \frac{1}{\sigma^3} \exp\left\{\frac{-2K}{2m\sigma^2}\right\} 4\pi \frac{2K}{m} \frac{dK}{\sqrt{2mK}} \\ &= \frac{1}{2\pi} \left(\frac{1}{2\pi}\right)^{1/2} \frac{1}{\sigma^3} \exp\left\{\frac{-K}{m\sigma^2}\right\} 4\pi \frac{\sqrt{2K}}{m^{3/2}} dK \\ &= \frac{2}{\sqrt{\pi}} m^{-3/2} \sqrt{K} \frac{1}{\sigma^3} \exp\left\{\frac{-K}{m\sigma^2}\right\} dK \end{aligned}$$

$$\begin{cases} E = mc^2 + K \\ K = \frac{1}{2}m|\mathbf{v}|^2 \end{cases}$$

$$\begin{cases} mc^2 =: h\nu_0 \\ K =: h\nu_k \\ K = \frac{1}{2}mc^2\left(\frac{|\mathbf{v}|^2}{c^2}\right) \end{cases}$$

So, the dispersion in velocity is equivalent to the following dispersion in frequency:

$$\begin{aligned}
f(|\mathbf{v}|)4\pi|\mathbf{v}|^2d|\mathbf{v}| &= \frac{2}{\sqrt{\pi}} \left(\frac{h\nu_0}{c^2} \right)^{-3/2} \sqrt{h\nu_k} \frac{1}{\sigma^3} \exp\left\{ \frac{-h\nu_k}{m\sigma^2} \right\} h d\nu_k \\
&= \frac{2}{\sqrt{\pi}} \left(\frac{c^2}{h\nu_0} \right)^{3/2} h^{3/2} \sqrt{\nu_k} \frac{1}{\sigma^3} \exp\left\{ \frac{-h\nu_k}{mc^2 \frac{\sigma^2}{c^2}} \right\} d\nu_k \\
&= \frac{2}{\sqrt{\pi}} \left(\frac{c^2}{\nu_0} \right)^{3/2} \sqrt{\nu_k} \frac{1}{\sigma^3} \exp\left\{ \frac{-h\nu_k}{h\nu_0} \left(\frac{c}{\sigma} \right)^2 \right\} d\nu_k \\
&= \frac{2}{\sqrt{\pi}} \frac{1}{\nu_0 \sqrt{\nu_0}} \left(\frac{c}{\sigma} \right)^3 \sqrt{\nu_k} \exp\left\{ -\frac{\nu_k}{\nu_0} \left(\frac{c}{\sigma} \right)^2 \right\} d\nu_k
\end{aligned}$$

Let's define:

$$f_{\nu_0}(\nu_k) \equiv \frac{2}{\sqrt{\pi}} \frac{1}{\nu_0 \sqrt{\nu_0}} \left(\frac{c}{\sigma} \right)^3 \sqrt{\nu_k} \exp\left\{ -\frac{\nu_k}{\nu_0} \left(\frac{c}{\sigma} \right)^2 \right\}$$

We have:

$$1 = \int_0^{+\infty} f_{\nu_0}(\nu_k) d\nu_k$$

We can see that the frequency dispersion depends on the rest axion mass $h\nu_0$. Besides, note that the index k here does not indicate discretization, but is used to remind us that ν_k corresponds to a small correction due to the Maxwellian velocity distribution.

We call ν the frequency measured by our detector. If we have a signal at ν , this frequency contains both ν_0 and ν_k . With just a shift in frequency, we can express our dispersion in function of ν .

$$\begin{aligned}
E &= h\nu \\
&= h\nu_0 + h\nu_k \\
\nu_k &= \nu - \nu_0 \quad \text{with } \nu > \nu_0
\end{aligned}$$

The change of variable from ν_k to ν gives,

$$\begin{aligned}
f_{\nu_0}(\nu - \nu_0) &\equiv \frac{2}{\sqrt{\pi}} \frac{1}{\nu_0 \sqrt{\nu_0}} \left(\frac{c}{\sigma} \right)^3 \sqrt{\nu - \nu_0} \exp\left\{ -\frac{\nu - \nu_0}{\nu_0} \left(\frac{c}{\sigma} \right)^2 \right\} \\
1 &= \int_{\nu_0}^{+\infty} f_{\nu_0}(\nu - \nu_0) d\nu
\end{aligned}$$

4.1.2 Axion signal power excess

Next, supposing we tune our system so that the n -mode of our cavity resonates at the axion signal's frequency. According to eq.63 of [12], the time-averaged power excess due to axion conversion into the n -mode of the cavity will be,

$$P_n = g^2 \rho_a B_z^2 V C_n \frac{1}{m_a} Q_n \quad (16)$$

This power depends on parameters from axion Theory such as the axion coupling constant g , halo axion density ρ_a , or axion mass m_a , and parameters proper to our cavity. C_n is called geometric factor and quantifies the overlap between the static B_z field and the n -mode of the electric field. Since our experiment uses only the first mode of the cavity, let's omit the index n . As P and Q are respectively the received power and the quality factor of the whole system { cavity walls + antenna } also called the "loaded cavity", we will note them with a subscript L. Besides, to include the case where the axion signal's frequency is not aligned with the resonance frequency, we add a correction factor α described in section 4.1.4. So the formula becomes,

$$P_L = g^2 \rho_a B_z^2 V C \frac{\alpha}{m_a} Q_L$$

with P_L , α and m_a that depend on ν_0

Now, we can relate P_L to the power received by the antenna P_A through the constant κ defined as,

$$\kappa \equiv \frac{Q_W}{Q_A}$$

The subscript A refers to the antenna and W to the cavity walls. By definition of the quality factor,

$$Q_X = \frac{\omega_0 U}{P_X} \text{ with } X = L, A, \text{ or } W$$

$$P_X = \left(\frac{dU}{dt} \right) \Big|_X \text{ the power loss through } X$$

The power loss of the loaded cavity is equal to the power loss through the wall plus the power loss through the antenna. In terms of Q factor, this conservation law gives,

$$\frac{1}{Q_L} = \frac{1}{Q_A} + \frac{1}{Q_W}$$

Hence,

$$Q_W = \frac{Q_L Q_A}{Q_A - Q_L}$$

$$\kappa = \frac{Q_L}{Q_A - Q_L}$$

$$Q_L = \frac{\kappa}{\kappa + 1} Q_A$$

$$P_A = \frac{\kappa}{\kappa + 1} P_L$$

Moreover, the data I am using are given by the digital spectrometer (SA). Therefore, the amplifier's gain G must be taken into account. The input power $P_{SA,in}$ at the signal analyzer is,

$$P_{SA,in} = P_A G$$

Thus,

$$P_{SA,in} = \frac{\kappa G}{(\kappa + 1)} g^2 \rho_a B_z^2 V C \frac{\alpha}{m_a} Q_L \quad (17)$$

The coupling constant g is the parameter under hypothetical test. The case where $g = 0$ corresponds to the current Standard Model. The existence of axion is an alternative hypothesis where g is non-zero. All other parameters of the above equation are given by our experimental set-up, numerical simulation, or can be obtained through the analysis of our data. We will determine these parameters one by one in section 4.2 and check their stability, perform a statistical treatment in section 4.4.4 and draw our conclusion in terms of g .

$$g = \sqrt{\frac{P_{SA,in} m_a}{\alpha}} \sqrt{\frac{(\kappa + 1)}{\kappa G \rho_a B_z^2 V C Q_L}} \quad (18)$$

with $P_{SA,in}$, α and m_a that depend on ν_0

In other sections, $P_{SA,in}$ will be noted P_{ν_0} to recall its dependence on ν_0 .

4.1.3 Fitting function

In this section, we want to relate the output power of the signal analyzer $P_{SA,out}$ (our data) to the input power P_{ν_0} . According to the previous section, this total power excess is spread over the frequency. P_{ν_0} is the total axion power received at the input of the spectrum analyzer, i.e. integrated over all frequencies.

$$P_{\nu_0} = P_{\nu_0} \int_{\nu_0}^{+\infty} f_{\nu_0}(\nu - \nu_0) d\nu$$

$$dP_{\nu_0}(\nu) = P_{\nu_0} f_{\nu_0}(\nu - \nu_0) d\nu$$

$P_{\nu_0} f_{\nu_0}(\nu - \nu_0)$ is the energy excess shape we would ideally expect (unit of $W.Hz^{-1} = \text{Joules}$). To obtain the value of this energy for all frequencies, the spectrum analyzer would have to break down our RF signal into an infinite number of perfect sinusoids. Of course, this is impossible. Firstly, filters always have a minimum bandwidth. Secondly, it would not be convenient because it would increase the noise level. Instead, we have a discrete set of frequencies, and for each frequency, the input signal passes through a band-pass filter known as the IF filter. In our measurement system, this filter is of Gaussian shape. The RBW corresponds to half the standard deviation of this Gaussian and is set to $\Delta\nu = 1kHz$. Since the power measured at ν_i contains part of the power of neighboring frequencies, the spectrum analyzer distorts the shape of the excess power. This distortion is not a problem, since the power excess still contains the parameter of interest P_{ν_0} . However, since the SA cannot integrate over an infinite range, there is necessarily a loss of precision. The SA company chooses a parameter x so that,

$$P_{SA,out}(\nu_i) = P_{\nu_0} \int_{\nu_i-x}^{\nu_i+x} f_{\nu_0}(\nu - \nu_0) * \text{gaus}(\nu_i, \Delta\nu) d\nu$$

We don't know the value of x but it is bigger than the RBW. The only thing we can do is to approximate the Gaussian by a rectangle of width $\Delta\nu$ so that this integration becomes,

$$P_{SA,out}(\nu_i) \approx P_{\nu_0} f_{\nu_0}(\nu_i - \nu_0) \Delta\nu$$

$$= P_{\nu_0} \frac{2}{\sqrt{\pi}} \frac{1}{\nu_0 \sqrt{\nu_0}} \left(\frac{c}{\sigma}\right)^3 \sqrt{\nu_i - \nu_0} \exp\left\{-\frac{\nu_i - \nu_0}{\nu_0} \left(\frac{c}{\sigma}\right)^2\right\} \Delta\nu \quad (19)$$

with $\frac{c}{\sigma} = 10^3$ and $\Delta\nu = 10^3 Hz$

4.1.4 Signal search range

Now, the signal analyzer does not receive only the hypothetical axion power excess, but also the cavity response. The latter follows a Lorentzian shape characterized by the quality factor Q_L and a resonance frequency f_r . More details are given section 4.2.3 but we can just mention that higher is Q_L , sharper is the Lorentzian shape. As shown in the previous sections, one can wish to have a high Q_L so that the axion power excess is enhanced, however, this also makes the investigation range smaller as the angle between the signal shape and the Lorentzian slope decreases when away from the resonance frequency. Thus, a high Q reduces the instantaneous search range, but provides greater sensitivity at the resonance frequency. Since the mass range of the axion is very wide, but the sensitivity required for axion QCD is high (small axion signal), we have to make a compromise.

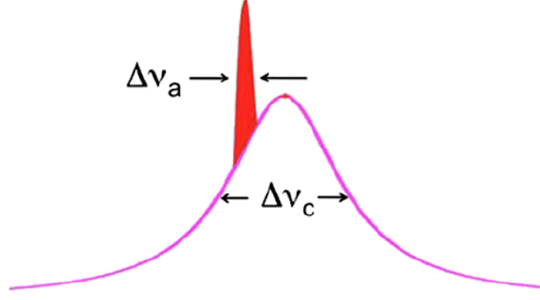


Figure 16: Sketch of axion signal's presence. In red the axion signal, in magenta the Lorentzian response of the cavity.

The figure 16 illustrates the relationship between the quality factor and the signal range. This decrease in sensitivity as we move away from resonance is included in the expression of the signal power through the correction factor α defined as,

$$\alpha(f) = \frac{\Gamma^2}{\Gamma^2 + (f - f_r)^2} \quad (20)$$

4.2 Stability check

To achieve high sensitivity, we have to reduce noise by averaging/compiling a lot of data. However, to do it in a consistent manner, data must be stable. Several aspects can be investigate such as resonance frequency, Q-value, amplifier's gain, noise level, etc. But a first good indicator is temperature fluctuation.

4.2.1 Temperature

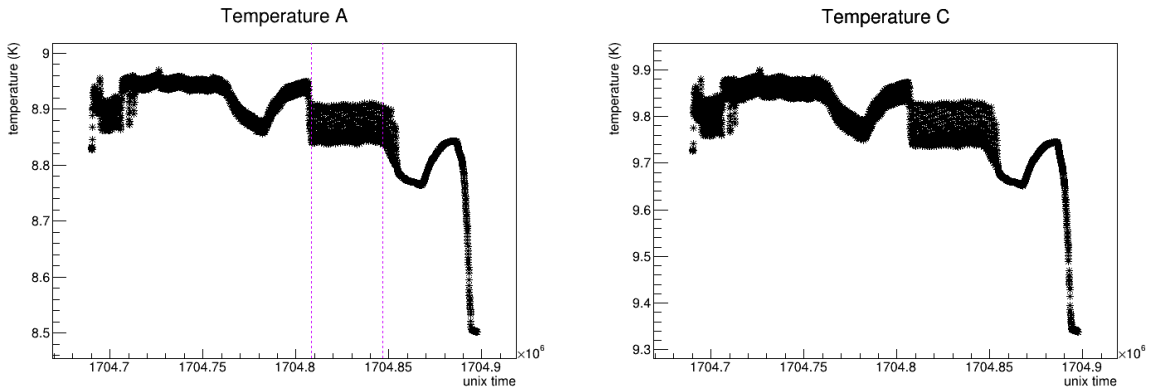


Figure 17: Temperature A (same as temperature B) at the cavity with markers for start and end of compilation area (purple lines) and temperature C at the transfer switch.

The big instabilities correspond to the very first tests of the detector when we were entering the experimental room frequently or moving the cables. They are therefore discarded. Nevertheless, a seemingly stable region (between the purple markers Figure 17) starts around 22:30 on Jan. 9th.

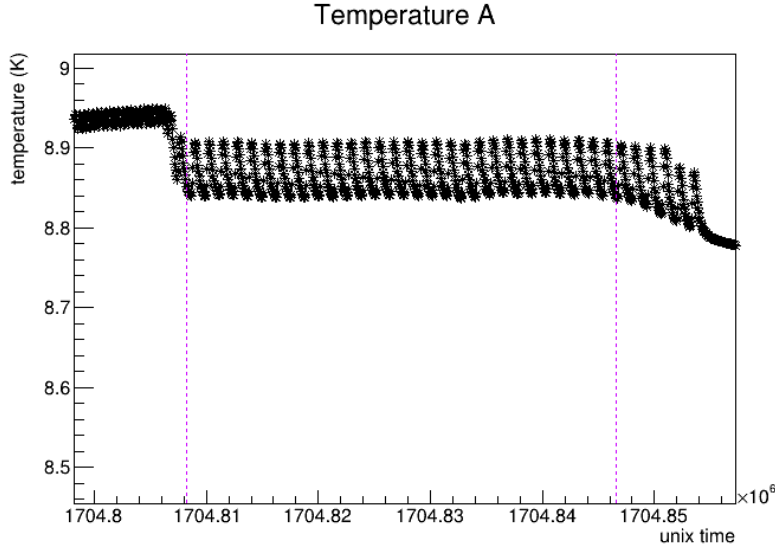


Figure 18: Zoom on the temperature A fluctuation in the chosen compilation region.

When zooming on this region we see a raise of temperature after each calibration. This is probably due to the use of the switch. For the next experiment, we will reduce the frequency of calibrations and rely more on the stability of the amplifier but for this run, we just decide to discard 7 sets (or 14 files) of SA data after each calibration. This number is decided according to logarithmic fits on the SA data. Our method was the following: since there is the same number of physics measurements between each calibration phase in the purple region, we did a two-dimensional compilation over data of the same relative unix time compared to their last calibration and over a small range of frequency. For example, around the frequency bin number 6, and with ± 6 uncorrelated bin along frequency, this process gives the graph Figure 19. Then we fit this result with the following function, proper to temperature behavior,

$$fit(x) = B + (A - B) * exp\left\{\frac{-x}{\tau}\right\}$$

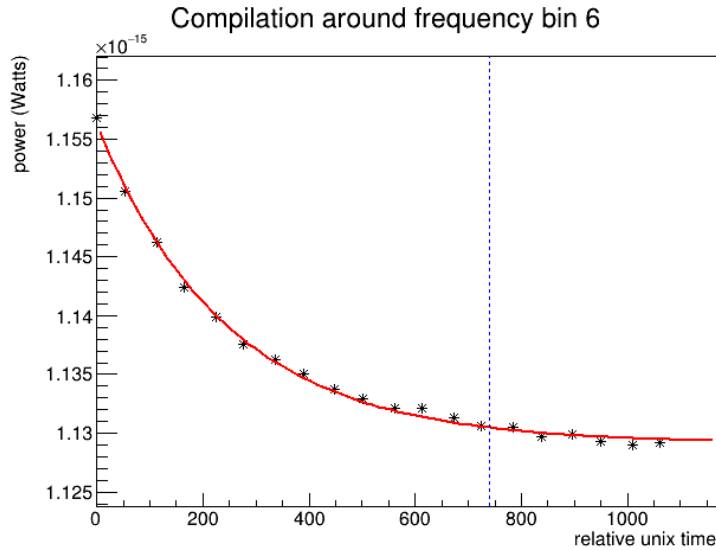


Figure 19: Measured power trend, fitting function (red), value of 3τ (blue line).

In this fitting function, 3σ corresponds to 5% deviation from the value of convergence. This amount is reasonable compared to the statistical fluctuations. Taking this criterion, we are left with the 6 last physics files between each calibration phase, which means 186 files in total, which corresponds to 2 hours 35 minutes. Looking back at the temperature graphs, these files correspond to the intervals highlighted in yellow Figure 20. During this selected periods, the average temperature is of $8.8459 \text{ K} \pm 0.12 \text{ percent}$.

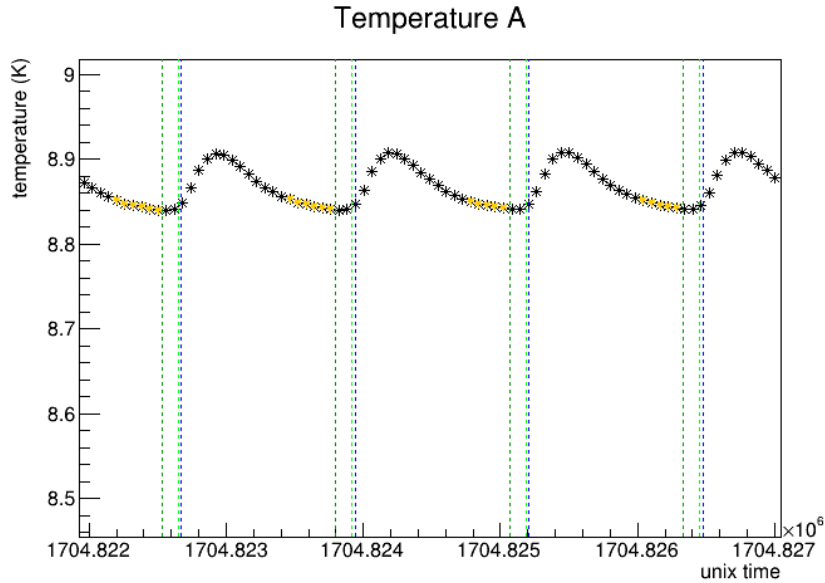


Figure 20: Zoom on temperature fluctuations in the cavity, start of calibration (dark green line), end of calibration (light green line), start of physics measurement (blue line), stable time intervals (yellow).

Now let's see what calibration tells us in the selected region.

4.2.2 Gain

The gain is estimated by a linear fit of NC (cf. section 3.2.8).

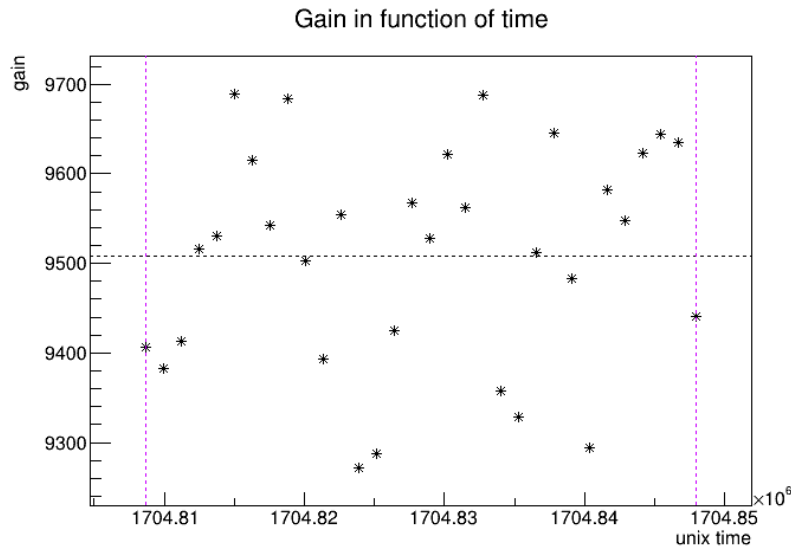


Figure 21: Gain estimates from the calibration with the NC noise source.

$$G = 9509 \pm 1.3\% \quad (21)$$

with 1.3% its standard deviation

The gain measurement has a big uncertainty and if we apply the gain correction to individual SA measurements, the latter are being more scattered than the raw data. Therefore we first compile/average the stable raw data together and use the averaged gain only at the end of our analysis (section 4.4.4), when we will need to relate our results to the axion's coupling constant.

Note also that this gain value is slightly underestimated because the calibration does not take into account the loss of the wire between the green switch and the RF port C Figure 13. However, this does not affect the reliability of our results.

4.2.3 Quality factor and resonance frequency

The electrical behavior of our two port cavity can be characterized by four complex numbers called S-parameters ($S_{11}, S_{12}, S_{21}, S_{22}$). These parameters give the relationships between the incident wave, the reflected wave and the transmitted wave at each port. The S-parameters can be measured with a Vector Network Analyzer (VNA). The values given by the VNA are usually expressed in decibels based on a voltage ratio. By definition, the decibel corresponds to ten times the decimal logarithm of the ratio between two powers. However, as the input and output impedances are matched, it can be effectively expressed in terms of voltage. For example,

$$|S_{21}|_{dB} = 10 \log_{10} \left(\frac{P_2}{P_1} \right) = 20 \log_{10} \left(\frac{V_2}{V_1} \right) = 10 \log_{10} \left(|S_{21}|_{lin}^2 \right)$$

Thanks to this relationship, we see that we can analyze our data with values in decibels (dB) as with the three-dB method, or with linear (lin) values in Watt for which we can more easily find models and fitting functions. The quality factor Q_L of the cavity can be estimated from the measurement $|S_{21}|$ which corresponds to the transmission amplitude from port 1 to port 2. Whereas, the antenna coupling κ is estimated from the reflection coefficient $|S_{22}|$.

Lumped-Element Model

In this section we will work with the linear values and omit the index *lin*. Working with linear values is very convenient because we can apply the superposition theorem. If we assume that the noise and the signal are uncorrelated, the resulting response will be the sum of the two. We will first describe the model of an ideal cavity and add the noise term afterwards.

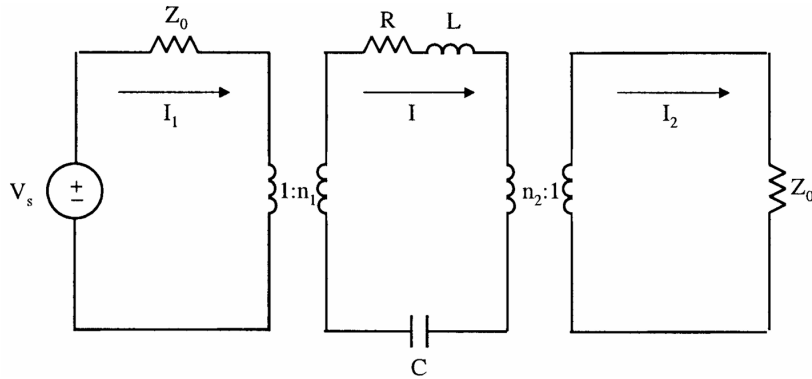


Figure 22: Lumped-element model of a resonant cavity. [68]

According to the demonstration in [68], for weak coupling, the Lumped-element model of the resonant cavity gives,

$$S_{21}(f) = \frac{S_{21}(f_r)}{1 + iQ_L\left(\frac{f}{f_r} - \frac{f_r}{f}\right)}$$

$$|S_{21}(f)|^2 = \frac{|S_{21}(f_r)|^2}{1 + Q_L^2\left(\frac{f}{f_r} - \frac{f_r}{f}\right)^2}$$

This function is not very practical for the fitting process, so we want to get an approximation of it near the resonance frequency. The calculation is in Appendix D and results in:

$$|S_{21}(f)|^2 = \frac{|S_{21}(f_r)|^2}{1 + 4Q_L^2\alpha^2} + \mathcal{O}(4|S_{21}(f_r)|^2Q_L^2\alpha^3) \quad \text{with} \quad \alpha = \frac{f - f_r}{f_r}$$

Therefore, near resonance, the lumped-element model becomes,

$$|S_{21}(f)|^2 = \frac{|S_{21}(f_r)|^2}{1 + 4Q_L^2\left(\frac{f}{f_r} - 1\right)^2}$$

Which can be re-written as,

$$|S_{21}(f)|^2 = \frac{A}{\Gamma^2 + (f - f_r)^2} \quad \text{with} \quad \Gamma \equiv \frac{f_r}{2Q_L} \quad \text{and} \quad A \equiv |S_{21}(f_r)|^2 \Gamma^2$$

We recognize a Cauchy distribution, usually called Lorentzian function in physics. Now, according to the superposition theorem, we can just add the noise to the Lumped-element model. In first approximation, we consider this noise to be linear.

$$|S_{21}(f)|^2 = \frac{A}{\Gamma^2 + (f - f_r)^2} + p0 + p1(f - f_r) \quad (22)$$

Note that, instead of $p1f$ we use $p1(f - f_r)$ to avoid very small values for $p1$ that would lead to imprecise estimation.

3dB method

Although fitting with Lorentz function may be more precise, it is less robust than the 3dB method. The fitting function alone is highly dependent on parameters' initialization. Therefore, we first use the 3dB method to select the input parameters of the Lorentz fit.

The 3dB method gives us a first estimation of Q-value by the following relation.

$$Q_{3dB} = \frac{f_r}{\Delta f}$$

The bandwidth Δf corresponds to the frequency range where the attenuation of the signal response is 3 dB less than the maximum signal. It is determined by linear interpolation. Respectively, on the graph of $|S_{21}(f)|_{lin}^2$, it is approximately equal to the so-called FWHM, which corresponds to a halving of the maximum.

$$|S_{21}(f)|_{dB} - 3 \approx 10 \log_{10} \left(\frac{|S_{21}(f)|_{lin}^2}{2} \right)$$

Lorentz fit

The Q-value estimated with the 3dB method and the resonance frequency given by the VNA apparatus are used as initial parameters in the Lorentz fit. Besides, the initial p_0 is taken equal to the power value at the first frequency bin.

Lorentz fit initial values

$$\Gamma = \frac{f_r}{2 * Q_{3dB}}$$

$$A = (|S_{21}(f_r)|^2 - p_0) * \Gamma^2$$

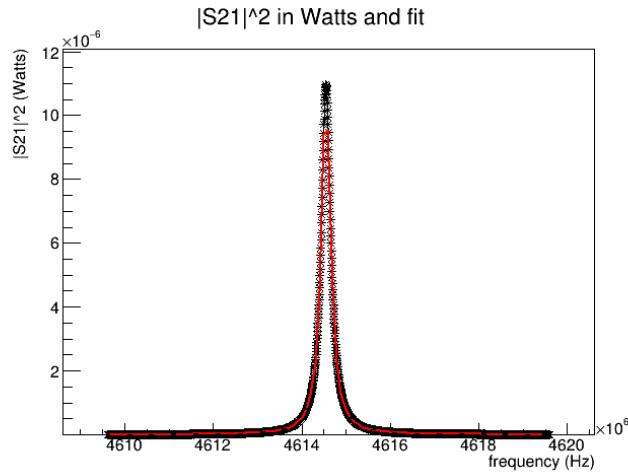


Figure 23: Example of VNA data $|S_{21}|^2$ in Watts. Lorentz fit in red.

After fitting all the pre-selected files, we examine the stability of the resonance frequency and Q_L value estimates. To do so, we calculate the maximum shift or "drop" produced by their fluctuations.

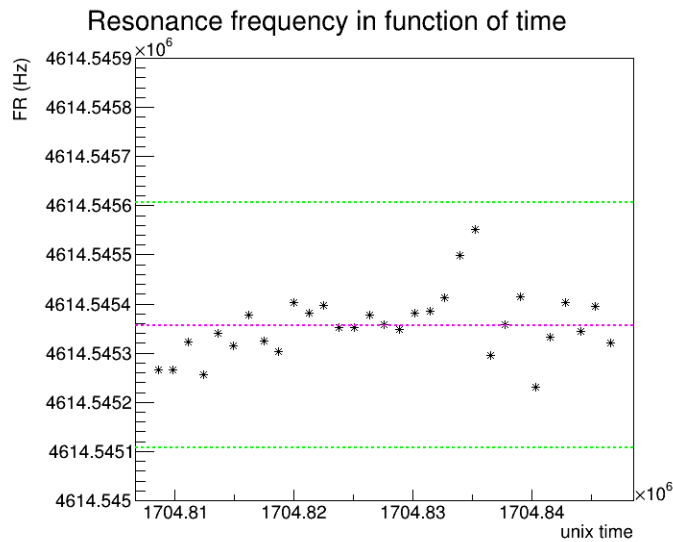


Figure 24: Resonance frequency estimate fluctuations during compilation interval. Purple marker is the average $\langle f_r \rangle$ of the fitting results over time and green markers show $\langle f_r \rangle \pm 0.001 * \langle f_r \rangle / Q$

As Figure 24 shows, all Lorentz fits give a resonance frequency that does not deviate from the mean for more than $0.001 * \langle f_r \rangle / Q_L$.

$$\frac{A}{\Gamma^2 + (0.001 * \frac{f_r}{Q_L})^2} = \frac{A}{\Gamma^2(1 + 4 * 10^{-6})} = \frac{|S_{21}(f_r)|^2}{1 + 4 * 10^{-6}}$$

$$drop(\text{due to } \Delta f_r) = |S_{21}(f_r)|^2 - \frac{|S_{21}(f_r)|^2}{1 + 4 * 10^{-6}} < 4 * 10^{-6} |S_{21}(f_r)|^2$$

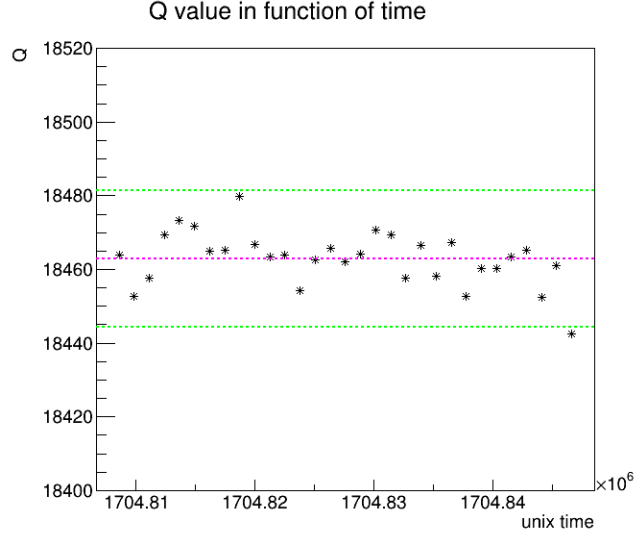


Figure 25: Q value estimate fluctuations during compilation interval. Purple marker is the average $\langle Q_L \rangle$ of the fitting results over time and green markers show $\langle Q_L \rangle \pm 0.001 \langle Q_L \rangle$

$$\frac{\partial}{\partial Q_L} \left[\frac{|S_{21}(f_r)|^2 \Gamma^2}{\Gamma^2 + (f - f_r)^2} \right] = -\frac{f_r^2}{2Q_L^3} \frac{|S_{21}(f_r)|^2 (f - f_r)^2}{\left[\left(\frac{f_r}{2Q_L} \right)^2 + (f - f_r)^2 \right]^2}$$

$$drop(\text{due to } \Delta Q_L) \leq 2 * 10^{-6} |S_{21}(f_r)|^2$$

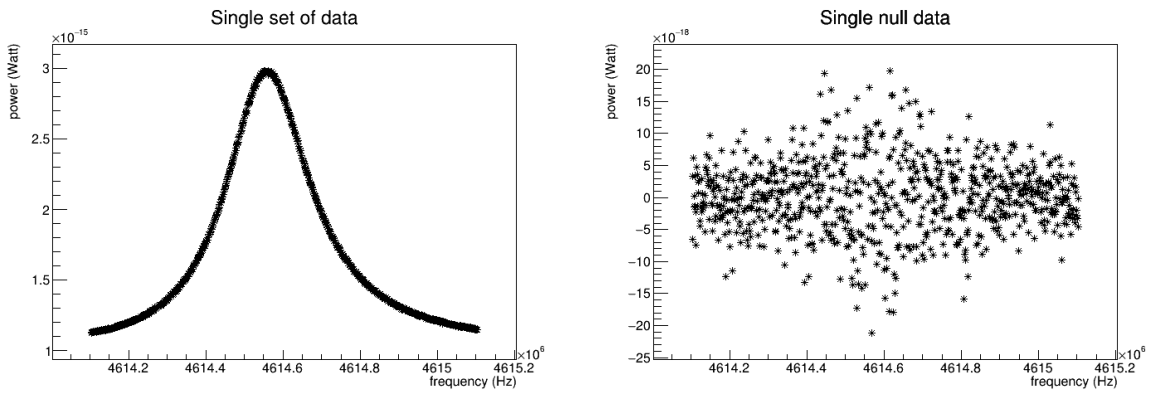


Figure 26: Compilation of one set (ie 2 successive files) on the left graph and its statistical fluctuation on the right graph

According to Figure 26 the statistical fluctuations are at least of about,

$$100 * \frac{5.6 \times 10^{-18}}{3^{-15}} = 0.19\%$$

The statistical fluctuations are much bigger than the effect of Q_L or f_r fluctuations so the quality factor and the resonance frequency are stable enough and we have

$$Q_L = 18463 \pm 0.12\% \quad (23)$$

$$f_r = 4.614545357 \times 10^9 \pm 3.8 \times 10^{-6}\% \quad (24)$$

4.2.4 Antenna coupling

Another S-parameter is used to characterize the cavity response. The vector network analyzer sends a wave from port 2 and measures the reflected wave that comes back. The ratio is the complex number S_{22} . We plot it in a two-dimensional plan as shown Figure 27. Those kind plots are called Smith Charts. By circle fittings of these two circles, we can estimate the antenna coupling kappa introduced section 4.1.2.

$$\kappa = \frac{1}{\frac{D}{d} - 1} \quad [69]$$

with,

d = diameter of the ON resonance circle

D = diameter of the OFF resonance circle

The factor that appears in the axion power (17) is,

$$\frac{\kappa}{\kappa + 1} = \frac{d}{D}$$

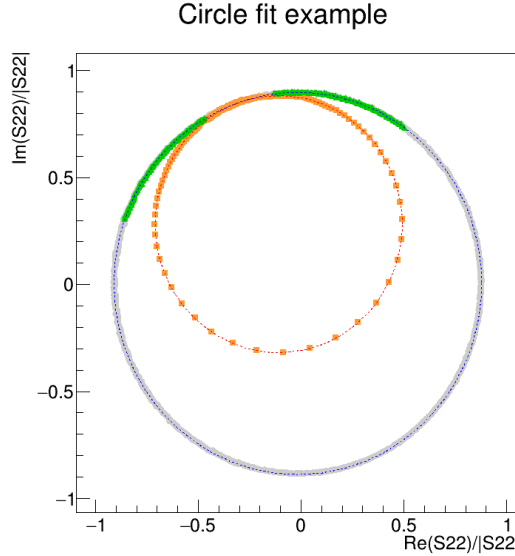


Figure 27: Circle fitting ranges in green (resp. orange) and fit results in blue (resp. red) dotted lines for OFF resonance (resp. ON resonance) circle.

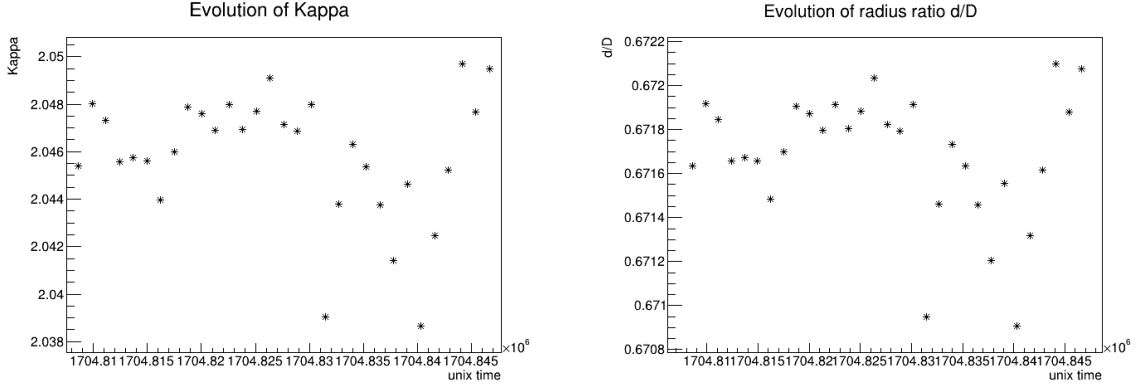


Figure 28: The time evolution of κ on the left graph and of $\frac{\kappa}{\kappa+1}$ on the right graph

$$\frac{\kappa}{\kappa+1} = 0.67168 \pm 0.12\% \quad (25)$$

The antenna was set to critical coupling in room temperature, but is now over-coupled in cryogenic conditions. We do not have any tuning system for the antenna to correct the over-coupling.

4.3 Digital spectrometer data treatment

In a signal analyzer data we see two kinds of fluctuations. There is a "global" shape that looks Lorentzian as expected and "local" fluctuations that are mainly due to the statistical nature of physics. Hidden in this data, we may have an axion signal.

4.3.1 Compilation

To find a signal, we first have to reduce the statistical fluctuations (i.e. improve the signal-to-noise ratio) by taking the average of several digital spectrometer data together. Of course, not all data can be compiled. They must be stable enough to give a reliable result. This stability has been investigated in 4.2. We can now compile the selected data together.

We make two kinds of compilation. One is just a simple average, the other one, called "null" data, aims at describing pure statistical fluctuations. Since data files come in sets of two, we will call successive files: 1 and 2. The next set is noted $\{1', 2'\}$ and so on. To make the null data we subtract 2 to 1 and change the order after each calibration, which means subtracting 1 to 2. This avoids bias due to the logarithmic trend observed Figure 19.

$$\begin{aligned} \text{Simple compilation} & \quad \frac{1 + 2 + 1' + 2' + \dots}{\text{number of files}} \\ \text{Null compilation} & \quad \frac{1 - 2 + 1' - 2' + \dots + 2'' - 1'' + \dots}{\text{number of files}} \end{aligned}$$

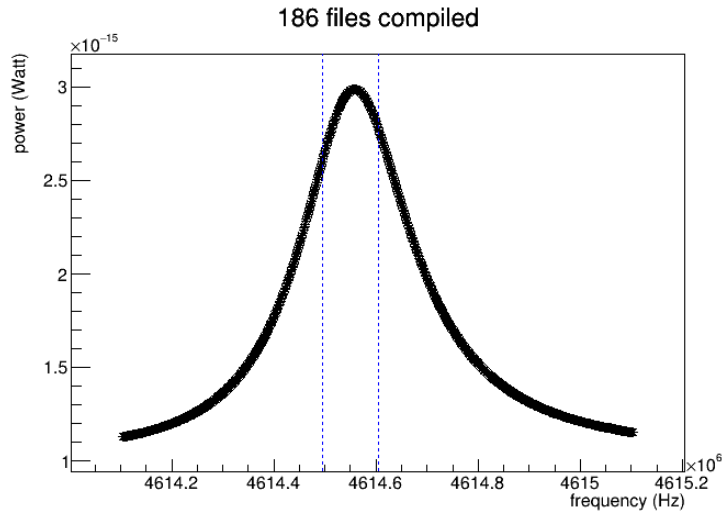


Figure 29: Signal data with the final search range between blue markers. Uncorrelated frequencies only.

Note that the original binning is smaller than the RBW (1 kHz) so that to have uncorrelated frequencies we need to skip 4 points every 5 bins. Thus, our closest uncorrelated points have a spacing of about 1221 Hz. For future experiment, we can consider optimizing the binning by taking a bin space just slightly above the RBW.

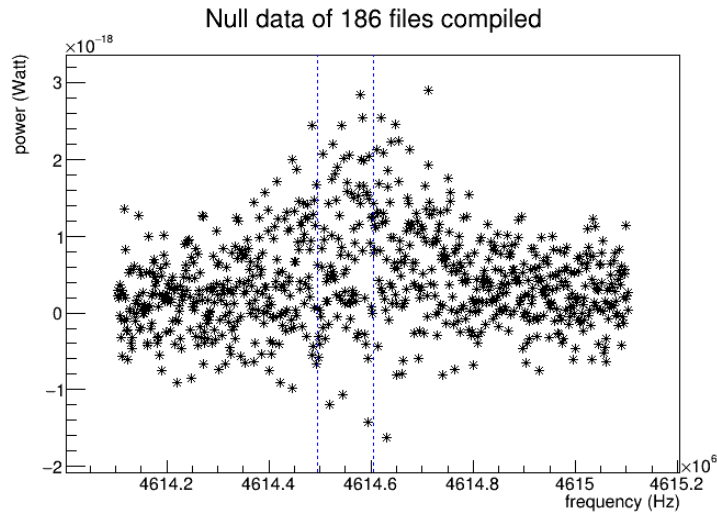


Figure 30: Null data with the final search range between blue markers. Uncorrelated frequencies only.

Figure 30 shows that the statistical fluctuations are bigger on the center of the range than on the borders.

4.3.2 Background fitting

Now, to treat this global background shape, we make once again a Lorentz fit. For the initial parameters, we can use the Q value and resonance frequency previously estimated on the VNA data as they are expected to be similar. We obtain the following residuals.

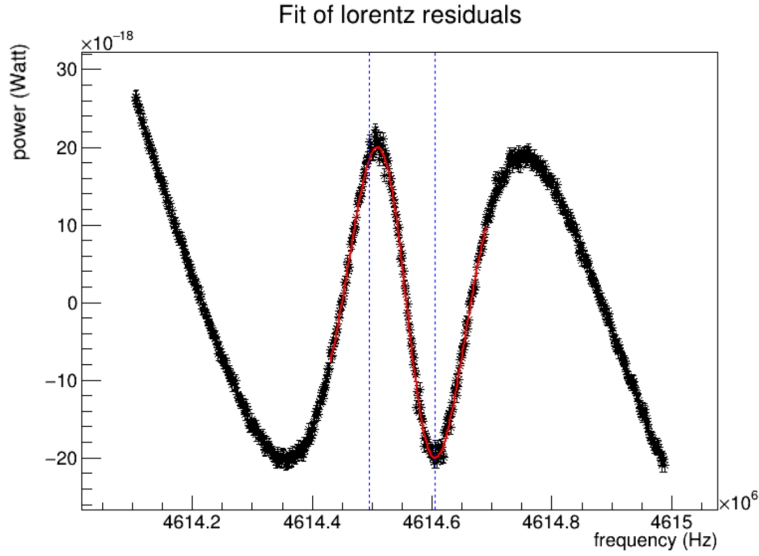


Figure 31: Residuals of Lorentz fit on SA data with new fit in red and final search range between blue markers

Lorentz fit residuals are fitted with the following function.

$$fit(x) = A * \sin\left(\frac{\pi}{\beta + \alpha * (x - shift)} * (x - shift)\right) + (x - shift) * B$$

This function can be explained by a frequency-dependent shift of the OFF resonance circle center as illustrated Figure 32.

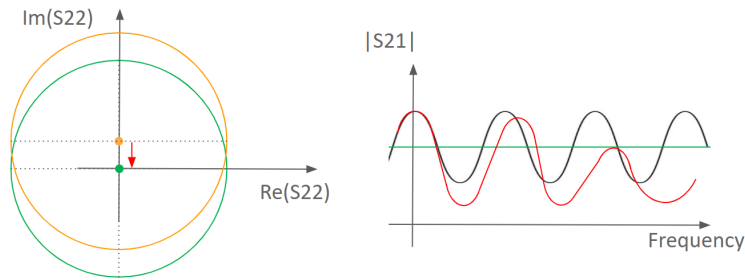


Figure 32: This figure illustrates three basic cases: no center shift (straight green line), a fixed center shift (perfect sinusoidal function in gray), and a frequency-dependent shift which would result in a distorted sinusoidal function (in red).

Whether this assumption is true or not, the width of the axion signal is in any case much smaller than this sinusoidal shape, so the latter can be considered as background and safely removed.

4.4 Statistical analysis

For this part, a detailed methodology can be found in [70].

We define the so-called Null-hypothesis H_0 and Alternative-hypothesis H_1 as,

$$H_0 = \text{the Standard Model is true}$$

$$H_1 = \text{the axion signal presence}$$

4.4.1 Signal and Null samples

From the stability check 4.2 and the two fittings 4.3, results the data Figure 33. In this plot, we might have an axion signal. It could be located at any frequency. However, we need a sufficient number of points on the sides to have a well-estimated baseline of the signal. Therefore, our search range is reduced to the interval between the blue markers. All frequencies of this interval will be tested.

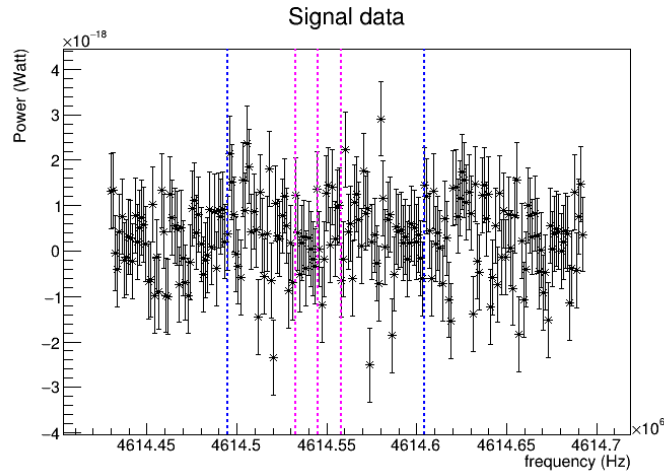


Figure 33: Residuals after background fit and the signal search range between blue markers.

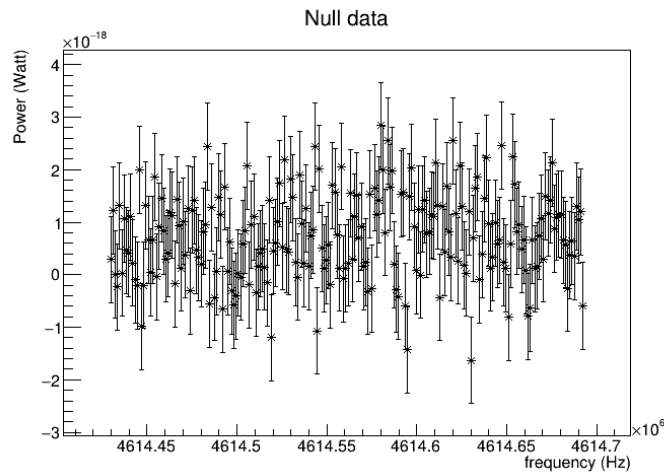


Figure 34: Null data sample on the same range as the final signal data sample. It is just a zoom of Figure 30 and made as explained section 4.3.1

The error bars are \pm the standard deviation of the null sample data points Figure 34, that is: $8.2 * 10^{-19}$ Watts. It is the only use of null data sample in this analysis.

We make the signal fit for each frequency of the signal data sample Figure 33. We decide to start the scan from 1/4th to 3/4th of the total range to keep a sufficient number of points for the signal shape baseline. The limits of the scan are indicated by blue markers. Each fit gives the best estimation of the axion power P_{ν_0} we note \hat{P} . The fitting algorithm returns the minimum chi square $\chi^2_{min} = \chi^2(\hat{P})$.

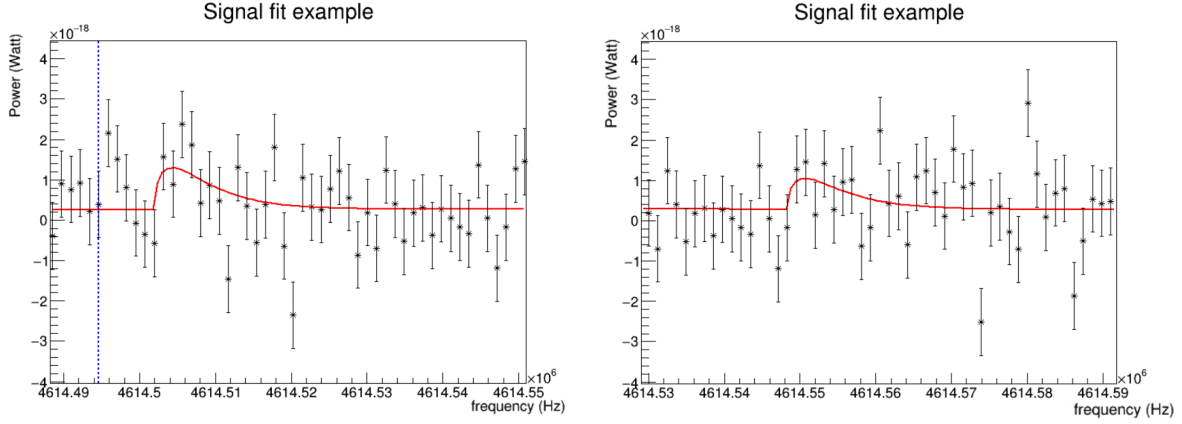


Figure 35: Two example of signal fit results. The signal on the left graph is our best candidate and has a local p value of 6.96×10^{-3} . The right graph gives an other example but less significant, with a local p value of 4.24×10^{-2} .

4.4.2 Confidence intervals

To make a confidence interval around P estimate, we need to know the sensitivity of the fit's quality as P varies for a given ν_0 . In other words, we will look at the variation $\Delta\chi^2$ defined as,

$$\Delta\chi^2(P) = \chi^2(P) - \chi^2(\hat{P})$$

Since we are only varying one parameter of interest, $\Delta\chi^2$ follows a χ^2 distribution with "one degree of freedom" (The background parameters p0 and p1 are left free during the fit but does not count as degree of freedom) Thanks to this distribution, we can relate our results to probabilities.

Let's choose a confidence level (CL) of 90%. This choice, although arbitrary, must be remembered when communicating the final results. 0.90 is equal to the integral of the chi-square probability density function for one degree of freedom from 0 to $c = 2.71$.

$$\begin{aligned} CL &= 90\% \\ \text{or significance level } \alpha &= 1 - CL = 10\% \\ \text{1 degree of freedom} \\ c &= 2.71 \end{aligned}$$

For each axion power estimate, we determine the range of power values for which $\Delta\chi^2$ is smaller than c . This range is called the confidence interval (CI) and the borders of this interval are naturally called upper limit and lower limit.

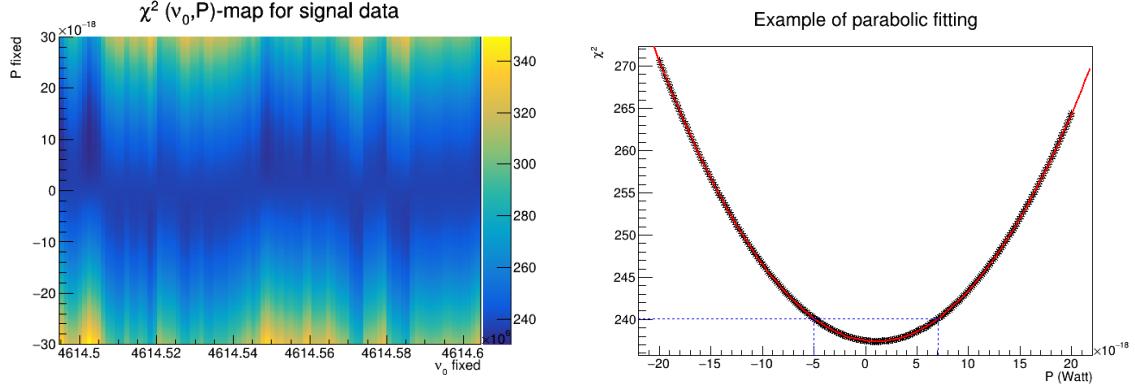


Figure 36: Left graph shows all the resulting χ^2 values from fitting with fixed axion frequency ν_0 and fixed P . Right graph shows a slice of the left graph at a given ν_0 . A parabolic fit is performed on it and the markers corresponds to the borders of the confidence interval at $c = 2.71$.

Concretely, we fit with a parabola

$$A(p - B)^2 + C(p - B) + D = \chi^2$$

And solve the equation for $\chi^2 - \chi_{min}^2 = c$ to get the borders of the confidence intervals. After doing this for all frequencies of the search range, we obtain Figure 37 .

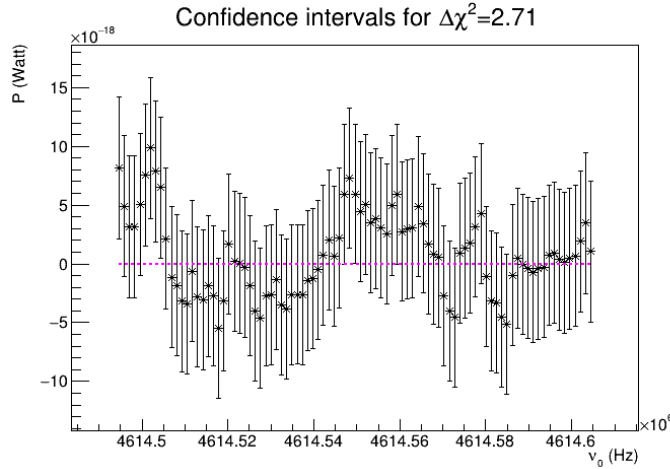


Figure 37: Confidence intervals at 90%CL along the our search range.

Physically it means that, if we were to repeat the measurement an infinite number of times, 90% of the confidence intervals would contain the Null Hypothesis value ($P=0$, ie. the Standard Model) and 10% would not, simply by the effect of statistics. As expected, some intervals do not contain the null hypothesis, but to find out whether this is chance or an axion signal, we need to perform another test.

4.4.3 Hypothetical test of non-zero P hypothesis

The axion signal can only be positive so we can define our statistical test as follow,

$$q(m) = \begin{cases} \chi^2(0, m) - \chi^2(\hat{P}, m) & \text{if } \hat{P} \geq 0. \\ 0 & \text{if } \hat{P} < 0, \end{cases}$$

with m the axion's frequency/or mass

Since axion can exist only at one frequency, we can just take the strongest argument against the Null hypothesis (smallest pValue) and test it. Our best chance to have an axion signal is at the frequency where $q(m)$ is maximal. We define,

$$u \equiv \max_m(q(m))$$

In our data, the biggest χ^2 distance among positive signals is,

$$u = 7.28$$

$$\text{at } m = 4.614501949 \text{ GHz}$$

We can calculate the corresponding local pValue and local Z-score,

$$p_{\text{local}} = 1 - \int_0^u \chi_1^2(x) dx = 6.96 \times 10^{-3}$$

$$Z_{\text{score local}} = \Phi^{-1}\left(1 - \frac{p_{\text{local}}}{2}, 1\right) = 2.69$$

note that $u = Z^2$ in our case

A Z-score of 2.69 is significant under 90% confidence level because it is higher than $\sqrt{\Delta\chi^2} = \sqrt{2.71}$, but before concluding, we must consider that we searched over a certain range and therefore made several ‘‘attempts’’. As a result, the significance of our signal is actually lower. This is called the look-elsewhere effect. Once this effect has been taken into account, the pValue is said to be global.

In [71], Eilam Gross gives a technic to obtain an approximation or at least a majoration of the global pValue. In the following demonstration, all probabilities are supposing the Null hypothesis.

$$p_{\text{global}} = P(\max_m(q(m)) > u)$$

$$= P\left(\bigcup_m q(m) > u\right)$$

$$= P(q(0) > u) + P\left(\bigcup_{m \geq 1} q(m) > u\right) - P(q(0) > u \cap \bigcup_{m \geq 1} q(m) > u)$$

$$\leq P(q(0) > u) + P\left(\bigcup_{m \geq 1} q(m) > u\right)$$

And,

$$P(q(0) > u) = \frac{1}{2}P(\chi_s^2 > u) \quad \text{with } s \text{ the number of degrees of freedom or dimension}$$

$$P\left(\bigcup_{m \geq 1} q(m) > u\right) = P(\mathcal{N}_u > 0) \quad \text{with } \mathcal{N}_u \text{ the number of up-crossings by } q \text{ above } u$$

Besides, $P(\mathcal{N}_u > 0) \leq \langle \mathcal{N}_u \rangle$ and,

$$\langle \mathcal{N}_u \rangle = \langle \mathcal{N}_1 \rangle u^{(s-1)/2} e^{-u/2}$$

$$\langle \mathcal{N}_{c_0} \rangle = \langle \mathcal{N}_1 \rangle c_0^{(s-1)/2} e^{-c_0/2}$$

with c_0 an arbitrary low level

So,

$$p_{\text{global}} \leq \frac{1}{2}P(\chi_s^2 > u) + \langle \mathcal{N}(c_0) \rangle \left(\frac{u}{c_0}\right)^{(s-1)/2} e^{-(u-c_0)/2} \quad (26)$$

with s the number of degrees of freedom or dimension

In our case $s = 1$ because we vary only one parameter which is P . Besides, $P(\chi_s^2 > u)$ is simply p_{local} calculated before. However, $\langle \mathcal{N}(c_0) \rangle$ requires Monte-Carlo data. In our analysis, a

Monte-Carlo data sample consists in Gaussian distributed data points along our search range of frequency and with as standard deviation, the one of the Null data sample Figure 34. In other words, it is artificial data assuming the null hypothesis to be true, or, we might say, artificial background data.

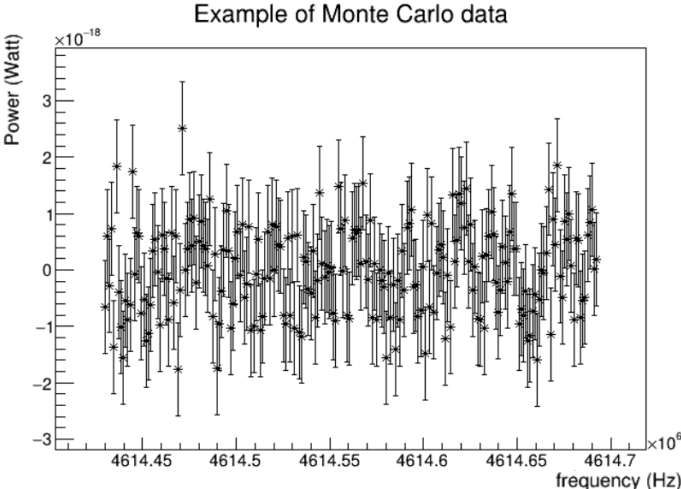


Figure 38: Example of one Monte-Carlo data

We simulate 1000 Monte Carlo of this type and scan each of them with our statistical test. During each scan, we count the number of up-crossings of our test q above a level c_0 . The average of this number over the Monte Carlo samples is $\langle N(c_0) \rangle$. Of course, the higher is the level c_0 , the smaller is the number of up-crossings (Figure 40).

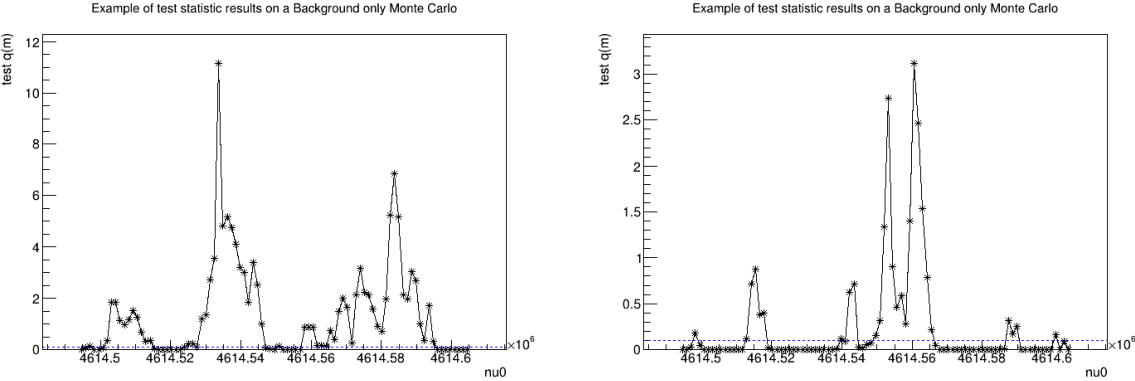


Figure 39: Two examples of test statistics along the search range on Monte Carlo data. The example on the right corresponds to the Monte Carlo showed Figure 38. The blue marker is the arbitrary c_0 choice.

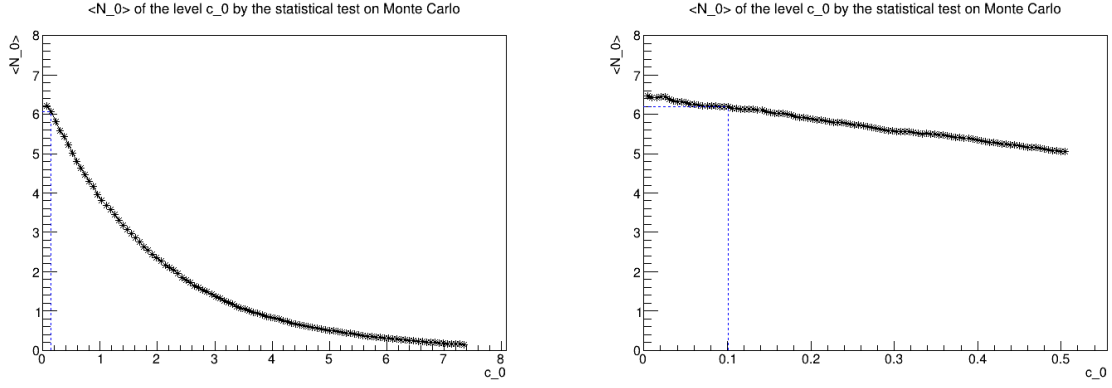


Figure 40: Average number of up-crossings in function of the level c_0 . Right graph is just a zoom. The blue marker is the arbitrary c_0 choice.

Now, if we multiply by the exponential factor, as in the formula (26), the extra term becomes independent of c_0 . In fact, the choice of c_0 is not of great importance. It is convenient to have a small c_0 because we have more up-crossings, and so better statistics. But it cannot be too small either because our test q has a limited precision (tolerance 0.01 cf. Appendix C). We can choose, for example, $c_0 \approx 0.1$.

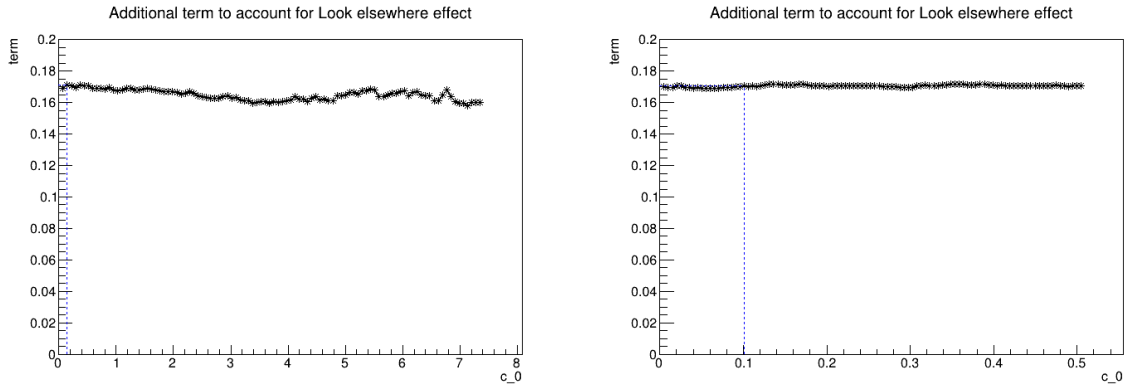


Figure 41: Second term of equation (26) in function of the level c_0 . Right graph is just a zoom. The blue marker is the arbitrary c_0 choice.

So finally, when considering the look-else where effect, the significance of our signal candidate get down to :

$$p_{\text{global}} \leq 1.74 \times 10^{-1}$$

$$Z_{\text{score}}_{\text{global}} = \Phi^{-1}\left(1 - p_{\text{global}, 1}\right) \geq 0.94$$

Note that these inequalities tend to equalities for high significance. But anyway, this result shows that our signal is not significant at the 90% confidence level, as we cannot assert that the global Z-score is greater than $\sqrt{2.71}$. We can forget the non-zero P hypothesis and admit the null-hypothesis.

4.4.4 Rejection line

We want the rejection line in terms of axion coupling constant. According to equations (17) and (19), we can fit $P_{SA,out}$ with the following function that depends on the coupling constant g .

$$fit(\nu_i) = p_0 + p_1(\nu_i - \nu_0) + \frac{\kappa G}{(\kappa + 1)} g^2 \rho_a B_z^2 V C \frac{\alpha}{m_a} Q_L \frac{2}{\sqrt{\pi}} \frac{1}{\nu_0 \sqrt{\nu_0}} \left(\frac{c}{\sigma}\right)^3 \sqrt{\nu_i - \nu_0} \exp\left\{-\frac{\nu_i - \nu_0}{\nu_0} \left(\frac{c}{\sigma}\right)^2\right\} \Delta\nu$$

with $c = \hbar = 1$; $\frac{c}{\sigma} = 10^3$; $\Delta\nu = 10^3 Hz$; and $\alpha(f) = \frac{\Gamma^2}{\Gamma^2 + (f - f_r)^2}$

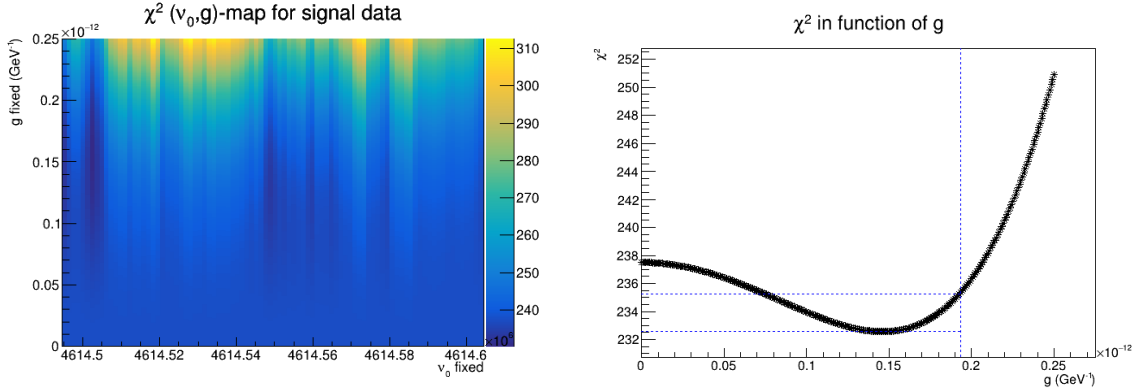


Figure 42: The left graph shows all the resulting χ^2 values from fitting with a fixed axion frequency ν_0 and a fixed g . The right graph shows a slice of the left graph at a given ν_0 . The markers corresponds to the borders of the rejection line at $\chi^2 - \chi_{min}^2 = c = 2.71$.

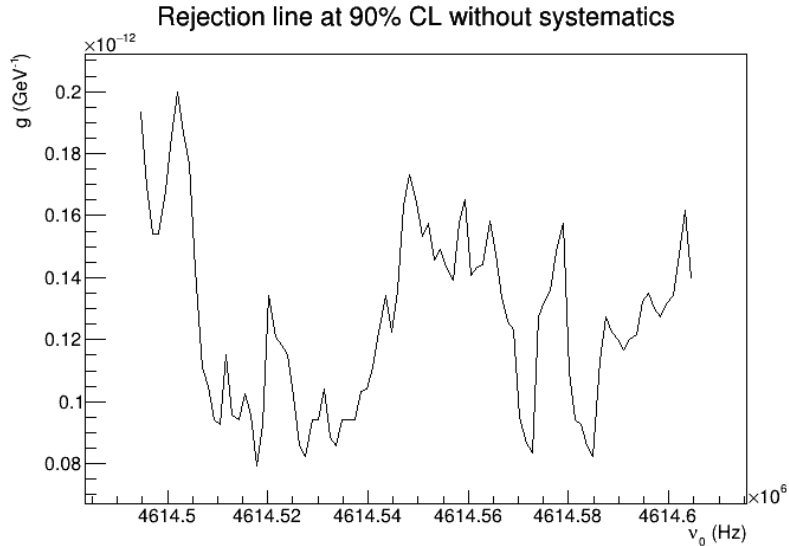


Figure 43: Rejection line with 90% CL, systematics not considered.

4.4.5 Systematics and final result

Before concluding, we need to take into account the systematic errors. The following table summarizes the errors for each parameter that composes the axion signal.

Error Budget		
Parameter Name	Value	Relative Error
Gain G (21)	9509	$\pm 1.3\%$
Axion Energy Density ρ_a (8)	0.45 GeV/cm^3	Omitted
Magnetic Field B_z (14)	8.76 T	$\pm 0.9\%$
Volume V (12)	370.87 cm^3	$\pm 0.8\%$
Geometric Factor C (13)	0.605	$\pm 0.15\%$
Quality Factor Q_L (23)	18463	$\pm 0.12\%$
Axion Mass m_a	$2\pi\nu_0$	Negligible
$\kappa/(\kappa + 1)$ (25)	0.67168	$\pm 0.12\%$
Resonance Frequency (24)	4.614545357 GHz	$\pm 3.8 \cdot 10^{-6}\%$

Table 5: Summary of the error budget for axion signal parameters and their contributions.

According to equation (18), we apply the error propagation formula,

$$\begin{aligned}
 \frac{\Delta g}{|g|} &= \sqrt{\frac{1}{2} \left(\frac{\Delta G}{G} \right)^2 + \left(\frac{\Delta B_z}{B_z} \right)^2 + \frac{1}{2} \left(\frac{\Delta V}{V} \right)^2 + \dots} \\
 &= \sqrt{\frac{1}{2} 1.3^2 + 0.9^2 + \frac{1}{2} 0.8^2 + \dots} \quad \% \\
 &= 1.4\%
 \end{aligned}$$

Thus, the rejection line is loosen to the final result Figure 44.

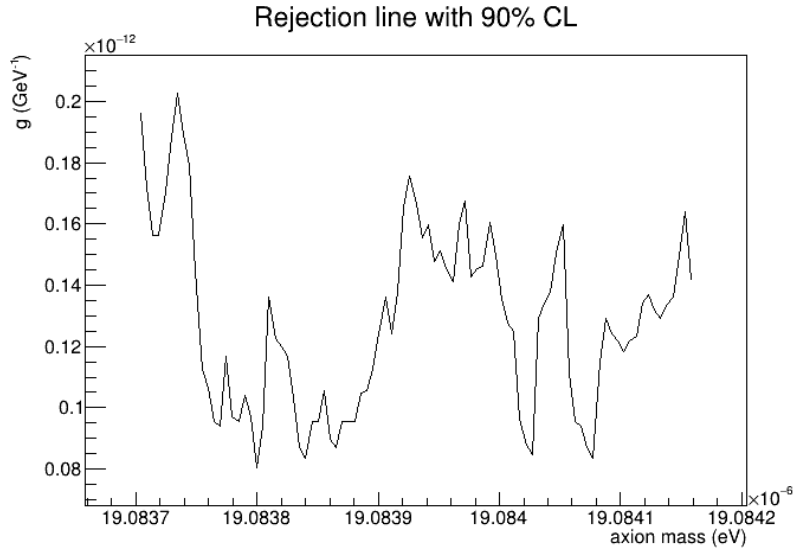


Figure 44: Rejection line with 90% CL with systematics taken into account

The most stringent limit on $g_{a\gamma\gamma}$ is $8 \times 10^{-14} \text{GeV}^{-1}$ at $1.908380 \times 10^{-5} \text{ eV}$ and the worst limit is $2.03 \times 10^{-13} \text{GeV}^{-1}$ at $1.908373 \times 10^{-5} \text{ eV}$ in Figure 45.

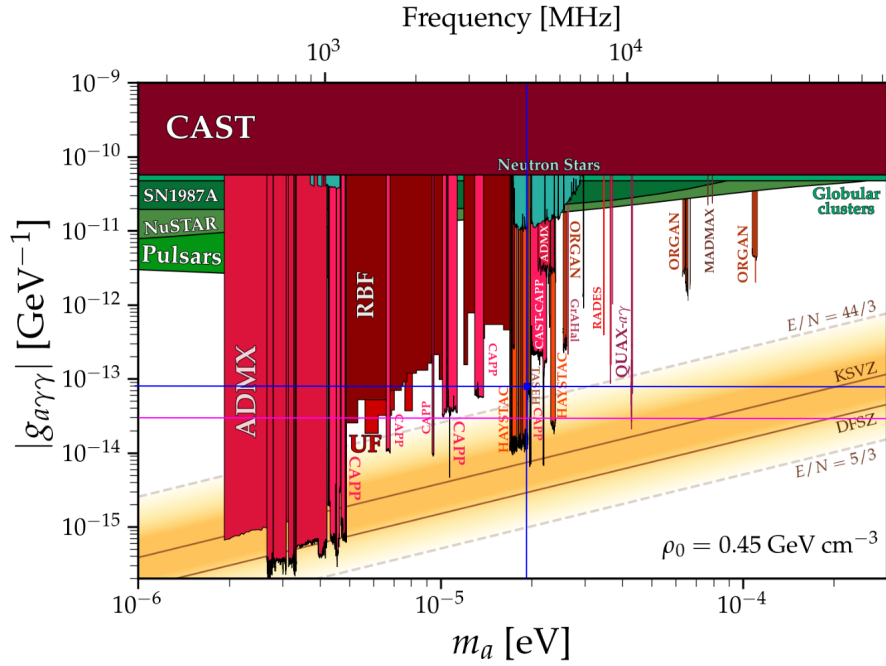


Figure 45: Our most stringent limit position in blue. HAYSTAC Phase II-c/d [58] approximate limit in pink. graph adapted from [38].

Conclusion

Our first experiment produced great results, with a sensitivity already reaching a region of axion parameter space that was still unexplored until a few months ago. Assuming axion to be the only component the thermal dark matter halo of our galaxy, our results exclude the trapped misalignment mechanism for the axion mass range $[1.908370397, 1.908415832] \times 10^{-5}$ eV. Our most stringent limit on $g_{a\gamma\gamma}$ is $8 \times 10^{-14} \text{GeV}^{-1}$ at 1.908380×10^{-5} eV and the worst limit is $2.03 \times 10^{-13} \text{GeV}^{-1}$ at 1.908373×10^{-5} eV.

5 Prospects

A new experiment has been launched at the end of November with several improvements. In particular, the cavity can now be tuned by a copper bar moving vertically.

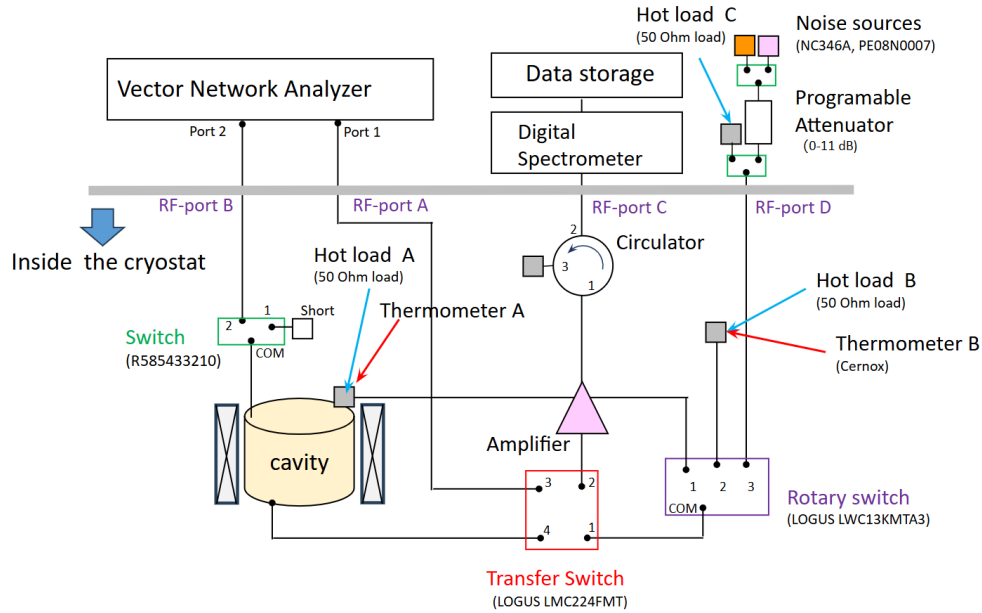


Figure 46: Circuit diagram of November set up

Some 50Ohm noise sources with a new mechanical switch (purple) are added for a better calibration. The electronics and cavity that enter the cryostat can be seen Figure 47. They held by the same column as the previous experiment.

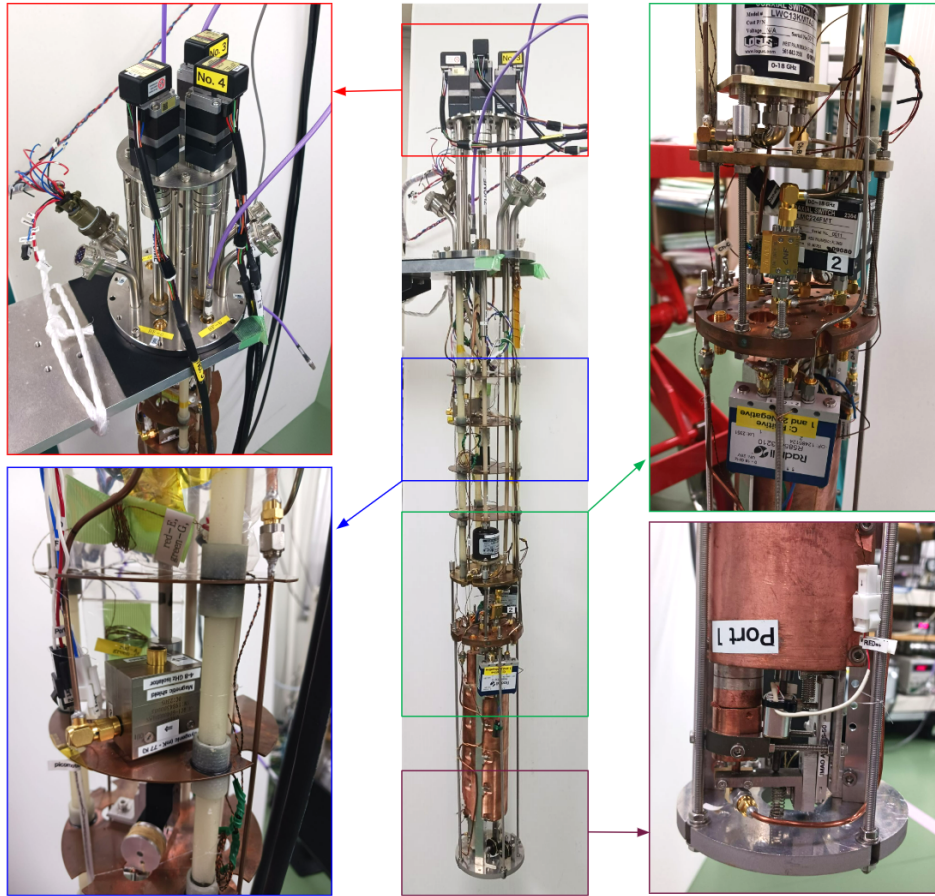


Figure 47: Pictures of the set up. In the top-left picture (red) are the shafts used to control the rotary switch, the transfer switch and the tuning rod. The bottom left picture (blue) shows the circulator and the wheel used to move the tuning rod. The Rotary switch, Transfer switch, and Common Positive switch are visible in the top right picture. Finally, the bottom right picture shows the antenna port.

The shafts on the top left picture are used to control a number of elements from outside the cryostat. Indeed, the intense magnetic field requires the use of purely mechanical systems whose functionality is not affected by the magnetic field. Shaft number four controls the rotary switch, shaft number three the transfer switch, and shaft number five the wheel. The “Common Positive” switch, by contrast, uses the magnetic field to change configuration. In the absence of a magnetic field, it is set to COM-2, enabling calibration, and when the magnetic field is applied, it switches to the COM-1 configuration (i.e. short-circuit), necessary for measurements.

This experiment, which was launched in November 2024, had some problems, particularly with the amplifier. We are currently solving these issues and will re-run the experiment at around 4.6 GHz for validation.

In parallel, we are preparing a new cavity to investigate the region around 7.5 GHz ($3.1 \mu\text{eV}$). An experiment will be launched in March as soon as the cavity is received. As for the long term, we plan to upgrade the magnet and the cryostat. We want to use a 9.4T magnet with a 340mm room-temperature bore at the High Field Laboratory for Superconducting Materials of the Institute for Materials Research of Tohoku University. Thanks to this large room-temperature bore, we will install a newly developed superfluid helium cryostat whose cold bore is of 290 mm. The 290 mm cold bore can accommodate a larger cavity and therefore a larger signal. Furthermore, the temperature of the superfluid helium cryostat can reach 2K. In this temperature range, we will use a low-noise, high-temperature superconducting amplifier that we are currently developing. All these improvements will enhance our sensitivity.

References

- [1] R. J. Crewther. Effects of Topological Charge in Gauge Theories. *Acta Phys. Austriaca Suppl.*, 19:47–153, 1978.
- [2] Steven Weinberg. The $u(1)$ problem. *Phys. Rev. D*, 11:3583–3593, Jun 1975.
- [3] S. Navas et al. Review of particle physics. *Phys. Rev. D*, 110(3):030001, 2024.
- [4] Stephen L. Adler. Axial-vector vertex in spinor electrodynamics. *Phys. Rev.*, 177:2426–2438, Jan 1969.
- [5] William A. Bardeen. Anomalous currents in gauge field theories. *Nuclear Physics B*, 75(2):246–258, 1974.
- [6] G. 't Hooft. Symmetry breaking through bell-jackiw anomalies. *Phys. Rev. Lett.*, 37:8–11, Jul 1976.
- [7] Gerard t Hooft and Falk Bruckmann. Monopoles, instantons and confinement. 11 2000.
- [8] R. Jackiw and C. Rebbi. Vacuum periodicity in a yang-mills quantum theory. *Phys. Rev. Lett.*, 37:172–175, Jul 1976.
- [9] R. D. Peccei and Helen R. Quinn. CP conservation in the presence of pseudoparticles. *Phys. Rev. Lett.*, 38:1440–1443, Jun 1977.
- [10] Steven Weinberg. A new light boson? *Phys. Rev. Lett.*, 40:223–226, Jan 1978.
- [11] Roberto D. Peccei. *The Strong CP Problem and Axions*, page 3–17. Springer Berlin Heidelberg, 2008.
- [12] Pierre Sikivie. Invisible axion search methods. *Reviews of Modern Physics*, 93(1), February 2021.
- [13] Jihn E. Kim. Weak-interaction singlet and strong CP invariance. *Phys. Rev. Lett.*, 43:103–107, Jul 1979.
- [14] M.A. Shifman, A.I. Vainshtein, and V.I. Zakharov. Can confinement ensure natural cp invariance of strong interactions? *Nuclear Physics B*, 166(3):493–506, 1980.
- [15] Michael Dine, Willy Fischler, and Mark Srednicki. A simple solution to the strong cp problem with a harmless axion. *Physics Letters B*, 104(3):199–202, 1981.
- [16] Gianfranco Bertone and Dan Hooper. History of dark matter. *Rev. Mod. Phys.*, 90:045002, Oct 2018.
- [17] Heinz Andernach and Fritz Zwicky. English and spanish translation of zwicky’s (1933) the redshift of extragalactic nebulae, 2017.
- [18] Erik Holmberg. On the Clustering Tendencies among the Nebulae. , 92:200, September 1940.
- [19] J. Neyman, T. Page, and E. Scott. CONFERENCE on the Instability of Systems of Galaxies (Santa Barbara, California, August 10-12, 1961): Summary of the conference. , 66:633, December 1961.
- [20] I. S. Chandrasekhar. The Time of Relaxation of Stellar Systems. , 93:285, March 1941.
- [21] Morton S. Roberts. A High-Resolution 21-CM Hydrogen-Line Survey of the Andromeda Nebula. , 144:639, May 1966.
- [22] R. P. Olling and M. R. Merrifield. Two measures of the shape of the dark halo of the milky way. *Monthly Notices of the Royal Astronomical Society*, 311(2):361–369, January 2000.
- [23] Michael S. Turner. Cosmic and local mass density of “invisible” axions. *Phys. Rev. D*, 33:889–896, Feb 1986.

- [24] Vera C. Rubin and W. Kent Ford, Jr. Rotation of the Andromeda Nebula from a Spectroscopic Survey of Emission Regions. , 159:379, February 1970.
- [25] Tisserand, P. et al. Limits on the macho content of the galactic halo from the eros-2 survey of the magellanic clouds ***. *AA*, 469(2):387–404, 2007.
- [26] G. Gamow. Expanding universe and the origin of elements. *Phys. Rev.*, 70:572–573, Oct 1946.
- [27] A. A. Penzias and R. W. Wilson. A Measurement of Excess Antenna Temperature at 4080 Mc/s. , 142:419–421, July 1965.
- [28] P. A. R. Ade et al. Planck2015 results: Xiii. cosmological parameters. *Astronomy amp; Astrophysics*, 594:A13, September 2016.
- [29] D. N. Page and S. W. Hawking. Gamma rays from primordial black holes. , 206:1–7, May 1976.
- [30] Hee Il Kim, Chul H. Lee, and Jane H. MacGibbon. Diffuse γ -ray background and primordial black hole constraints on the spectral index of density fluctuations. *Phys. Rev. D*, 59:063004, Feb 1999.
- [31] M. Milgrom. A modification of the Newtonian dynamics as a possible alternative to the hidden mass hypothesis. , 270:365–370, July 1983.
- [32] Jacob D. Bekenstein. Relativistic gravitation theory for the modified newtonian dynamics paradigm. *Phys. Rev. D*, 70:083509, Oct 2004.
- [33] S. D. M. White, C. S. Frenk, and M. Davis. Clustering in a neutrino-dominated universe. , 274:L1–L5, November 1983.
- [34] Scott Dodelson and Lawrence M. Widrow. Sterile neutrinos as dark matter. *Phys. Rev. Lett.*, 72:17–20, Jan 1994.
- [35] Savas Dimopoulos and Howard Georgi. Softly broken supersymmetry and su(5). *Nuclear Physics B*, 193(1):150–162, 1981.
- [36] Heinz Pagels and Joel R. Primack. Supersymmetry, cosmology, and new physics at teraelectronvolt energies. *Phys. Rev. Lett.*, 48:223–226, Jan 1982.
- [37] Gary Steigman and Michael S. Turner. Cosmological constraints on the properties of weakly interacting massive particles. *Nuclear Physics B*, 253:375–386, 1985.
- [38] Ciaran O’HARE. cajohare/axionlimits: Axionlimits, July 2020.
- [39] E.V. Karukes, M. Benito, F. Iocco, R. Trotta, and A. Geringer-Sameth. Bayesian reconstruction of the milky way dark matter distribution. *Journal of Cosmology and Astroparticle Physics*, 2019(09):046–046, September 2019.
- [40] Pablo F de Salas and A Widmark. Dark matter local density determination: recent observations and future prospects. *Reports on Progress in Physics*, 84(10):104901, October 2021.
- [41] L. D. Duffy and P. Sikivie. Caustic ring model of the milky way halo. *Phys. Rev. D*, 78:063508, Sep 2008.
- [42] Francesca Chadha-Day, John Ellis, and David J. E. Marsh. Axion dark matter: What is it and why now?, 2022.
- [43] N. Aghanim et al. Planck2018 results: Vi. cosmological parameters. *Astronomy amp; Astrophysics*, 641:A6, September 2020.
- [44] Guillermo Ballesteros, Javier Redondo, Andreas Ringwald, and Carlos Tamarit. Standard model—axion—seesaw—higgs portal inflation. five problems of particle physics and cosmology solved in one stroke. *Journal of Cosmology and Astroparticle Physics*, 2017(08):001–001, August 2017.

- [45] D. H. Lyth. Axions and inflation: Vacuum fluctuations. *Phys. Rev. D*, 45:3394–3404, May 1992.
- [46] So-Young Pi. Inflation without tears: A realistic cosmological model. *Phys. Rev. Lett.*, 52:1725–1728, May 1984.
- [47] David J.E. Marsh. Axion cosmology. *Physics Reports*, 643:1–79, July 2016.
- [48] Malte Buschmann, Joshua W. Foster, and Benjamin R. Safdi. Early-universe simulations of the cosmological axion. *Physical Review Letters*, 124(16), April 2020.
- [49] Evan Berkowitz, Michael I. Buchoff, and Enrico Rinaldi. Lattice qcd input for axion cosmology. *Physical Review D*, 92(3), August 2015.
- [50] Leesa Fleury and Guy D. Moore. Axion dark matter: strings and their cores. *Journal of Cosmology and Astroparticle Physics*, 2016(01):004–004, January 2016.
- [51] Luca Di Luzio, Belen Gavela, Pablo Quilez, and Andreas Ringwald. Dark matter from an even lighter qcd axion: trapped misalignment. *Journal of Cosmology and Astroparticle Physics*, 2021(10):001, October 2021.
- [52] Fuminobu Takahashi. Trapped misalignment mechanism and its cosmological implications. Axion Workshop, <https://sites.google.com/view/axionworkshop>, 2023. Accessed: 2025-01-19.
- [53] Tetsutaro Higaki, Kwang Sik Jeong, Naoya Kitajima, and Fuminobu Takahashi. Quality of the peccei-quinn symmetry in the aligned qcd axion and cosmological implications. *Journal of High Energy Physics*, 2016(6), June 2016.
- [54] Chiara P. Salemi, Joshua W. Foster, Jonathan L. Ouellet, Andrew Gavin, Kaliroë M.W. Pappas, Sabrina Cheng, Kate A. Richardson, Reyco Henning, Yonatan Kahn, Rachel Nguyen, Nicholas L. Rodd, Benjamin R. Safdi, and Lindley Winslow. Search for low-mass axion dark matter with abracadabra-10 cm. *Physical Review Letters*, 127(8), August 2021.
- [55] N. Crisosto, P. Sikivie, N.S. Sullivan, D.B. Tanner, J. Yang, and G. Rybka. Admx slic: Results from a superconducting lc circuit investigating cold axions. *Physical Review Letters*, 124(24), June 2020.
- [56] Alexander V. Gramolin, Deniz Aybas, Dorian Johnson, Janos Adam, and Alexander O. Sushkov. Search for axion-like dark matter with ferromagnets. *Nature Physics*, 17(1):79–84, August 2020.
- [57] L. Brouwer et al. Projected sensitivity of dmradio-m3: A search for the qcd axion below 1ev. *Physical Review D*, 106(10), November 2022.
- [58] HAYSTAC Collaboration et al. Dark matter axion search with haystac phase ii, 2024.
- [59] C. Bartram et al. Axion dark matter experiment around 3.3 μeV with *dine – fischler – srednicki – zhitnitsky* discoveryability, 2024.
- [60] Matthew Lawson, Alexander J. Millar, Matteo Pancaldi, Edoardo Vitagliano, and Frank Wilczek. Tunable axion plasma haloscopes. *Physical Review Letters*, 123(14), October 2019.
- [61] Jesse Liu, Kristin Dona, et al. Broadband solenoidal haloscope for terahertz axion detection. *Physical Review Letters*, 128(13), March 2022.
- [62] B. Ary dos Santos Garcia, D. Bergermann, et al. First search for axion dark matter with a madmax prototype, 2024.
- [63] Deniz Aybas, Janos Adam, et al. Search for axionlike dark matter using solid-state nuclear magnetic resonance. *Physical Review Letters*, 126(14), April 2021.
- [64] C. Abel, N.J. Ayres, et al. Search for axionlike dark matter through nuclear spin precession in electric and magnetic fields. *Physical Review X*, 7(4), November 2017.
- [65] K. van Bibber, P. M. McIntyre, D. E. Morris, and G. G. Raffelt. Design for a practical laboratory detector for solar axions. *Phys. Rev. D*, 39:2089–2099, Apr 1989.

- [66] K. Altenmüller, V. Anastassopoulos, S. Arguedas-Cuendis, et al. New upper limit on the axion-photon coupling with an extended cast run with a xe-based micromegas detector. *Phys. Rev. Lett.*, 133:221005, Nov 2024.
- [67] K. Van Bibber, N. R. Dagdeviren, S. E. Koonin, A. K. Kerman, and H. N. Nelson. Proposed experiment to produce and detect light pseudoscalars. *Phys. Rev. Lett.*, 59:759–762, Aug 1987.
- [68] K.J. Coakley, J.D. Splett, M.D. Janezic, and R.F. Kaiser. Estimation of q-factors and resonant frequencies. *IEEE Transactions on Microwave Theory and Techniques*, 51(3):862–868, 2003.
- [69] David M. Pozar. *Microwave Engineering*. Wiley, 4th edition, 2011.
- [70] Glen Cowan, Kyle Cranmer, Eilam Gross, and Ofer Vitells. Asymptotic formulae for likelihood-based tests of new physics. *The European Physical Journal C*, 71(2), February 2011.
- [71] Eilam Gross and Ofer Vitells. Trial factors for the look elsewhere effect in high energy physics. *The European Physical Journal C*, 70(1–2):525–530, October 2010.
- [72] David Tong. Particle physics, Lecture Notes.

Appendix

A CPT symmetries

We have three discrete internal symmetries: Charge (C), Parity (P), and Time (T).

The parity transformation corresponds to the sign reversal of all spatial coordinates, as if we were looking into a mirror. In a mirror, left-handed becomes right-handed. For a particle, being right-handed means that its spin is aligned with its momentum, contrary to the left-handed particle. It is what we call the chirality of a particle. This categorization only makes sense for massless particles, as they travel at the speed of light and the observer’s position is therefore of no consequence. Saying that parity symmetry is respected/conserved means that there are no differences between right-handed and left-handed particles. Unlike the strong force, the weak force and hypercharge do not respect the symmetry of parity Figure 49. We can say that the weak force performs a maximum violation of parity as it interacts only with left handed particles.

Particles		Strong	Weak	Hypercharge
Left-handed	quarks	yes	yes	+1/6
	leptons	no	yes	-1/2
Right-handed	up quark	yes	no	+2/3
	down quark	yes	no	-1/3
	electron	no	no	-1
	neutrino	no	no	0

Figure 48: Particle categorization arises from discrete differences in their interactions with forces. From [72].

Charge conjugation is the transformation of a particle into its antiparticle. The antiparticle has the same mass as the particle but with opposite signs for all physical charges (electric charge, QCD color charge, etc.). Charge symmetry is respected if the antiparticle undergoes the same physics as the corresponding particle. Among anti-particles, the weak force interacts only with right handed anti-particles.

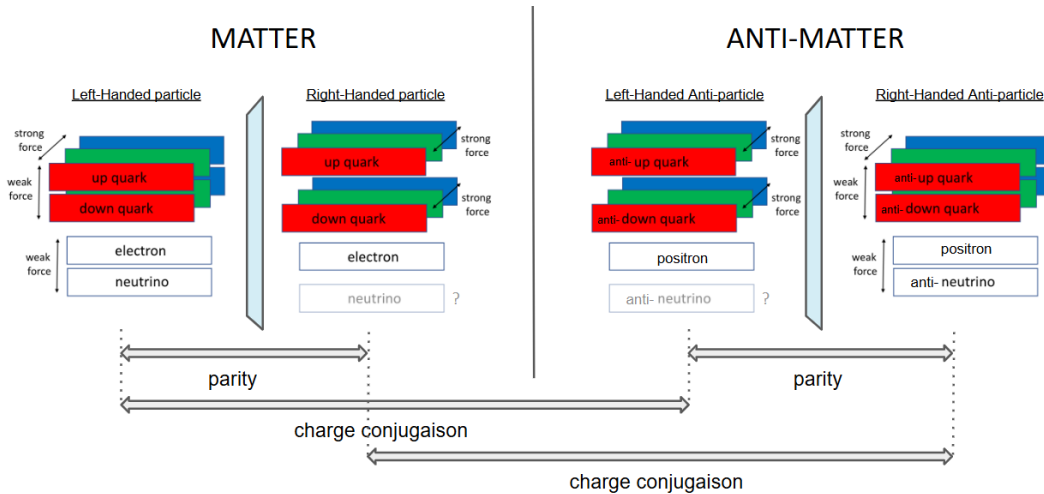


Figure 49: And similar schematic for the 2nd and 3rd generation, so in total $16 \times 2 \times 3 = 96$ fermions (if we suppose the neutrino is not a Majorana particle). This figure remains incomplete as it suggests CP symmetry to be true. Adapted from [72]

CP symmetry means that the laws of physics are invariant under the simultaneous use of charge

symmetry and parity symmetry. In other words, we would observe the same physics if we were to swap particles with their antiparticles and then take their reflection in the mirror.

B Basic definitions in Gauge theories

We note A_μ a Yang-Mills field with Greek letters for the Lorentz indexes. To the Lie group (or more precisely a gauge group, e.g $SU(2)$ or $SU(3)$), we can define the corresponding Lie Algebra with a set of basis generators $\{\tau^a\}$ and the following commutation relations:

$$[\tau^a, \tau^b] = if^{abc}\tau^c \quad \text{with } f^{abc} \text{ the structure coefficients and Einstein summation notation.}$$

Since the gauge field is an element of the Lie Algebra, it can be decomposed as,

$$A_\mu(x) = A_\mu^a(x)\tau^a$$

The exponential maps between Lie Groups and Lie Algebras ensure that for all element Ω of the gauge group, it exists a function ξ so that,

$$\Omega = e^{i\xi^a(x)\tau^a}$$

Under a gauge transformation, the gauge field transforms as,

$$A_\mu \rightarrow \Omega A_\mu \Omega^{-1} + \frac{i}{g} \Omega \partial_\mu \Omega^{-1} \quad \text{with } g \text{ the coupling constant}$$

The field-strength tensor $F_{\alpha\beta}$ and its dual $\tilde{F}^{\alpha\beta}$ are defined by,

$$\begin{aligned} F_{\alpha\beta} &= \partial_\alpha A_\beta - \partial_\beta A_\alpha - ig[A_\alpha, A_\beta] \\ F_{\alpha\beta}^a &= \partial_\alpha A_\beta^a - \partial_\beta A_\alpha^a + gf^{abc} A_\alpha^b A_\beta^c \\ \tilde{F}^{\alpha\beta} &= \frac{1}{2} \varepsilon^{\alpha\beta\mu\lambda} F_{\mu\lambda} \quad \text{with } \varepsilon^{\alpha\beta\mu\lambda} \text{ the antisymmetric tensor} \end{aligned}$$

With Einstein summation notation $F_{\mu\nu}^a \tilde{F}^{a\mu\nu} = F \cdot \tilde{F}$
Note that in some references, the dual is noted F^* .

C Goodness of fit

All out fitting process are based on the chi-square minimization method.

A fitting function is a theoretical model that wants to be tested on our data. Some parameters of the function are let free. To quantify the accordance between the model and the data one can think of calculating the sum of quantitative deviations.

$$D(\{\text{parameters}\}, \{\text{data points}\}) = \sum_N \frac{(x_i - m(f_i))^2}{m(f_i)}$$

with x_i the experimental data and, $m(f_i)$ the value returned by the fitting function m , both for the frequency f_i . N the number of discrete frequencies in the fitting range. The function D takes as inputs, the parameters of the fitting function and the data points, and return a quantitative value that characterizes the goodness of the fit. For example, in the context of the Lorentz fit,

$$\begin{aligned} \{\text{parameters}\} &= \{A, \Gamma, f_r, p_0, \dots\} \\ \{\text{data points}\} &= \{x_0, x_1, \dots, x_N\} \end{aligned}$$

As some parameters of the fitting function are free, we create an algorithm that tests different parameter values until the D deviation is minimized. This minimization is what we will refer to as the fitting process. The parameters resulting from the fitting process and the values returned by the final model are called “estimates” and written with a hat.

$$D(A, \Gamma, f_r, p_0, \dots) \longrightarrow D(\hat{A}, \hat{\Gamma}, \hat{f}_r, \hat{p}_0, \dots) = D_{min} = \sum_N \frac{(x_i - \hat{x}_i)^2}{\hat{x}_i}$$

However, when calculating the limit, the algorithm cannot be infinitely precise. This is why we need to set a threshold called ”tolerance”, below which the difference dD is considered small enough for the fitting process to stop iterating. Besides, a maximum number of iterations or ”calls” is set in case the D does not converge at all.

$$\text{if } D_k - D_{k+1} \leq T \Rightarrow D_k = D_{min}$$

with T the tolerance

and the iteration index $k <$ maximum number of calls

The tolerance is set to 0.01 by default in ROOT.

In our case, the expected value is much bigger than the observed deviation, which gives us very small D . Unfortunately, the calculation of a difference does not work well with very small values because ”double” object in c++ has a limited memory. Therefore, we replace \hat{x}_i at the denominator, by a value we note σ_i^2 .

$$D(\{\text{parameters}\}, \{\text{data points}\}) = \sum_{i=1}^N \frac{(x_i - \hat{x}_i)^2}{\sigma_i^2}$$

This notation is more general. We can choose $\sigma_i^2 = 1 * \hat{x}_i$ and have the original D , but we can also decide to take $\sigma_i^2 = 0.1 * \hat{x}_i$ to have bigger D value. If \hat{x}_i is very big compared to the variation $(x_i - \hat{x}_i)^2$ we can suppose a non-dependence of the denominator on the expected value with, for instance $\sigma_i^2 = 0.1$. For the moment, we do not make any assumption and we keep the general notation σ_i^2 .

You may wonder why this value is called σ_i^2 . The reason lies in the way we can interpret this value. We note

$$Z_i = \frac{x_i - \hat{x}_i}{\sigma_i}$$

We recognize the standardized variable of the random variable $x_i \hookrightarrow \mathcal{N}(\hat{x}_i, \sigma_i)$. Hence D can be interpreted as the sum of Z_i squared, with $Z_i \hookrightarrow \mathcal{N}(0, 1)$. If we suppose the Z_i to be independent than, by definition, D follows a χ^2 distribution. Actually, we do not have N independent Z_i because the free parameters of our fitting function gives some relation between the Z_i . The number of independent variables that we can have is more exactly equal to the number of degrees of freedom NdF .

$$NdF = N - \text{number of free parameters}$$

By definition, the sum of the squares of NdF independent standard normal random variables follows a χ^2 distribution. Since the number of frequencies N is much larger than the number of free parameters (~ 5) we can approximate,

$$\chi^2 = \sum_{i=1}^{NdF} \left(\frac{x_i - \hat{x}_i}{\sigma_i} \right)^2 \approx \sum_{i=1}^N \left(\frac{x_i - \hat{x}_i}{\sigma_i} \right)^2$$

Here χ^2 is the name of the variable and the name of the distribution it follows. Approaching our quantitative deviation D with a variable that follows a known distribution will be very useful for setting confidence intervals (section...). But for now, we can just remember that the value returned by D , that characterizes the goodness of our fit, follows approximately a well-known distribution called χ^2 and mathematically, this holds for any σ_i . That is why, our fitting process is said to be based on the

chi-square minimization method.

In practice, on ROOT, we implement the value of σ_i by adding error bars to the x_i data. ROOT will automatically standardize the variables according to these error bars before calculating the chi-square. In other words, we apply our fitting to a TGraphError which include our experimental data and the error $\pm\sigma_i$. The σ_i notation was introduced to possibly overcome the limitations of the fitting process, but ends up being the error bar on our data. How to interpret this?

As said at the beginning of this section, D tests the match between a model and the data. The value in the denominator is used to weight each squared difference. Weighting with $\sigma_i^2 = m(f_i)$ is considering the relative squared deviation compared to the model. On the other hand, taking the same σ_i for all frequencies means giving the same importance to all deviations. Therefore, with a high σ_i , we allow the final fit to deviate from the concerned data point, while with a low σ_i , we give priority to the fit that comes closest to the data point. As a result, σ_i acts as an allowed error around this data point. Now, to know what error bars to use we try, see, and go backward if necessary. For example, we can suppose, at first, that all the σ_i are the same and of order 10^{-17} . We try the fitting process. Once we get the last fitting function, we subtract it to the data. The result of this subtraction is called "residuals". In the residuals we can see the deviation between data points and fitting function and so verify if we have or not the same fluctuations for all points. It is possible that we cannot conclude from the residuals of the Lorentz fit because of some remaining structure. This structure is due to the incompleteness of our background model. So it is after background fit that we can admit the residuals to be due to random noise and therefore reconsider our choice of sigmas. Then, we have to do the fitting process all over again with the exact error bars to be sure to get the right parameter estimates and final χ^2 .

D Lorentz approximation

Let's note,

$$\alpha = \frac{f - f_r}{f_r}$$

Near resonance α tends to zero, so we can use series expansion in alpha.

$$\frac{f}{f_r} - \frac{f_r}{f} = \alpha + 1 - \frac{1}{\alpha + 1} = \frac{\alpha^2 + 2\alpha}{\alpha + 1} \underset{0}{=} (\alpha^2 + 2\alpha)(1 + \mathcal{O}(\alpha)) = 2\alpha + \mathcal{O}(\alpha^2)$$

$$\begin{aligned} |S_{21}(f)|^2 &= \frac{|S_{21}(f_r)|^2}{1 + Q^2(2\alpha + \mathcal{O}(\alpha^2))^2} \\ &= \frac{|S_{21}(f_r)|^2}{1 + Q^2(4\alpha^2 + \mathcal{O}(4\alpha^3))} \\ &= \frac{|S_{21}(f_r)|^2}{1 + 4Q^2\alpha^2} \times \frac{1 + 4Q^2\alpha^2}{1 + 4Q^2\alpha^2 + \mathcal{O}(4Q^2\alpha^3)} \\ &= \frac{|S_{21}(f_r)|^2}{1 + 4Q^2\alpha^2} \times (1 + 4Q^2\alpha^2)(1 - 4Q^2\alpha^2 + \mathcal{O}(4Q^2\alpha^3)) \\ &= \frac{|S_{21}(f_r)|^2}{1 + 4Q^2\alpha^2} \times (1 + \mathcal{O}(4Q^2\alpha^3)) \\ &= \frac{A}{\Gamma^2 + (f - f_r)^2} + \frac{|S_{21}(f_r)|^2}{1 + 4Q^2\alpha^2} \mathcal{O}(4Q^2\alpha^3) \\ &= \frac{A}{\Gamma^2 + (f - f_r)^2} + |S_{21}(f_r)|^2 (1 - 4Q^2\alpha^2 + \mathcal{O}(4Q^2\alpha^3)) \mathcal{O}(4Q^2\alpha^3) \\ &= \frac{A}{\Gamma^2 + (f - f_r)^2} + \mathcal{O}(4|S_{21}(f_r)|^2 Q^2 \alpha^3) \end{aligned}$$

E Details of lorentz fit results on VNA data

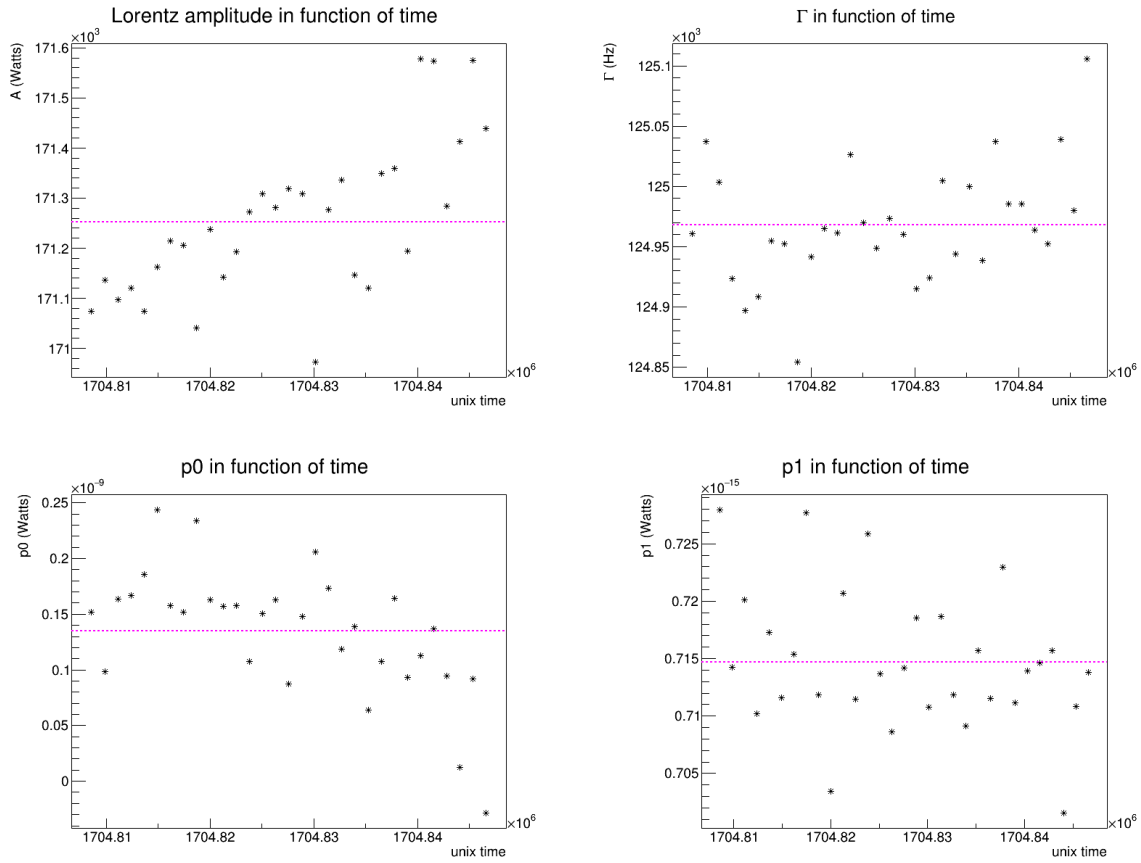


Figure 50: Other fitting parameters as a function of time. The mean value is indicated by a magenta marker.

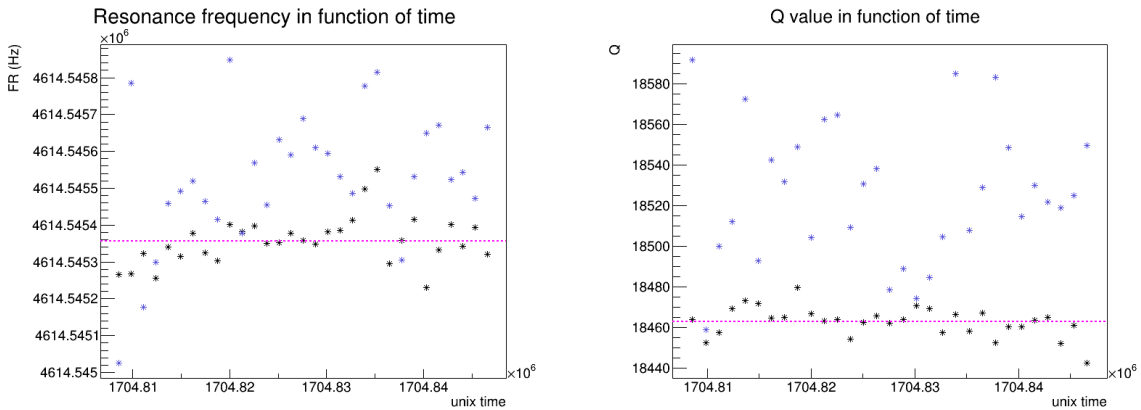


Figure 51: Resonance frequency and Q value fluctuation during compilation interval. Blue dots are the fitting initial value and black dots are the results for the biggest fitting range. $Q = 18463 \pm 0.12\%$

F Natural units

$$\hbar = 6.582 \times 10^{-16} \text{ eV}\cdot\text{s} \equiv 1 \quad \text{implies} \quad 1 \text{ Hz} = 1 \text{ s}^{-1} = 6.582 \times 10^{-16} \text{ eV},$$

so,

$$m_a = 2\pi\nu_0 \text{ Hz} = \nu_0 \cdot 4.1356 \times 10^{-15} \text{ eV},$$

$$1 \text{ W} = 1 \text{ J}\cdot\text{s}^{-1} = \frac{1}{1.602 \times 10^{-19}} \text{ eV}\cdot\text{s}^{-1} = \frac{6.582 \times 10^{-16}}{1.602 \times 10^{-19}} \text{ eV}^2 = 4.108 \times 10^3 \text{ eV}^2,$$

$$1 \text{ T} = 10^4 \text{ G} = 1.9535 \times 10^2 \text{ eV}^2 \quad (\text{cf. eq. (48) of [12]}).$$